

3697



Stability and Transition in Boundary Layers: Effect of Transverse Curvature and Pressure Gradient

A Thesis
Submitted for the Degree of
DOCTOR OF PHILOSOPHY

by
N. VINOD



ENGINEERING MECHANICS UNIT
JAWAHARLAL NEHRU CENTRE FOR ADVANCED SCIENTIFIC
RESEARCH

(A Deemed University)

Bangalore – 560 064

SEPTEMBER 2005

To my parents

DECLARATION

I hereby declare that the matter embodied in the thesis entitled “**Stability and transition in boundary layers: Effect of transverse curvature and pressure gradient**” is the result of investigations carried out by me at the Engineering Mechanics Unit, Jawaharlal Nehru Centre for Advanced Scientific Research, Bangalore, India under the supervision of Prof. Rama Govindarajan and that it has not been submitted elsewhere for the award of any degree or diploma.

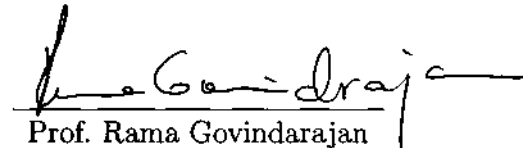
In keeping with the general practice in reporting scientific observations, due acknowledgment has been made whenever the work described is based on the findings of other investigators.



N. Vinod

CERTIFICATE

I hereby certify that the matter embodied in this thesis entitled "**Stability and transition in boundary layers: Effect of transverse curvature and pressure gradient**" has been carried out by Mr. N. Vinod at the Engineering Mechanics Unit, Jawaharlal Nehru Centre for Advanced Scientific Research, Bangalore, India under my supervision and that it has not been submitted elsewhere for the award of any degree or diploma.


Prof. Rama Govindarajan
(Research Supervisor)

Acknowledgments

This thesis is the result of a gratifying period of work through which I have been accompanied and supported by many people. I take this opportunity to express my sincere gratitude to all of them. The first and foremost person I would like to thank is my research supervisor Prof. Rama Govindarajan for suggesting this work and encouraging me to pursue many exciting problems in the field. It was a great pleasure to work under her supervision. I am further indebted to her for her guidance with boundless enthusiasm, patience and optimism. Her inputs and directions were invaluable in the creation of this thesis, and the research that it contains. Her wide knowledge in various branches of fluid dynamics and mathematics was always of great help.

I would like to thank Prof. Roddam Narasimha for the numerous inspiring discussions and suggestions, which have helped me gain insight into my research. His integral and unique viewpoints on research, critical comments, and questions are to be appreciated.

I would like to thank Dr. K. R. Sreenivas for his help and advice during my research work. His valuable suggestions have helped me a lot during the course of my Ph.D program. I extend my thanks to Dr. Meheboob Alam also for his suggestions towards this thesis.

My special thanks to Sameen, whom I have known for more than ten years now, and who has always been a helpful and trusted friend. The countless discussions and arguments I have had with him have helped me to streamline my research. I would like to thank Hamsa Balakrishnan, who has contributed significantly to the initial part of theory formulation of stability and to preliminary code development. I am grateful to Rajesh for his help in learning spectral collocation method. I would like to thank Kirti Sahu for giving me the flavour of various CFD techniques and helping me in solving the meanflow code using finite difference methods. I wish to thank Vijay for his help with the simulations.

I would like to thank, Dileep, Sameen and Pinaki for their immense help with L^AT_EX and Xfig, in writing the thesis.

The excellent working atmosphere was also indispensable for finishing this thesis. In the lab, I was surrounded by friendly and loving people who helped me everyday. I would like to thank all of them: Shiva, Saji, Raji, Sameen, Kirti, Vijay, Mukund, Faraz, Mani, Anjana, Kaushik, Pinaki, Shreyas, Punit, Sanjeev, Antina and Binaya, for their constant support. Special thanks to Faraz and Mani who gave me the feeling of being at home during my

work.

I would like to thank the computer lab of JNCASR for providing excellent computation facilities. Special thanks are due to Rajesh Kanna, Shithal, Nagamani, Sudhee, James, Ravi, Dr. Bala and Dr. Umesh for the efficient maintenance of the computing system. They deserve much more appreciation than just being mentioned here.

I am ever grateful to my institute, JNCASR for providing the necessary infrastructure and financial support.

The road to my graduate degree has been a long and winding one. During the course of my Ph. D programme i could interact with many nice people. I would like to thank those close to me, whose presence has helped me a lot towards the completion of my work. I am indebted to Manoj, who has always stood by me, Shobana, who has always wanted to see this thesis through to completion, and CP, the most reliable and ideal friend one could have. My heartfelt thanks to Kalyani, Neena and Reji for their companionship, entertainment and support. I wish to extend my earnest gratitude to S. Lakshmi, who has always encouraged me with her incisive mind, and Gautam, for providing a fun-filled environment to learn and grow. I am very much thankful to Dhanashree, for being a good friend during my stay in JNC. I am a lot lucky to have made close bonds with such empathetic and supportive people.

Special mention is to be made of the many good friends in JNC, for their immense support, motivation and care. In this regard I would like to thank Deepak, Gomathi, Ashish, John, Jaya, Pattu, Sujay, Selvi, Vivek, Sudhee, Ram, Sreeraj, Patric, Rupesh and Kinson. The chain of my gratitude would be definitely incomplete if I forget to mention my friends: Ashwin, Krishnan, Kavitha, Pushpa, Sharmila, Shailesh, Sarathy, Priya, Ved, Arpita, Ksiva, Rajesh, Prashant, Vaidhya, Viji, Selvi and Sajini. My stay in the campus would not have been so fun-filled and happy, but for all of them.

A simple thanks is not enough to my parents who continue to give their best, for the welfare and prosperity of their children. Their constant care and guidance has indeed helped me to grow into the person I am today. I would like to thank my brothers and sisters-in-law for their unwavering encouragement and support. My family has always been a constant source of inspiration for me, imparting the sense and the value of brotherhood.

Preface

This thesis is aimed at understanding the effects of transverse curvature on instability and transition in laminar boundary layers. A connection between the behaviour at the onset of transition and the patterns in upstream instability is also made.

The first part of this thesis involves the formulation of a stability theory for the laminar boundary layer around an axisymmetric body steadily translating through fluid in a direction parallel to its axis and the development of a spectral code to solve the ensuing stability equations. We make the parallel flow assumption for the axisymmetric boundary layer, since present wisdom is that non-parallel effects are not too large in two-dimensional mean flows. A range of surface curvatures, from almost two-dimensional surfaces and extending to very thin bodies are considered for the stability analysis. For thick cylinders we use a Blasius type profile as mean flow. For thinner cylinders the mean velocity profile is computed by solving Navier-Stokes equations, under the boundary layer approximation.

The main findings on instability are as follows. In an extension of Rayleigh's and Fjørtoft's theorem to axisymmetric boundary layers, the boundary layer past a cylinder is shown to be inviscidly stable to linear disturbances. Above a certain level of curvature, the flow is found to be linearly stable at all Reynolds numbers. Squire's theorem does not apply and the helical mode is unstable at the lowest Reynolds number.

At low curvatures, several nonaxisymmetric modes are simultaneously unstable, and the production layers of the disturbance kinetic energy have a significant overlap. Higher non-axisymmetric modes ($n \geq 2$) are linearly unstable only for a very small range of curvatures. The helical ($n = 1$) mode is unstable over a significant axial extent of the cylinder, but is never unstable for curvatures above 1. Here the curvature is defined as the ratio of momentum thickness (θ) to the body radius (r_0). Curvature has an overall stabilising effect, both via the mean flow, as well as directly through the stability equations.

The secondary instability analysis of the flow containing linear modes of a certain amplitude is carried out. It is found that secondary modes remain unstable at larger curvatures than linear modes. However there is again a maximum curvature, given by $\theta \approx 2r_0$, above which all disturbances decay. It is found that the most unstable secondary modes are always those whose azimuthal wavenumbers are related to that of the linear mode by $m_+ = 2n$ and $m_- = -n$. As in two-dimensional boundary layers the subharmonic (in terms of axial wavenumber) modes are least stable.

For the transition zone we have focussed mainly on two-dimensional boundary layers. This is because the connection between instability and the onset of transition is not completely understood even for this case. Secondly experimental results are available only for this case. Stochastic simulations, inspired by a cellular-automaton approach, of turbulent spot generation and propagation in transitional boundary layers have been conducted, employing the hypothesis of concentrated breakdown and the observation that spot growth is self-similar. In conjunction with experimental measurements, the approach can serve as a useful new tool to study transition zone behaviour.

The objective is to make a connection between secondary instability and the onset of transition. It is shown that experimental measurements of intermittency in high disturbance environments as well as in adverse pressure gradients are consistent with a mostly regular pattern in the birth of turbulent spots, rather than randomly distributed spot birth as hitherto assumed. The pattern is as dictated by the secondary instability. At zero pressure gradient, when the disturbance is low, the intermittency is consistent with random spot birth; reasons are discussed. The simulations are used to validate the hypothesis of concentrated breakdown as well as to investigate the effect of the calmed region behind a turbulent spot. Further predictions are made which may be experimentally verified.

Just after its onset, transition on an axisymmetric body proceeds exactly as it would in two-dimensional flow. Downstream, especially when the lateral merger of turbulent spots is frequent, a patch of turbulence wraps itself around the body. There is no further lateral growth and transition proceeds much more slowly after this.

Publications

N. Vinod and R. Govindarajan, "Pattern of breakdown of laminar flow into turbulent spots" *Physical Review Letters*, 93, 114501, 2004

N. Vinod and R. Govindarajan "Instabilities and Transition in Boundary Layers", *Pramana- Journal of Physics*, 64, 3, 1-10, 2005

N. Vinod and R. Govindarajan "Signature of laminar instability in a decelerating boundary layer", communicated. (<http://arXiv.org/abs/physics/0504222>)

N. Vinod and R. Govindarajan "Linear and secondary instabilities on Axisymmetric Boundary Layers : Effects of Transverse curvature", preprint, 2005

N. Vinod and R. Govindarajan, "Instabilities in an axisymmetric boundary layer" *Accepted to International Conference on Marine Hydrodynamics* Visakhapattanam, INDIA, 2006

R. Govindarajan, **N. Vinod** and A. Sameen, "The many routes to turbulence in shear flows" *Proc. Seventh Natl. CFD Conf.* Bangalore, INDIA, 2005

N. Vinod and R. Govindarajan, "Aspects of the Laminar-Turbulent Transition in Axisymmetric Boundary Layers" *Proc. 21st, International Congress of Theoretical and Applied Mechanics*, Warsaw, POLAND, 2004.

N. Vinod and R. Govindarajan, "Are subtransitions in boundary layers a signature of laminar instability?" *Proc. International Symposium on Advances in Fluid Mechanics*, Bangalore, INDIA, 2003.

N. Vinod, Hamsa Blakrishnan and R. Govindarajan, "Stability analysis of an axisymmetric boundary layer", *Proc. of Ninth Asian Congress on Fluid Mechanics*, Isfahan, IRAN, 2002.

N. Vinod and R. Govindarajan, "The transition zone in adverse pressure gradient boundary layers: Results from stochastic simulations " *Proc. XV Intl. Symposium on Air Breathing Engines* Bangalore, INDIA, 2001

N. Vinod and R. Govindarajan, "Axisymmetric instabilities in the boundary layer over a cylinder" *Proc. Third Natl. CFD Conf.* Bangalore INDIA, 2001

Nomenclature

Roman Letters

A_p	:	Amplitude of primary waves
B	:	Burst Rate in transition zone
c	:	Phase speed of disturbant waves
F	:	Intermittency growth parameter
f	:	Falkner-Skan function
G	:	Area factor of turbulent spots
g	:	Glauert-Lighthill function
k_+, k_-	:	Streamwise wave numbers of secondary instability waves
m	:	Pressure gradient parameter
m_+, m_-	:	Number of secondary waves encircling the body
n	:	Number of primary waves encircling the body
S	:	Curvature
R_θ	:	Reynolds number based on free-stream velocity and radius of cylinder
R_θ	:	Reynolds number based on free-stream velocity and momentum thickness
U	:	Mean flow velocity
U_∞	:	Free-stream velocity
W	:	Persistence time of laminar flow in transition zone

Greek Letters

α	:	Streamwise wave number of primary instability wave
β	:	Spanwise wave number of primary instability wave
δ	:	Boundary layer thickness
δ^*	:	Dispacemnet thickness

- γ : Intermittency of transition zone
 λ_θ : Falkner-Skan pressure gradient parameter
 ν : Kinematic viscosity
 ω : Frequency of primary instability wave
 ψ, ϕ : Generalised stream function of disturbant waves.
 θ : Momentum thickness

Subscripts

- r : Real part of complex quantity
 i : Imaginary part of complex quantity
 p : Primary disturbant wave
 s : Secondary disturbant wave

List of Figures

1.1	Schematic diagram of the sequence of events in laminar-turbulent transition process on a boundary layer in the flow past a semi-infinite flat plate.	5
1.2	Schematic diagram of two patterns of three-dimensionality, (a) <i>K</i> -type breakdown where the streamwise wavelength of Λ vortices is equal to that of the two-dimensional TS waves ($\lambda_x = \lambda_{TS}$). (b) <i>N</i> -type/ <i>H</i> -type breakdown: the wavelength of three-dimensional pattern is double the TS wavelength ($\lambda_x = 2\lambda_{TS}$).	10
1.3	Sketch of contours of streamwise velocity in instability modes of streaks. Solid lines represent the low-speed streaks and dashed lines are for the high-speed streaks. The fundamental modes are shown in the left, while the subharmonic modes are shown in the right (from Schmid & Henningson, 2001).	15
1.4	Schematic diagram of the growth of turbulent spots in the transition zone in a flat plate boundary layer.	18
2.1	Schematic diagram showing the coordinate system.	25
2.2	Velocity profile ($U = U_d/U_\infty \equiv f'$: solid line) and its derivatives for Blasius flow. Dashed line: the first derivative (f''); dot dashed line: second derivative (f''').	27
2.3	Comparison of streamwise velocity profiles. Solid line: numerical solution of equation 2.1 with $R = 5 \times 10^5$. Symbols: Blasius.	30
2.4	Comparison of normal velocity at different streamwise locations. The solid lines are the numerical solutions at $R = 5 \times 10^5$ and symbols are Blasius solutions.	30

2.5	Comparison of streamwise velocity with results from Tutty <i>et al.</i> (2002) at $R = 10^4$. The ordinate shows $z = \sqrt{R/x^*}(r - 1)$. The different curves are for different streamwise locations, the lowest curve is at $x = 10^5$ and the top curve is for $x = 398$. The other curves are evenly spaced at intervals of $x^{1/2}$. The symbols are results from Tutty <i>et al.</i> (2002), while the lines are present results.	31
2.6	Dimensionless boundary layer thickness $\delta\sqrt{R}/r_0$ for $R = 10^4$. The solid lines are from the numerical solution of the boundary layer equations. The symbols are results from Tutty <i>et al.</i> (2002).	31
2.7	Streamwise velocity using Navier-Stokes solution for different streamwise locations, at Reynolds number=4,000.	33
2.8	First derivative of streamwise velocity using Navier-Stokes solution for different streamwise locations, at $R = 4,000$	33
2.9	Second derivative of streamwise velocity using Navier-Stokes solution for different streamwise locations, at $R = 4,000$	34
2.10	Streamwise velocity (U) for different streamwise locations, at a Reynolds number of 400,000.	34
2.11	First derivative of streamwise velocity (U') for different streamwise locations, at a Reynolds number 400,000.	35
2.12	Second derivative of streamwise velocity (U'') for different streamwise locations, at a Reynolds number of 400,000.	35
2.13	Variation of dimensionless boundary layer thickness ($\delta\sqrt{R}/r_0$) along streamwise location, for different Reynolds number.	36
2.14	Variation of momentum thickness along streamwise coordinate, for different Reynolds numbers.	39
2.15	Variation of displacement thickness along streamwise coordinate, for different Reynolds numbers.	39
2.16	Variation of shape factor along streamwise coordinate, for different Reynolds numbers. The Blasius value (dotted line) is shown for comparison.	40
3.1	Schematic diagram showing the coordinate system	41

3.2	Inviscid stability characteristics. I_1 is shown by circles and I_2 by squares. The Reynolds number and curvature are 5000 and 0.8 respectively. The U'' of the Blasius profile is shown by the dotted line. The normal coordinate is scaled with body radius r_0	51
3.3	Comparison of present eigenspectrum with Mack (1976). $R_\theta = 385.12$ and $\alpha = 0.1189$ when scaled with θ . (In Mack's units, these were $R_{L^*} = 580$ and $\alpha_{L^*} = 0.179$).	54
3.4	Comparison of neutral stability curves at $S = 0.001$ with the Orr-Sommerfeld solution.	55
3.5	Variation of the most dominant eigenvalue with curvature. The Reynolds number and wavenumber are held constant at $R = 200$ and $\alpha = 0.14$. The flat plate eigenvalue is shown by the square. The curvature ranges from $S_0 = 0$ to $S_0 = 0.20$	55
3.6	Amplitude of disturbance velocity in the streamwise direction, for the non-axisymmetric mode $n = 1$. The Reynolds number is 300, $\alpha = 0.10$ and $S_0 = 0.05$. The solid and dashed lines are the real and imaginary parts respectively.	56
3.7	Amplitude of disturbance velocity in the radial direction, for the case shown in figure 3.6.	56
3.8	Amplitude of disturbance velocity in the azimuthal direction, for the case shown in figure 3.6.	57
3.9	Neutral stability curves ($\alpha - R$ plane) for the axisymmetric mode ($n = 0$) for different surface curvatures. The outer-most curve is for $S_0 = 0$ and the inner-most curve is for $S_0 = 0.2$. The other curves are for $S_0 = 0.02, 0.05, 0.08, 0.10, 0.12,$ and 0.15 respectively.	58
3.10	The neutral stability curves in the $\omega - R$ plane of figure 3.9.	58
3.11	Neutral stability curves in the $\alpha - R$ plane for the axisymmetric mode ($n = 1$) for different surface curvatures.	59
3.12	Neutral stability curves in the $\omega - R$ plane for the axisymmetric mode ($n = 1$) for different surface curvatures.	60
3.13	Neutral stability curves ($\alpha - R$ plane) for the non-axisymmetric mode ($n = 2$) for different surface curvatures.	60
3.14	Neutral stability curves ($\omega - R$ plane) for the non-axisymmetric mode ($n = 2$) for different surface curvatures.	61

3.15	Variation of the phase speed (c_r) with curvature for different modes ($n = 0, 1, 2, 3$). The Reynolds number and wavenumber are held constant at $R = 300$ and $\alpha = 0.10$	61
3.16	Variation of growth rate (c_i) with disturbance wavenumber for the case shown in in figure 3.15.	62
3.17	Variation of critical Reynolds number (R_{cr}) with surface curvature for different modes.	63
3.18	Comparison of second derivative (U'') of velocity for Blasius profile and Navier-Stokes solution. In the y -axis Blasius parameter η is shown.	64
3.19	Distribution of production (W_+) and dissipation (W_-) of an axisymmetric mode.	65
3.20	Distribution of production (W_+) and dissipation (W_-) of the non-axisymmetric mode $n=1$	65
3.21	Distribution of production (W_+) and dissipation (W_-) of the mode $n=2$	66
3.22	Growth rates of disturbance waves along the cylinder axis for the axisymmetric mode at $R = 15,000$	68
3.23	Decay rates of disturbance waves along the cylinder axis for the non-axisymmetric mode $n = 1$ at $R = 1000$	68
3.24	Growth rate of disturbance waves along streamwise coordinate for the non-axisymmetric mode $n = 1$ at $R = 2000$	69
3.25	Decay rate of disturbance waves along the cylinder surface for the non-axisymmetric mode $n = 2$ at $R = 5000$	70
3.26	Growth rate of disturbance waves along streamwise coordinate for the non-axisymmetric mode $n = 2$ at $R = 10000$	70
3.27	Growth rate of disturbance waves along streamwise coordinate for the non-axisymmetric mode $n = 3$ at $R = 10000$	71
3.28	Neutral stability loops for axisymmetric mode along the streamwise coordinate at different Reynolds numbers.	72
3.29	Neutral stability loops for non-axisymmetric mode $n = 1$ along the streamwise coordinate at different Reynolds numbers.	72
3.30	Neutral stability loops for non-axisymmetric mode $n = 1$ as a function of surface curvature at different Reynolds numbers.	73

3.31	Neutral stability loops for non-axisymmetric mode $n = 2$ along the streamwise coordinate at different Reynolds numbers.	74
3.32	Neutral stability loops for non-axisymmetric mode $n = 3$ along the streamwise coordinate at different Reynolds numbers.	74
3.33	Neutral stability loops for non-axisymmetric mode $n = 3$ as a function of surface curvature at different Reynolds numbers.	75
3.34	Neutral stability loops for non-axisymmetric mode $n = 4$ along the streamwise coordinate at different Reynolds numbers.	76
3.35	Neutral stability loops for non-axisymmetric mode $n = 4$ as a function surface curvature at different Reynolds numbers.	76
3.36	Production (W_+) and dissipation (W_-) rate of axisymmetric disturbance at $x = 60$, $R = 20,000$ and $\alpha = 0.125$. The location of the critical line $U = c_r$ is shown by the dashed line.	77
3.37	Production (W_+) and dissipation (W_-) rate of axisymmetric disturbance at $x = 200$, $R = 20,000$ and $\alpha = 0.125$. The location of the critical line $U = c_r$ is shown by the dashed line.	78
3.38	Production (W_+) and dissipation (W_-) rate of non-axisymmetric disturbance ($n = 1$) at $x = 60$, $R = 20,000$ and $\alpha = 0.125$. The location of the critical line $U = c_r$ is shown by the dashed line. . . .	78
3.39	Production (W_+) and dissipation (W_-) rate of non-axisymmetric disturbance ($n = 1$) at $x = 200$, $R = 20,000$ and $\alpha = 0.125$. The location of the critical line $U = c_r$ is shown by the dashed line. . . .	79
3.40	Production (W_+) and dissipation (W_-) rate of non-axisymmetric disturbance ($n = 2$) at $x = 60$, $R = 20,000$ and $\alpha = 0.125$. The location of the critical line $U = c_r$ is shown by the dashed line. . . .	79
3.41	Production (W_+) and dissipation (W_-) rate of non-axisymmetric disturbance ($n = 2$) at $x = 200$, $R = 20,000$ and $\alpha = 0.125$. The location of the critical line $U = c_r$ is shown by the dashed line. . . .	80
3.42	Production (W_+) and dissipation (W_-) rate of non-axisymmetric disturbance ($n = 3$) at $x = 60$, $R = 20,000$ and $\alpha = 0.125$. The location of the critical line $U = c_r$ is shown by the dashed line. . . .	80
3.43	Production (W_+) and dissipation (W_-) rate of non-axisymmetric disturbance ($n = 3$) at $x = 200$, $R = 20,000$ and $\alpha = 0.125$. The location of the critical line $U = c_r$ is shown by the dashed line. . . .	81

3.44	Critical Reynolds number as a function of curvature for the mode $n = 1$	82
4.1	Growth rate of most dangerous secondary mode on a flat plate at a Reynolds number (R_θ) of 402.4. Solid lines: present computations; symbols: Herbert (1988). The amplitudes A_p for each curve from the bottom up are 0.002, 0.004, 0.006, 0.008 and 0.01.	88
4.2	Growth rate of secondary disturbance waves along the cylinder axis for the non-axisymmetric mode $n = 1$ at $R = 1000$ and $A_p = 0.02$. The azimuthal wave numbers of secondary modes are $m_+ = 2$ and $m_- = -1$. The most unstable primary mode is shown by the dashed line.	89
4.3	Growth rate of secondary disturbance along the cylinder axis for $R = 2000$. The other parameters are the same as in figure 4.2.	90
4.4	Growth rate of secondary disturbance along the cylinder axis for $R = 5000$. The other parameters are the same as in figure 4.2.	91
4.5	Growth rate of secondary disturbance waves along the cylinder axis for the non-axisymmetric mode $n = 2$ at $R = 3000$ and $A_p = 0.02$. The azimuthal wave numbers of secondary modes are $m_+ = 4$ and $m_- = -2$	91
4.6	Growth rate of secondary disturbance along the cylinder axis for $R = 5000$. The other parameters are the same as in figure 4.5.	92
4.7	Growth rate of secondary disturbance waves along the cylinder axis for the non-axisymmetric mode $n = 3$ at $R = 5000$ and $A_p = 0.02$. The azimuthal wave numbers of secondary modes are $m_+ = 6$ and $m_- = -3$	93
4.8	Growth rate of secondary disturbance along the cylinder axis for $R = 10,000$. The other parameters are the same as in figure 4.7.	93
4.9	Axial component u_+ of the secondary disturbance. The Reynolds number is 1000, $n = 1$, $\alpha = 0.14$, $x = 200$, $k_+ = k_- = \alpha/2$. A_p of primary wave A_p is taken as 0.02. The solid and dashed lines are real and imaginary part respectively.	94
4.10	Axial component u_- of disturbance velocity. The parameters are same as the figure 4.9.	94

4.11	Radial component u_+ of disturbance velocity. The parameters are same as the figure 4.9.	95
4.12	Radial component u_- of disturbance velocity. The parameters are same as the figure 4.9.	95
4.13	Azimuthal component w_+ of disturbance velocity. The parameters are same as the figure 4.9.	96
4.14	Azimuthal component w_- of disturbance velocity. The parameters are same as the figure 4.9.	96
4.15	Growth rate of most dangerous secondary sub-harmonic mode at a Reynolds number $R = 600$ (based on the momentum thickness of the boundary layer and U_∞). Solid line: $m = -0.06, k_+ = 0.14$, dashed line: $m = 0, k_+ = 0.085$	98
5.1	Growth of the intermittency parameter F in flat plate flow. Symbols: experiment Dhawan & Narasimha (1958).	105
5.2	Adverse pressure gradient, $m = -0.05$. Symbols: experiment Gostelow & Blunden (1988); lines: best fit for data, depict observed sub-transition. L is the distance from x_t at which $\gamma = 99\%$	106
5.3	Schematic diagram of the simulation domain. This figure corresponds to a random breakdown scenario, where spots appear according to a Poisson distribution in time, and are uniformly distributed in the spanwise direction.	109
5.4	Schematic diagram of the simulation domain with a regular breakdown. Spots are formed at regular intervals in the spanwise direction and are staggered after every time period, as dictated by the secondary instability. The harmonic arrangement is shown here.	110
5.5	Variation of intermittency parameter in harmonic breakdown for $N_z = 49$ and $N_t = 10$. Symbols: regular breakdown, solid line: random breakdown. The mean spot generation rate is $N = 0.01$ in both cases. The dashed line shows the best linear fit for the downstream part of F	112
5.6	Variation of intermittency parameter for $N_z = 10$ and $N_t = 49$. Symbols: regular breakdown. All other parameters are same as in figure 5.5.	113

5.7	Variation of the intermittency in an adverse pressure gradient flow, $m = -0.06$. Solid line: stochastic simulations, with $N_z = 49, N_t = 10$, in accordance with the wavelengths of the dominant secondary mode; symbols: experiments (Gostelow & Blunden, 1988).	116
5.8	Variation of the parameter F for the data shown in figure 5.7. The dashed lines are the best fit of the observed F , as proposed in the sub-transition model of Narasimha (1985).	116
5.9	Variation of the intermittency in an adverse pressure gradient of $m = -0.04$. Solid line: stochastic simulations with $N_z = 39, N_t = 12$, from in accordance with the wavelengths of the dominant secondary mode; symbols: experiments (Gostelow <i>et al.</i> , 1994).	117
5.10	Variation of the parameter F for the data shown in Figure 5.9. (Gostelow <i>et al.</i> , 1994).	118
5.11	Transition through a bypass mechanism, streak breakdown. Symbols: experiment Matsubara & Alfredsson (2001); line: regular breakdown, $N_z/N_t = 5$	119
5.12	The variation of the breakdown ratio (N_z/N_t) as determined by the most unstable secondary instability with adverse pressure gradient (m).	120
5.13	Variation of intermittency parameter F in the boundary layer over a flat plate. Solid line: stochastic simulations with $N_z = 32, N_t = 13$ as dictated by secondary instability; dots are the experimental data in zero pressure gradient boundary layers from Dhawan & Narasimha (1958).	122
5.14	The variation of amplitude of secondary disturbance wave with time in adverse ($m = -0.06, \alpha = 0.185$ and $\beta = 0.12$, solid line) and zero ($\alpha = 0.13$ and $\beta = 0.805$, dashed line) pressure gradient boundary layers.	122
5.15	Variation of the burst rate with the intermittency γ for different scenarios of spot breakdown. Symbols: Random breakdown according to Poisson distribution, Solid line: equation 5.1, Dashed line: regular breakdown.	124
5.16	Probability density function (pdf) of 'persistence time w_t '.	125

5.17	Effect of the hypothesis of concentrated breakdown on the intermittency distribution. Solid line: spots are allowed to form only at x_t . Dashed line: 80% spots are born downstream of the onset location. Dot-dashed line: all spots form downstream of the transition onset (Emmons breakdown). The x -axis is scaled with $x_{\gamma=0.99}$	127
5.18	Effect of concentrated breakdown on persistence time distribution. The persistence time is computed at the location where intermittency $\gamma = 0.1$. The curve marked R2 is according to the hypothesis of concentrated breakdown, R1 is for random breakdown anywhere downstream of x_t (Emmons, 1951), P1 represents periodic breakdown (sub-harmonic), the pattern is obtained from secondary instability.	127
5.19	Effect of the calmed region behind a spot on the intermittency for a random breakdown scenario. C0 is for simulations without a calmed region. In the scenario C1 each spot is followed by a calmed region. The x -axis is scaled with $x_{\gamma=0.99}$	128
5.20	The intermittency parameter F for the results shown in figure 5.19.	129
5.21	Burst rate plotted against intermittency. C0 is without considering the effect of the calmed region. In the scenario C1 each spot is followed by a calmed tail. The maxima are scaled arbitrarily. . . .	130
5.22	The intermittency factor F Vs. X , for different circumferences of the cylinder. The straight line is the result of two-dimensional simulations with the same spot birth rate.	131
5.23	The burst rate in the transition zone of the boundary layer around a cylinder.	131

]

]

]

List of Tables

3.1	Critical Reynolds number and other parameters for different modes, in comparison with Tutty <i>et al.</i> (2002). The streamwise location where instability first occurs is denoted as x_c . α_c and c_r are the streamwise wavenumber and phase speed corresponding to the critical Reynolds number.	67
5.1	Typical phase and group velocities in Blasius and decelerating boundary layers.	121
5.2	Effect of the primary disturbance amplitude on the obliqueness of the most dangerous mode.	123

Contents

Preface	vii
Nomenclature	xi
List of Figures	xxi
List of Tables	xxiii

I Instabilities in an axisymmetric boundary layer

1 Introduction	3
1.1 A brief history of stability of shear flows	7
1.1.1 Highlights of progress in the last decade	12
1.2 The transition zone	17
1.3 Boundary layer over a curved surface	18
1.3.1 Squires theorem and effect of curvature	19
1.4 Review of literature on axisymmetric boundary layers	20
1.4.1 Incompressible boundary layers	20
1.4.2 Compressible boundary layers	22
1.5 Scope of the present work	23
2 The basic laminar boundary layer	25
2.1 Thick cylinders	26
2.2 Navier-Stokes solution with the boundary layer approximation . . .	28
2.2.1 Code validation	29
2.2.2 Dependence of mean flow on curvature	32
2.2.3 Does similarity exist?	36

2.2.4	Momentum thickness	37
3	Linear Stability Analysis	41
3.1	Formulation of the stability problem	41
3.1.1	Linear stability equations	41
3.1.2	Boundary conditions	45
3.1.3	Energy Balance	45
3.2	Inviscid stability characteristics	47
3.2.1	Governing Equations	47
3.3	The eigenvalue problem and its numerical solution	51
3.3.1	Grid stretching	52
3.4	Stability results: thick cylinders	53
3.5	Linear stability results: cylinders of arbitrary radius	66
3.5.1	Energy balance	75
3.6	Summary of linear instability studies	77
4	Secondary Instability Analysis	83
4.1	Governing Equations	84
4.1.1	Secondary instability equations	85
4.2	Method of solution	87
4.3	Results and discussions	88
4.4	Secondary instability analysis of two-dimensional boundary layers	97

II The transition zone

5	Transition modelling in boundary layers	101
5.1	Introduction	101
5.1.1	Effect of pressure gradient	103
5.2	The transition zone	104
5.2.1	Qualitative difference	105
5.3	The stochastic model and simulations	107
5.4	Connection between instability and transition	115
5.4.1	Why there is no apparent connection in zero pressure gradient.	119
5.5	Measures to infer the breakdown scenario	123
5.6	Effect of concentrated breakdown	125

5.7	Effect of calmed region	128
5.8	Axisymmetric Boundary Layers	129
6	Conclusions	133
6.1	Summary of Results	133
6.2	Suggestions for future work	135
	Appendices	137
I	Chebyshev Spectral Collocation Method	137
A.1	Chebyshev Expansions	137
A.2	Differentiation in Chebyshev Plane	138
A.3	Chebyshev Discretisation of OS Equation	140
	References	143

Part I

**INSTABILITIES IN AN AXISYMMETRIC
BOUNDARY LAYER**

CHAPTER 1

INTRODUCTION

We distinguish the state of flow as laminar or turbulent based on its nature. Laminar flow is one in which fluid particles flow in an orderly fashion, whereas turbulent flows are characterised by irregular and chaotic motion. The presence of a wide range of spatial and temporal scales, large diffusivity and 3-dimensional vorticity fluctuations are some of the other salient features of turbulence. The state of the flow being laminar or turbulent drastically affects quantities such as skin friction, form drag, heat transfer rates etc. Laminar flow is preferred in certain conditions, say, the flow over an airfoil, since this offers the prospect of reducing the drag by a significant amount, which in turn saves enormous amount of fuel. Another advantage of laminar flow is the reduced pressure-fluctuation-induced wear and noise in fluid engineering applications. On the other hand, there are situations where turbulent flow is desired, say in a combustion chamber where the fuel needs to be mixed thoroughly. So, from a scientist's or an engineer's point of view, it is very important to be able to predict transition from the laminar to the turbulent state, which still seems a Herculean task quite often.

The laminar to turbulent transition has therefore been a subject of great interest for several decades. Traditionally theoretical investigations for explaining this transition were based on the premise that the first step in the transition process is the destabilisation of laminar flows by small disturbances. Thus, the classical starting point has been linear stability, which deals with the growth/decay of tiny

disturbance waves in space and/or time. Stability analysis of laminar flows has been avidly pursued over many decades and the area has grown significantly in the last 40 years. The study of stability and transition mainly deals with two kinds of flows: (i) those which are dominated by volume forces such as gravity and (ii) those subjected to shear forces. The well-known Rayleigh-Benard instability, in which a fluid layer is heated from below in the presence of gravity, and Taylor-Couette flow (driven fluid flow between two rotating concentric cylinders) are examples of the first kind. Plane Couette flow and boundary-layer flow come under the second category, where the instability is due to the shearing of fluid. In this category, most attention has been focussed on the boundary layer over a two-dimensional surface. This is because a major motivation for understanding transition in open flows came from the aircraft industry, for the design of laminar airfoils, and in turbomachinery blades. A fundamental understanding of the laminar-turbulent transition process can lead to improved transition prediction techniques and eventually to transition control methodologies. However, our current understanding of the physical processes involved is far from complete, except in a few text-book flows. A detailed review has been given in the books by Chandrasekhar (1961), Drazin & Reid (1981), Huerre & Rossi (1998), Lin (1955) and Schmid & Henningson (2001).

The transition to turbulence in open flows is a process that usually occurs in a sequence of events. A schematic picture of the 'standard' sequence of events that lead to transition from laminar to turbulent flow in a flat plate boundary layer is given in figure 1.1.

The process begins with *receptivity*, in which a laminar flow receives disturbances from the free-stream or from the surface roughness. This is considered as the most difficult stage to include in transition prediction models. Even in the 'quietest' of flows, the free-stream consists of stochastically occurring perturbations,

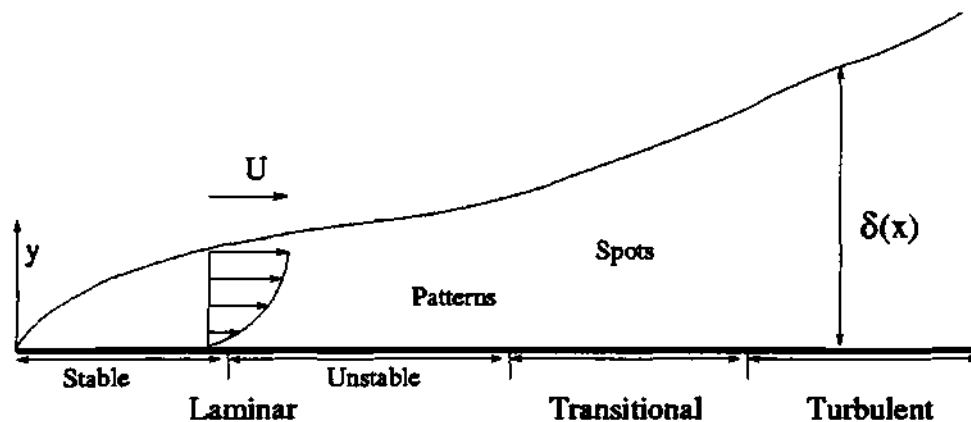


Figure 1.1: Schematic diagram of the sequence of events in laminar-turbulent transition process on a boundary layer in the flow past a semi-infinite flat plate.

typically of small amplitude. The receptivity mechanism includes the entrainment of such disturbances into the boundary layer and how they force disturbance growth inside. Transition can vary dramatically with the external noise and its receptivity. There is a lot of recent work on the receptivity problem (see e.g. Hunt *et al.*, 1996; Jacobs & Durbin, 1998). The freestream supports both discrete and continuous disturbance eigenmodes. These studies showed that the amplitude of continuous modes damps out rapidly inside the boundary layer, whereas eigenfunction of discrete modes decays slowly. The inability of continuous modes of free-stream turbulence to penetrate the boundary layer has been termed as “shear sheltering”.

The next stage is the *amplification* of disturbance waves. Depending on the local Reynolds number, disturbances lying within a narrow range of frequencies may grow. This stage can often be described by linear hydrodynamic stability theory and has been extensively studied especially for two-dimensional flows. An appropriate Reynolds number in this case would be $R \equiv UL/\nu$, where U is the local free stream velocity, ν is the kinematic viscosity and L is a local length scale (it could be, for example, the boundary layer thickness δ or the momentum thickness

θ). Once these linear disturbances have grown to a certain amplitude, they are able to destabilize three dimensional secondary modes, giving rise to Λ vortices (see Bech, Henningson & Henkes, 1998; Reed & Saric, 1996; Saric, Reed & White, 2003). As a thumb rule the non-linearity becomes detectable when the amplitude of the primary disturbance becomes of the order of 1% of the mean flow.

The last stage in the transition process is the non-linear growth of the three-dimensional waves and their breakdown into turbulence. This consists of a succession of events (all of which are not completely understood even in a two-dimensional boundary layer) that cause the breakdown of the flow into occasional isolated patches of turbulence, known as turbulent spots. The streamwise location where spots first originate can be defined as the onset of transition. The spots grow both in the streamwise and spanwise directions as they convect downstream with the flow; in this process they often merge with neighbouring spots, until the flow asymptotically becomes fully turbulent.

The processes that occur depend specifically on given flow situations, some steps can be more significant than the others, and some steps may be bypassed. So the stages cannot be expected to happen always in the above sequence, even in a two-dimensional boundary layer. At high freestream turbulence levels the 'bypass' mechanism predominates, a detailed discussion on is included in 1.1.1. Another interesting deviation occurred in the investigations of Kachanov *et al.* (1977), where two-dimensional disturbance waves were observed till the late stages of the non-linear process; and transition occurred without the formation of turbulent spots. They termed this an 'evolutionary transition.' Here fully developed turbulence is obtained by the gradual filling up of the disturbance spectrum. However, in most other experiments on boundary layers a breakdown of the flow into turbulent spots seems indispensable (see Morkovin & Reshotko, 1989).

1.1 A brief history of stability of shear flows

In this section the status of our understanding of this problem upto the early 1990's is traced. In the last decade the area has witnessed explosive growth which will be discussed in section 1.1.1. The essential problems in hydrodynamic stability were identified and formulated in the 19th century mainly by von Helmholtz (1868), Kelvin (1871), Reynolds (1883), and Rayleigh (1880). Through his classical pipe flow experiments, Reynolds studied the transition process and showed that laminar flow breaks down and turbulence ensues when a dimensionless number R (which is named after him) exceeds some critical value. For a given geometry and flow rate this means that decreasing the viscosity increases the tendency of a laminar flow to destabilise. Almost at the same time Rayleigh studied theoretically the stability of shear flows to infinitesimal perturbations. From an inviscid analysis he showed that an inflexion point in the base flow velocity profiles is a necessary condition for instability. Later Tollmien (1935) showed that the presence of an inflexion point in the velocity profile is a sufficient condition for the presence of amplified waves. However, it is now well known that flows without inflexion points (e.g. the Blasius profile) can also be unstable. Here viscosity is the reason for the generation of instability. Viscosity thus plays a dual role.

In their pioneering work, Orr (1907) and Sommerfeld (1906) derived the famous Orr-Sommerfeld (OS) equation for the stability of viscous parallel laminar flows. Subsequently, the attention of many researchers turned to flow instability based on the OS equation and its solutions. The first reported solution of this equation was given by Heisenberg (1924), who used a heuristic approximation to show that the flow becomes unstable for a finite Reynolds number. He could locate four points on the neutral stability curve. Later, Tollmien (1929) and Schlichting (1933) gave

solutions to the OS equation in the form of two-dimensional eigenfunctions, which predict the existence of disturbance waves, now known as Tollmien-Schlichting (TS) waves. Squire (1933) showed that two-dimensional disturbances are more unstable than three-dimensional ones, which is discussed in detail 1.3.1.

In spite of these theoretical predictions, the existence of a wave-like growing disturbance in an actual boundary layer was a subject of debate until the landmark experiments of Schubauer & Skramstad (1947). They made velocity measurements downstream of a ribbon vibrating with a certain frequency and proved the existence of TS waves. The differences between theory and experiment were surprisingly small. However, there remained a quantitative discrepancy at the bend in the neutral stability boundary, which was unexplained until the early 1990's, although much theoretical effort was directed towards explaining it. In the early analyses, a locally parallel boundary layer was assumed, while actually a boundary layer slowly grows in the streamwise direction. Several workers suggested that the parallel-flow assumption may be the reason for the discrepancy. After many years of trying to account for non-parallel effects to explain the discrepancy, such as by Barry & Ross (1970) , Ross *et al.* (1970), Ling & Reynolds (1973), Gaster (1974), Saric & Nayfeh (1975), Bertolotti, Herbert & Spalart (1992) and Fasel & Konzelmann (1990), it became clear that non-parallel effects on the neutral boundary in Blasius boundary layers are extremely small. Klingmann *et al.* (1993) settled the issue in their experiments when they obtained a neutral stability boundary very close to the theoretical one. They demonstrated that the earlier experiments were likely to have contained small gradients in pressure close to the leading edge, which would have given rise to the observed differences in the stability boundary.

The disturbances we have discussed are two-dimensional but turbulence is three-dimensional. Thus, a fundamental question is, how does three-dimensionality arise

from growing two-dimensional waves. Tani (1969) suggested that the onset of three-dimensionality is due to non-linear effects of finite amplitude disturbances. In their experiments, Klebanoff *et al.* (1962) found high frequency pulsations using oscilloscope traces of TS waves. These were due to the three-dimensional distortion of plane TS waves. With the emergence of three-dimensionality, the growth rate of the disturbance waves departed from the predictions of linear stability analysis. They suggested that a shear layer in which growing two-dimensional modes exist has a stronger ability to amplify small three-dimensional disturbances, and proposed a mechanism of breakdown which is now known as *K*-type transition. In this scenario, patches of Λ shaped vortices, which are aligned one behind the other in the streamwise direction, form and convect downstream. The periodic array of Λ vortices has a streamwise wavelength equal to the initial two-dimensional TS wavelength (λ_{TS}). It is characterised by the appearance of peaks and valleys in the spanwise distribution of velocity, and is commonly referred to as “peak-valley splitting”. Another type of breakdown was observed in the experiments carried out in Novosibirsk by Kachanov, Kozlov & Levchenko (1977), where the Λ vortices were staggered. Later Herbert (1988) gave a theoretical explanation for this staggered pattern of Λ vortices in terms of subharmonic instabilities. This type of breakdown is known as N-type/H-type (for Novosibirsk/Herbert). In this staggered arrangement the streamwise wavelength of Λ vortices is equal to twice the initial two-dimensional TS wavelength. A sketch of these two types of breakdown scenario is given in figure 1.2. An extensive review of the physical mechanisms involved can be found in Kachanov (1994). Saric & Thomas (1984) showed from their experiments on a Blasius boundary layer that the amplitude of the plane wave determines the pattern of Λ vortices that results. The subharmonic type is a characteristic of natural transition, as the initial disturbance amplitude required is only half of the

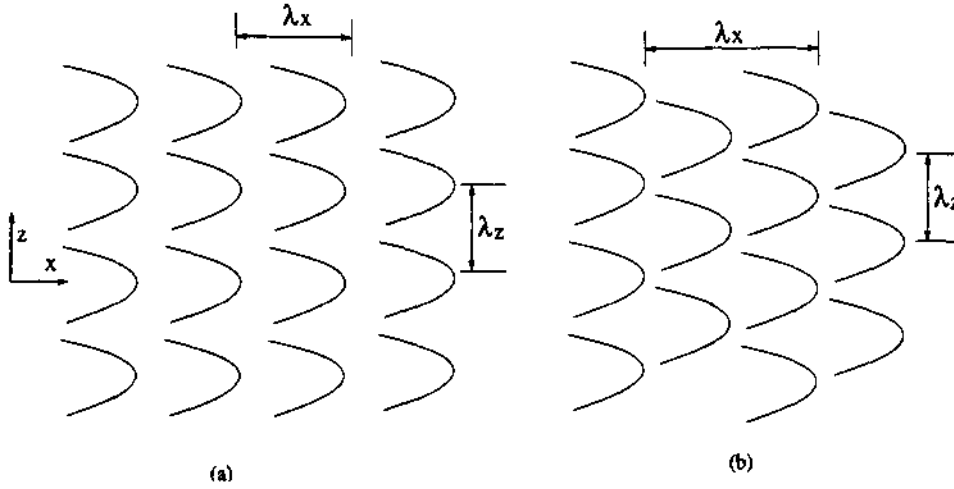


Figure 1.2: Schematic diagram of two patterns of three-dimensionality, (a) *K*-type breakdown where the streamwise wavelength of Λ vortices is equal to that of the two-dimensional TS waves ($\lambda_x = \lambda_{TS}$). (b) *N*-type/*H*-type breakdown: the wavelength of three-dimensional pattern is double the TS wavelength ($\lambda_x = 2\lambda_{TS}$).

threshold amplitude for a *K*-type breakdown. The *N*-type breakdown also has a higher growth rate. Both these scenarios have been observed in experiments (see Wazzan, 1975). However, the presence of low-amplitude streamwise vorticity in the background flow in experiments leads quite often to a *K*-type breakdown. Another non-linear mechanism, namely, the triad resonance model of Craik (1971) is caused by two oppositely-oriented oblique OS modes that are phase locked to the primary two-dimensional TS disturbance. He showed that a quadratic interaction between the oblique waves can produce a resonance with the primary wave. In this *C*-type breakdown there is again a staggered arrangement with the streamwise wavelength of Λ vortices, the same as that of the *N*-type. However, the spanwise wavelength is almost double that of the *N*-type.

The Λ structures in the *K* and *H*-type are a signature of secondary instability. Upstream the boundary layer already contains TS modes of significant amplitude,

and is thus periodic in nature. This periodic flow is now unstable to secondary three-dimensional modes. A Floquet analysis enables one to predict these (Herbert, 1988). The secondary modes, as will be discussed in chapter 4, consist of pairs of waves of opposite obliqueness, the sum of whose wavenumbers is equal to that of the primary TS mode. In most situations either harmonic (corresponding to *K*-type pattern) or subharmonic (corresponding to the *H*-type pattern) modes predominate. Since the secondary instability leads to disturbance growth on a fast convective time scale, it is closely related to the breakdown into turbulent spots.

When the Λ vortices are sufficiently energetic, they induce the flow to break down into turbulent spots. The spots in turn grow and merge with one another as they convect downstream (Emmons, 1951), until the entire boundary layer is turbulent. In short, streamwise region between the laminar flow with growing secondary modes and the transition zone, which contains concentrated patches of turbulence in laminar surroundings, the flow has changed character; although it is not fully clear how.

There are different empirical methods for predicting transition onset as defined by the location where turbulent spots first originate. The simplest relation was proposed by Michel (1952), which is based on the local momentum thickness (θ); and is given by

$$R_{\theta, tr} = 2.9 R_{x, tr}^{0.4} \quad (1.1)$$

where R_{θ} and $R_{x, tr}$ are the Reynolds numbers based on local momentum thickness and the streamwise location at transition onset respectively. Later van Ingen (1956) and Smith & Gamberoni (1956) independently proposed a new correlation based on the local amplification of TS waves. Their model is known as the e^N -method and is still widely used primarily in the aircraft industry. Transition onset is said to

occur when the maximum amplitude of linear disturbances has grown to e^N times that at the beginning of amplification, where N is a number that depends on the geometry and nature of the flow. The onset of transition depends on a number of other variables as well, such as freestream turbulence, pressure gradients, surface roughness, curvature etc. Typically, for a boundary layer on a flat plate, the value of N is found to be between 4 and 30, which means that transition occurs when the most amplified initial disturbance has grown by a factor in between 55 and 10^{13} . At high levels of environmental disturbance, N can even be negative. This is indicative of transition through the bypass mechanism. Even today it is impossible to predict transition onset from first principles.

1.1.1 Highlights of progress in the last decade

Recent theory and observations have indicated that transition in shear flows can take place due to a variety of alternate mechanisms. Free-stream turbulence is a major parameter which affects the nature of transition in the boundary layer. It may be defined as

$$q \equiv \left(\frac{\overline{\hat{u}_i \hat{u}_i}}{3U_\infty^2} \right)^{1/2} \quad (1.2)$$

where \hat{u}_i are the components of velocity perturbation outside the boundary layer, so q is a measure of how noisy the external flow is. If the background disturbances are very low (say, $q \sim 0.005$ or less), transition is likely to occur through the amplification of TS waves and subsequently the secondary instabilities. At higher values of free-stream turbulence the conventional TS wave mechanism can be “bypassed”. An important bypass mechanism is via the algebraic growth of disturbances, and the breakdown of a pair of oblique waves.

An instance of algebraic growth of disturbances was provided by Ellingsen &

Palm (1975) for an inviscid flow. Landahl (1975, 1980) showed that spanwise inhomogeneities are formed when *streamwise vortices* advect the meanflow alternately towards and away from the wall. He called this the *lift-up mechanism*, wherein the shear layer retains its horizontal momentum when displaced in a direction normal to the wall, producing narrow elongated regions of alternate low and high streamwise velocity, termed as *streaks*. The streaks are three-dimensional quasi-stationary deformation of streamwise velocity. Their characteristic shape in a boundary layer is visualised by Boiko (2002). Much of the early work on bypass transition focussed on pipe and channel flows (see e.g. Trefethen *et al.*, 1993). This is because in these flows the TS route could not be followed. In channels the flow is linearly unstable above a Reynolds number of 5772.2, whereas transition occurs usually at a Reynolds number of around 1500 (see e.g. Davies & White, 1928; Kao & Park, 1970; Narayanan & Narayanan, 1967; Patel & Head, 1969). Pipe flows are linearly stable at all Reynolds numbers (e.g. Davey & Drazin, 1969; Lessen *et al.*, 1968), while transition to turbulence takes place at around $R = 2100$ as seen already by Reynolds in 1883. The transient growth mechanism discussed below was found to be responsible in these cases (Reshotko, 2001; Schmid & Henningson, 1994). It was in the famous work of Trefethen *et al.* (1993), where a mechanism of algebraic growth that could lead to transition to turbulence, was explained. A shear flow contains a host of disturbance eigenmodes which satisfy the OS equation or variants of it. Each mode is exponentially decaying, but since the OS operator is not self-adjoint, the eigenfunctions are not orthogonal. The waves can thus interfere so that at short times the total disturbance kinetic energy grows algebraically. At long times, all the disturbances, if still behaving linearly, would of course decay exponentially, but if the temporary growth of disturbance kinetic energy is high enough, nonlinear mechanisms can take over at finite time, and drive the flow to

turbulence. This is now called the *transient growth* mechanism of transition to turbulence.

In boundary layers the likelihood of such transient growth has been studied by Andersson *et al.* (2001); Boiko *et al.* (1994); Brandt *et al.* (2003); Brandt & Henningson (2002); Luchini (2000); Matsubara & Alfredsson (2001). It is found that in high-disturbance environments, bypass is the preferred route to turbulence. This is because algebraic growth can then be of sufficient magnitude to activate a transition to turbulence (Schmid & Henningson, 2001). Secondly, at moderately high free-stream turbulence levels the amplification of TS waves is found to be small as compared to their growth in low disturbance environments (Boiko *et al.*, 1994). Several experiments have shown that transition can occur at a much lower Reynolds number than that predicted from linear theory.

These studies confirm that perturbations manifested as streamwise streaks show the highest potential for transient energy amplification. The corresponding spanwise spacing is of the order of the boundary layer thickness (Andersson *et al.*, 1999). Once the streaks reach certain amplitude, they could again be subject to secondary instability from random disturbances. This secondary instability deforms the streaks in the manner shown in figure 1.3 and causes the breakdown to turbulence. The experiments by White (2002) on flat plate boundary layer show that the qualitative behaviour of transient growth is as predicted by theory. However, there are quantitative discrepancies such as in the location of the maximum in wall-normal disturbance velocity profiles and the streamwise location of the maximum energy growth. Boiko & Chun (2004) found that the experimental value of spanwise wavenumber (β) is much smaller than that predicted by theory. The recent investigations of Fransson *et al.* (2004) confirm the findings of White (2002). It is suggested that the discrepancies arise from spanwise vortices generated by

roughness elements in the experiments. They concluded that experimentally generated streaks of amplitude larger than a certain value are stable to inflectional secondary instability. The studies by Corbet & Bottaro (2000) on Falkner-Skan profiles reveal that the largest transient amplification results again from stream-wise vortices, as in a Blasius boundary layer. The adverse pressure gradient causes increase in the optimal growth.

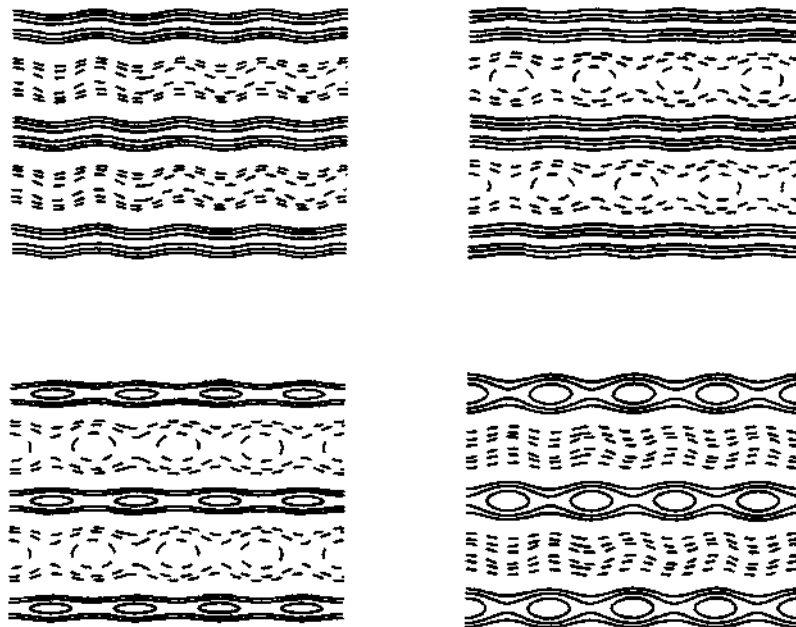


Figure 1.3: Sketch of contours of streamwise velocity in instability modes of streaks. Solid lines represent the low-speed streaks and dashed lines are for the high-speed streaks. The fundamental modes are shown in the left, while the subharmonic modes are shown in the right (from Schmid & Henningson, 2001).

Oblique transition is initiated by two oblique waves of opposite wave angles. The non-modal growth of disturbances plays an important role in this scenario as well. There are some similarities in structure in the later stage of oblique transition to those found in K-type or H-type of transition (Schmid & Henningson, 2001).

It has recently been demonstrated both theoretically and experimentally in internal flows that non-linearities appearing in the form of travelling waves provide a self-sustaining mechanism for transition to turbulence (see e.g. Faisst & Eckhardt, 2003; Hof *et al.*, 2004; Waleffe, 2001). The role of this mechanism, if any, in open flows is unclear. These experiments demonstrate the existence of finite amplitude disturbances arranged in specific patterns in the cross-section. In the experiments of Prigent *et al.* (2002) in plane Couette flow and Taylor-Couette flow, localised patches of turbulence in the form of spirals and spots were observed which formed a finite-wavelength pattern. They found that this spatial modulation of turbulent intensity obeys the dynamics of coupled amplitude (Ginzburg-Landau type) equations with noise.

The natural question thus is ‘which one of the above is the most likely transition scenario?’ The answer depends strongly on the type of flow, the initial disturbance energy, the time taken for reaching the threshold amplitude for transition, and the energy required to reach the turbulent state (Schmid & Henningson, 2001). In pipe and channel flows, a non-linear growth triggered by streaks and oblique waves are suggested to be the most likely mechanism. These are in turn generated by the transient growth of superposed linear eigenmodes. At very low turbulence Nishioka *et al.* (1975) proved the validity of linear TS mechanism in channel flow. They were able to achieve laminar flow upto a Reynolds number of ~ 8000 . In Couette flows and pipe flows the mechanism has to be other than the TS, since these flows are linearly stable at any Reynolds number. In a boundary layer, the linear mechanism and the successive breakdown to spots is the most favoured at low to moderate levels of free-stream turbulence, while at high disturbance environments transition happens through bypass mechanisms such as streaks or oblique breakdown.

1.2 The transition zone

At a streamwise location, where the disturbance amplitude reaches a requisite finite value, turbulent spots begin to be born. This is defined as the location x_t of transition onset. Narasimha (1957) made the hypothesis of concentrated breakdown, according to which most turbulent spots originate within a narrow spanwise strip around x_t . This hypothesis has been validated by a large number of experiments (in section 5.6 we discuss this further). The transition zone is easiest to describe quantitatively in terms of the variation in the streamwise coordinate, x , of the intermittency, γ , which is defined as the fraction of time for which the flow is turbulent. With spots appearing randomly in accordance with a Poisson distribution in time and a uniform distribution in the spanwise coordinate z , γ would vary downstream as (Narasimha, 1957)

$$\gamma = 1 - \exp \left[\frac{-n\sigma}{U} (x - x_t)^2 \right], \quad (1.3)$$

$$\text{or } F \equiv \sqrt{-\log(1 - \gamma)} = \sqrt{\frac{-n\sigma}{U}} (x - x_t) \quad (1.4)$$

such that the intermittency parameter F varies linearly in x . Here U is the free stream velocity, n is the number of spots forming per unit z , per unit time, at x_t . The shape and downstream growth of turbulent spots is experimentally observed to be similar in all pressure gradients: a turbulent spot maintains an arrowhead shape when viewed from above, and remains self-similar as it grows (Narasimha, 1985; Seifert & Wygnanski, 1995). It is convenient therefore to define a non-dimensional spot propagation parameter as

$$\sigma = \left[\frac{1}{U_r} - \frac{1}{U_h} \right] U \tan \zeta, \quad (1.5)$$

where ζ is the angle subtended by the spot at its origin, and U_h and U_r , respectively are the speeds with which its head and rear convect. A schematic diagram of spot growth in a flat plate boundary layer is given in figure 1.4.

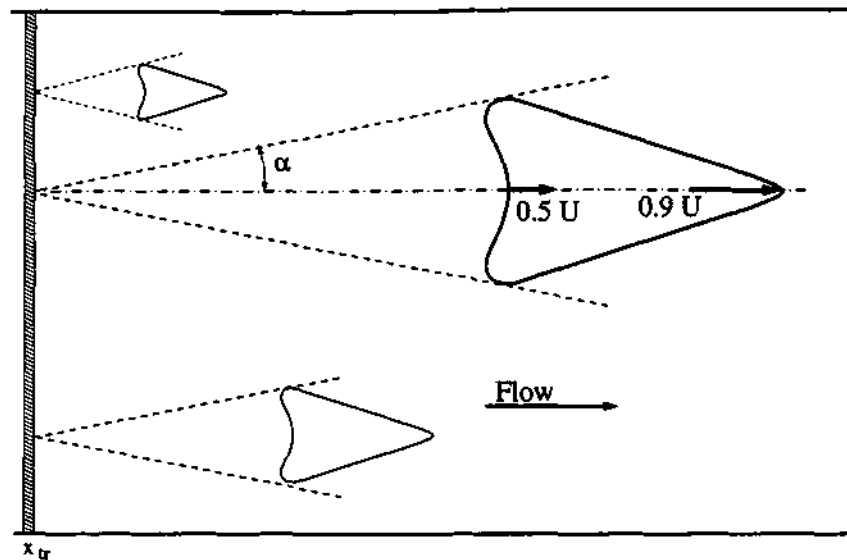


Figure 1.4: Schematic diagram of the growth of turbulent spots in the transition zone in a flat plate boundary layer.

1.3 Boundary layer over a curved surface

So far, the discussion was about boundary layers over two-dimensional bodies. In boundary layers over curved surfaces the process could be of a different character. The effects of longitudinal and of transverse curvature constitute an interesting class of problems. In engineering applications such as flow past underwater bodies, the effects of transverse curvature may be crucial. The focus of this thesis is transverse curvature and its role in the early stages of transition to turbulence. As the simplest case we consider the flow past cylinders. The equations and approach derived here, however, can be used for arbitrary axisymmetric bodies.

The boundary layer over a curved body is qualitatively different from that on a flat plate. Many studies have been carried out to understand the effect of curvature in the stability of laminar boundary layers. However, most of the work was focussed on the effect of longitudinal curvature, and the Görtler instabilities which occurred in that case. Görtler (1940) theoretically predicted the existence of a new kind of vortex in a longitudinally curved surface. His investigation was on the stability of boundary layer on concave walls, using the parallel flow approximation. He neglected higher-order curvature effects. Later, experiments by Gregory & Walker (1950) on the flap of a Griffith suction airfoil proved the existence of these vortices and the instabilities thus generated. In contrast, the effect of *transverse* curvature on the stability of laminar flows has not been studied very much.

1.3.1 Squires theorem and effect of curvature

Squire's theorem (1933) states that when the basic flow is two-dimensional, the minimum critical Reynolds number occurs in the case of a two-dimensional disturbance propagating along the same direction as the basic flow.

In this case, the three-dimensional OS equation, for a disturbance of streamwise and spanwise wavenumbers α and β respectively, can be transformed to an equivalent two-dimensional equation, with an effective wavenumber $\bar{\alpha} (= \sqrt{\alpha^2 + \beta^2})$ and a Reynolds number $\bar{R} = \alpha R / \bar{\alpha}$. Therefore for every three-dimensional wave that is destabilised, a corresponding two-dimensional wave is destabilised at a lower Reynolds number, i.e. the first instability is two dimensional.

In the presence of transverse curvature, however, the stability equations cannot be transformed in the manner proposed by Squire. A study of three-dimensional disturbances is therefore necessary for such geometries.

1.4 Review of literature on axisymmetric boundary layers

1.4.1 Incompressible boundary layers

Although the problem seems to be very simple and necessary to understand, studies of the stability of axisymmetric boundary layers are found to be very sparse in the literature. Two exceptions are Rao (1967, 1974) and Tutty *et al.* (2002), which are discussed briefly below.

Rao (1967, 1974)

This is the first reported work we could find on the stability analysis of axial flow over a cylinder. The Navier-Stokes equations were expressed in terms of generalised stream functions for axisymmetric flow that satisfy continuity, and two fourth-order differential equations for the linear stability were derived. Non-axisymmetric disturbances were found to be less stable than two-dimensional disturbances. The estimated critical Reynolds number based on free stream velocity and cylinder radius was 11,000. However, the equations used had some errors in algebra as discussed in chapter 3. Secondly the equations were not solved directly and the stability estimates had severe limitations.

Tutty, Price & Parsons (2002)

Tutty *et al.* (2002) showed that non-axisymmetric modes are less stable than axisymmetric modes. They found that a non-axisymmetric mode ($n = 1$, one az-

imuthal wave wrapped around the body) is the most unstable, and there is a large difference in the critical Reynolds number for different modes.

For all non-axisymmetric modes, i.e., for $n \geq 1$, the critical Reynolds number increases with n . The axisymmetric mode is found to be the fourth least stable. The critical Reynolds number was found to be 1060 for the $n = 1$ mode and 12439 for $n = 0$.

They solved the mean flow equations both numerically and analytically, taking into consideration the variation of velocity in the streamwise direction. The analytical velocity profile was written in terms of an asymptotic series with the leading terms satisfying the Blasius equation. They found that the second term in the expansion is of the order of $(x/R)^{\frac{1}{2}}$ and that it has a significant role in the stability for a thin boundary layer, even fairly close to the leading edge. Far downstream, the numerical mean flow follows closely the Glauert & Lighthill (1955) profiles for thin cylinders. The mean flow equation is solved at each streamwise location. The stability equations are derived using a parallel flow assumption.

Other work

The effect of curvature on stability of incompressible axisymmetric boundary layer was studied by Malik & Poll (1985). They investigated the stability of flow over a windward face of infinitely long cylinder had been investigated. They showed the body curvature and streamline curvature to have large damping effects, and found that in a three-dimensional boundary layer the most amplified waves are travelling waves.

1.4.2 Compressible boundary layers

The stability of supersonic flows past sharp cones was studied by Malik (1987) and Mack (1987) using linear theory. However, the effect of curvature was neglected in their work. Later Malik & Spall (1991) presented the viscous compressible boundary layer equations for an axisymmetric basic flow. They considered both axisymmetric and non-axisymmetric disturbances. In their experiments on blunt bodies and walls with concave curvature, Malik & Spall (1991) considered both two-dimensional and three-dimensional disturbances for studying TS and Görtler instabilities. They concluded that transverse curvature has a stabilizing effect for axisymmetric disturbances and a destabilising effect on non-axisymmetric disturbances.

Duck (1984) showed that the effect of transverse curvature becomes very small when the radius of the body is much higher than the boundary layer thickness. Duck & Hall (1989) later studied the stability of supersonic flow over axisymmetric boundary layers by considering two-dimensional as well as three-dimensional disturbances. They showed that the neutral stability boundaries show no similarity when effects of curvature are significant. Duck (1990) established, in his inviscid analysis with axisymmetric disturbances, that curvature has a stabilising effect in the flow along a circular cylinder. Duck and Shaw (1990) continued this study with non-axisymmetric disturbances and obtained inviscid growth rates. They identified the most unstable disturbances as a new mode of instability waves. Stetson *et al.* (1983) experimentally studied the stability of laminar boundary layer over a sharp cone (7° half-angle) at a Mach number 8. They showed that different unstable regions exist in the boundary layer.

1.5 Scope of the present work

As we have seen, though the effect of curvature on linear stability has been studied, the range for which the flow is unstable is not well explored. Some of the investigations only dealt with inviscid theory. Although many researchers looked into the compressible flows on axisymmetric boundary layers, there is significant difference in the results. For example Spall & Malik (1991) concluded that the transverse curvature destabilises the first non-axisymmetric mode, but stabilise the second mode. Other reports (e.g. Duck, 1984; Duck & Hall, 1989) show that transverse curvature has an overall stabilising effect on axisymmetric boundary layers. These stability computations/experiments have been performed for different Mach numbers, varying from 1.25 to 5.0.

To our knowledge the secondary instability of axisymmetric boundary layer has not been studied before. The transition zone in axisymmetric boundary layers has also not been investigated so far, except by 'Lauchle & Gurney (1984) and Govindarajan & Narasimha (2000). The aim of this thesis is to understand better the transition to turbulence in axisymmetric boundary layers. Towards this aim, we have formulated the linear and secondary instability equations and solved them. We have also made a foray into the transition zone, by making a connection between the secondary instability pattern and the birth of turbulent spots. Since this connection has not been made for two-dimensional flows either, we have expended some effort on the transition zone in two-dimensional boundary layers.

First we obtain the mean velocity profile in axisymmetric laminar boundary layers. This exercise, with examples of the results obtained, is described in chapter 2. The destabilisation of the laminar boundary layer by linear disturbances, as mentioned above, is the first step involved in the transition to turbulence. As

described in chapter 3, we conduct a stability analysis of the laminar axisymmetric boundary layer to estimate the conditions under which linear disturbances of particular frequencies begin to grow, and also to obtain the nature and rate of growth of these disturbances. Based on the present wisdom, and on present experience with non-parallel effects, we make the parallel flow assumption. The work includes the secondary instability analysis, which is described in chapter 4. In chapter 5, results from stochastic simulations of the transition zone are described.

CHAPTER 2

THE BASIC LAMINAR BOUNDARY LAYER

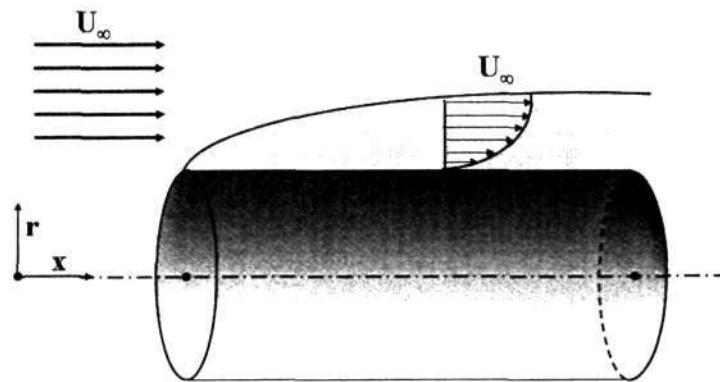


Figure 2.1: Schematic diagram showing the coordinate system.

Before we can perform stability calculations, we first need to compute the unperturbed laminar flow. The steady flow momentum equation for the axial component of velocity can be written in cylindrical polar co-ordinates as:

$$U \frac{\partial U}{\partial x} + V \frac{\partial U}{\partial r} = \frac{1}{R} \left(\frac{\partial^2 U}{\partial r^2} + \frac{1}{r} \frac{\partial U}{\partial r} \right), \quad (2.1)$$

where the x co-ordinate is along the surface of the body and r is normal to the body at each point. The respective velocity components in these co-ordinates are U, V and W . The mean flow is assumed to be steady and incompressible and it is assumed that the boundary layer approximations are valid. This means that the term $\partial^2 U / \partial x^2$ has been neglected in comparison with $\partial^2 U / \partial r^2$, and the governing

equation is now parabolic. The variation of pressure along the x -direction is zero, since the free-stream velocity is constant. The length and velocity scales used for non-dimensionalisation are the body radius, r_0 and the freestream velocity, U_∞ respectively. Then the Reynolds number is given by

$$R \equiv \frac{U_\infty r_0}{\nu}. \quad (2.2)$$

The continuity equation is

$$\frac{\partial U}{\partial x} + \frac{\partial V}{\partial r} + \frac{V}{r} = 0. \quad (2.3)$$

The boundary conditions are

$$U(x_0, r) = 1, \quad (2.4a)$$

$$U(x, 0) = 0, \quad V(x, 0) = 0 \quad \text{and} \quad U(x, \infty) = 1. \quad (2.4b)$$

It is convenient to define r as the distance from the axis (rather than the distance away from the surface).

2.1 Thick cylinders

A thick cylinder is defined here as one whose radius is much greater than the boundary layer thickness. The equation in this case may be simplified by employing a Mangler (1945) transformation, which is given as

$$x' = \frac{1}{L^2} \int_0^{x_d} r_0^2 dx_d, \quad r' = \frac{r_0(r_d - r_0)}{L}, \quad (2.5)$$

where L is a reference length and the subscript d denotes a dimensional quantity. Equation 2.1 may now be transformed to an equivalent similarity equation. For a

circular cylinder, the radius is independent of x , hence $x' = r_0^2 x / L^2$ (White, 1991).

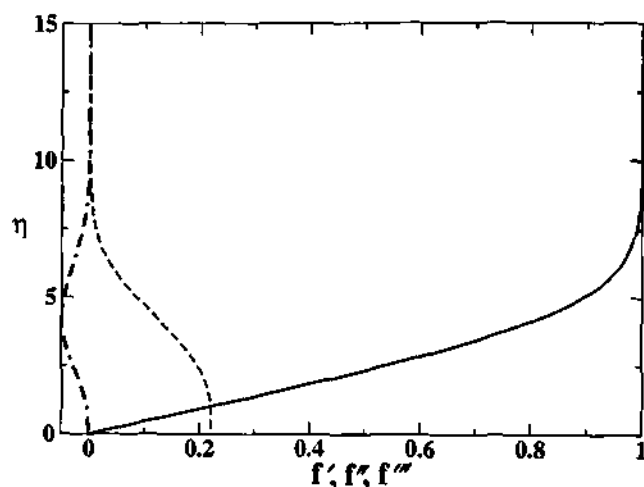


Figure 2.2: Velocity profile ($U = U_d/U_\infty \equiv f'$: solid line) and its derivatives for Blasius flow. Dashed line: the first derivative (f''); dot dashed line: second derivative (f''').

The resulting equation is of the Blasius form

$$f''' + ff'' = 0 \quad (2.6)$$

where the primes refer to differentiation with respect to $\eta = (r_d - r_0)\sqrt{U_\infty/2\nu x}$, and the non-dimensional streamfunction is given by

$$\psi = \sqrt{2U_\infty\nu x_d} f(\eta).$$

The streamwise and normal velocities can be obtained from the relations

$$U_d = \frac{\partial\psi}{\partial(r_d - r_0)} = U_\infty f'(\eta) \quad \text{and} \quad V_d = -\frac{\partial\psi}{\partial x_d} = \sqrt{\frac{\nu U_d}{2x_d}} (\eta f'(\eta) - f(\eta)). \quad (2.7)$$

The boundary conditions are

$$f = f' = 0 \quad \text{at} \quad \eta = 0, \quad \text{and} \quad (2.8)$$

$$f' = 1 \quad \text{as} \quad \eta \rightarrow \infty. \quad (2.9)$$

A fourth order Runge-Kutta scheme to solve the Blasius equation is employed and the velocity profile is shown in Figure 2.2.

2.2 Navier-Stokes solution with the boundary layer approximation

For thinner cylinders the above profiles do not hold good. Here a finite difference scheme is used to solve the momentum equation. A 3-level implicit scheme is used for solving equations 2.1 and 2.3. A uniform-grid finite-difference method is used to develop the computational algorithm. The following discretisation expressions are employed:

$$\frac{\partial u}{\partial x} = \frac{1.5u_j^{n+1} - 2u_j^n + 0.5u_j^{n-1}}{\Delta x} + O(\Delta x^2), \quad (2.10)$$

$$\frac{\partial u}{\partial r} = \frac{u_{j+1}^{n+1} - u_{j-1}^{n+1}}{2\Delta y} + O(\Delta r^2), \quad (2.11)$$

$$\frac{\partial^2 u}{\partial r^2} = \frac{u_{j-1}^{n+1} - 2u_j^{n+1} + u_{j+1}^{n+1}}{\Delta r^2} + O(\Delta r^2), \quad (2.12)$$

$$u_j^{n+1} = 2u_j^n - u_j^{n-1} + O(\Delta x^2), \quad (2.13)$$

$$v_j^{n+1} = 2v_j^n - v_j^{n-1} + O(\Delta r^2). \quad (2.14)$$

Substituting the above expressions into equation 2.1, we get

$$a_j u_{j-1}^{n+1} + b_j u_j^{n+1} + c_j u_{j+1}^{n+1} = d_j \quad (2.15)$$

where

$$a = \frac{1}{2rR\Delta r} - \frac{1}{R\Delta r^2} - \frac{2v_j^n - v_j^{n-1}}{2\Delta r}, \quad (2.16a)$$

$$b = \frac{2}{R\Delta r^2} + \frac{1.5(2u_j^n - u_j^{n-1})}{\Delta x}, \quad (2.16b)$$

$$c = \frac{2v_j^n - v_j^{n-1}}{2\Delta r} - \frac{1}{R\Delta r^2}, \quad (2.16c)$$

$$\text{and } d = \frac{-(2v_j^n - v_j^{n-1})(-2u_j^n + 0.5u_j^{n-1})}{\Delta x}. \quad (2.16d)$$

Once u_j^{n+1} is available, v_j^{n+1} can be calculated from

$$v_j^{n+1} = v_{j-1}^{n+1} - 0.5 \frac{\Delta y}{\Delta x} \left[(1.5u_j^{n+1} - 2u_j^n + 0.5u_j^{n-1}) + (1.5u_{j-1}^{n+1} - 2u_{j-1}^n + 0.5u_{j-1}^{n-1}) \right]. \quad (2.17)$$

Two levels of initial data must be provided, to start the downstream march. The equation 2.15 together with 2.17 is second order accurate in Δx and Δr , and is unconditionally stable in the von Neumann sense. A fairly fine grid in the r direction is necessary to capture the velocity and its derivative accurately, especially in the near-wall region.

2.2.1 Code validation

The present solution for large r_0 can be validated against the Blasius profile. In figure 2.3, the streamwise velocity is plotted. Figure 2.4 shows the normal velocity in the boundary layer at different streamwise locations ($x^* \equiv x_d/r_0$). The solutions

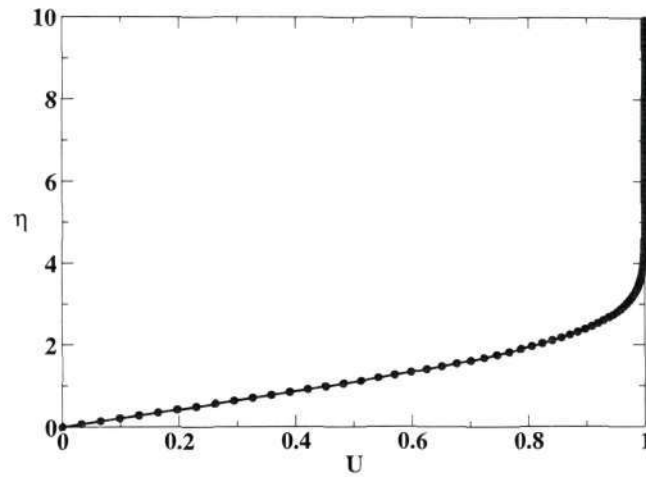


Figure 2.3: Comparison of streamwise velocity profiles. Solid line: numerical solution of equation 2.1 with $R = 5 \times 10^5$. Symbols: Blasius.

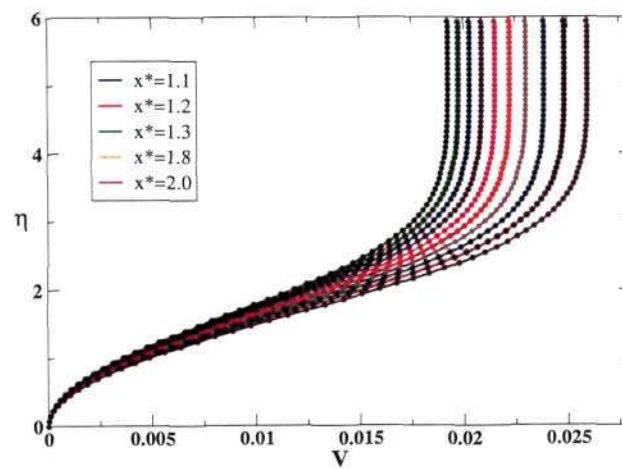


Figure 2.4: Comparison of normal velocity at different streamwise locations. The solid lines are the numerical solutions at $R = 5 \times 10^5$ and symbols are Blasius solutions.

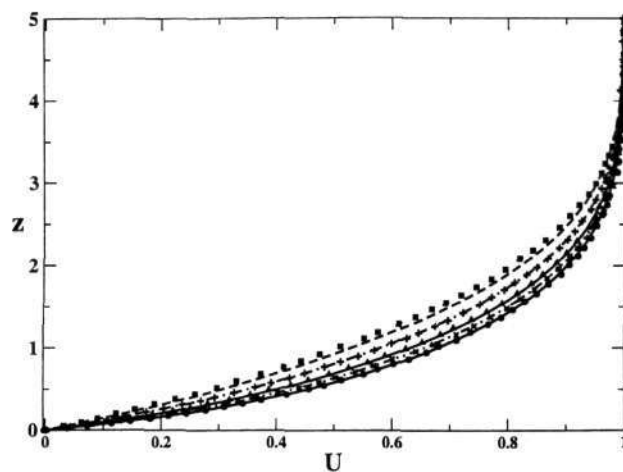


Figure 2.5: Comparison of streamwise velocity with results from Tutty *et al.* (2002) at $R = 10^4$. The ordinate shows $z = \sqrt{R/x^*}(r - 1)$. The different curves are for different streamwise locations, the lowest curve is at $x = 10^5$ and the top curve is for $x = 398$. The other curves are evenly spaced at intervals of $x^{1/2}$. The symbols are results from Tutty *et al.* (2002), while the lines are present results.

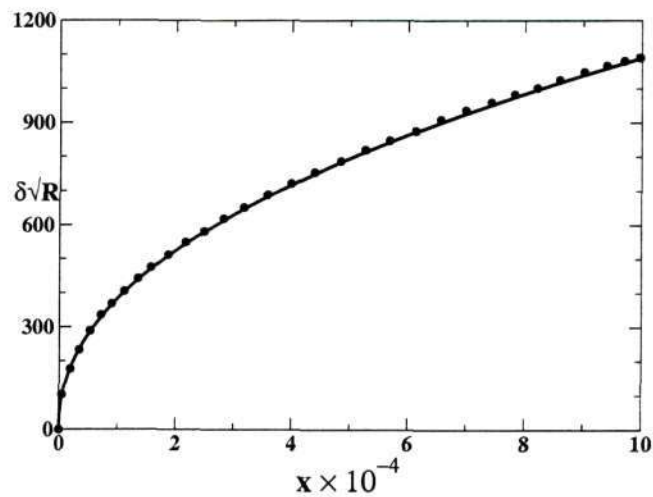


Figure 2.6: Dimensionless boundary layer thickness $\delta\sqrt{R}/r_0$ for $R = 10^4$. The solid lines are from the numerical solution of the boundary layer equations. The symbols are results from Tutty *et al.* (2002).

agree very well with Blasius. At other r_0 , present velocity profiles are compared with those of Tutty *et al.* (2002). The streamwise velocity is plotted in figure 2.5 for a Reynolds number (R) of 10,000 at different streamwise locations. The results are in good agreement. The dimensionless boundary layer thickness $\delta\sqrt{R}/r_0$ is plotted against the streamwise location in figure 2.6. The boundary layer thickness is defined as the location $\delta = r_{d_{0.99}} - r_0$, where $U_{r_{d_{0.99}}} = 0.99$. In figure 2.5 the streamwise velocity from numerical calculations is plotted against the scaled normal coordinate $z = \sqrt{R/x^*}(r - 1)$.

2.2.2 Dependence of mean flow on curvature

The streamwise velocity profiles at different locations are given in figure 2.7 for a Reynolds number of 4,000. The radial distance from the wall is scaled by the local boundary layer thickness, δ , i.e. $r^* \equiv (r_d - r_0)/\delta$. Although the velocity profiles look similar, there is a difference near the wall, which is evident from the derivatives of velocity profiles 2.8 and 2.9. This will be reflected in the stability behaviour. The boundary layer thickness increases with streamwise location. It is not possible to get a general relationship between boundary layer thickness and the streamwise location, since the equations are not similar (see Section 2.2.3).

Now we consider a higher Reynolds number of 400,000. The derivatives of velocity dU/dr^* and d^2U/dr^{*2} are plotted in figures 2.11 and 2.12. For all Reynolds numbers the value of first derivative of velocity increases at the wall downstream, while the second derivative at wall decreases. Further the value of second derivative at the wall also decreases with increase in Reynolds number.

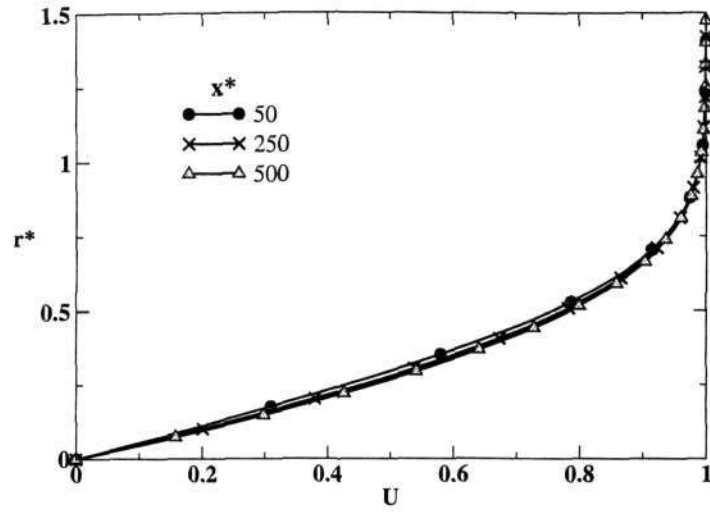


Figure 2.7: Streamwise velocity using Navier-Stokes solution for different streamwise locations, at Reynolds number=4,000.

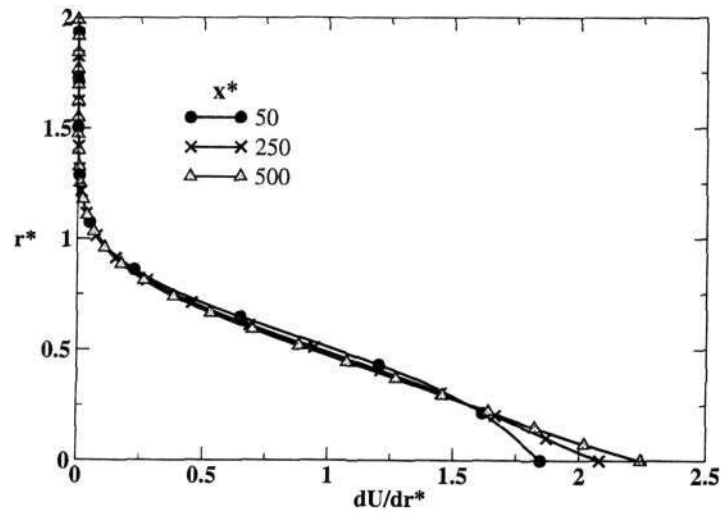


Figure 2.8: First derivative of streamwise velocity using Navier-Stokes solution for different streamwise locations, at $R = 4,000$.

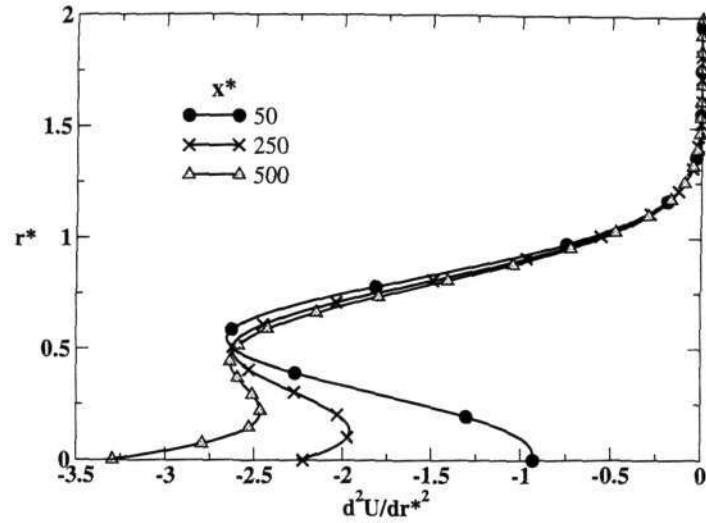


Figure 2.9: Second derivative of streamwise velocity using Navier-Stokes solution for different streamwise locations, at $R = 4,000$.

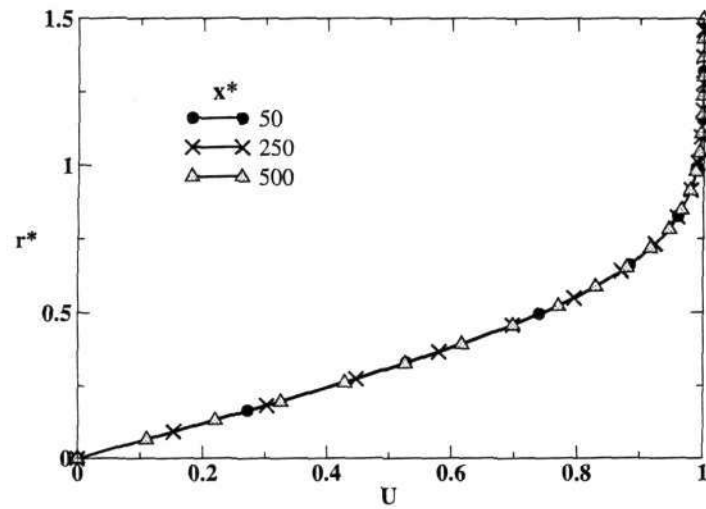


Figure 2.10: Streamwise velocity (U) for different streamwise locations, at a Reynolds number of 400,000.

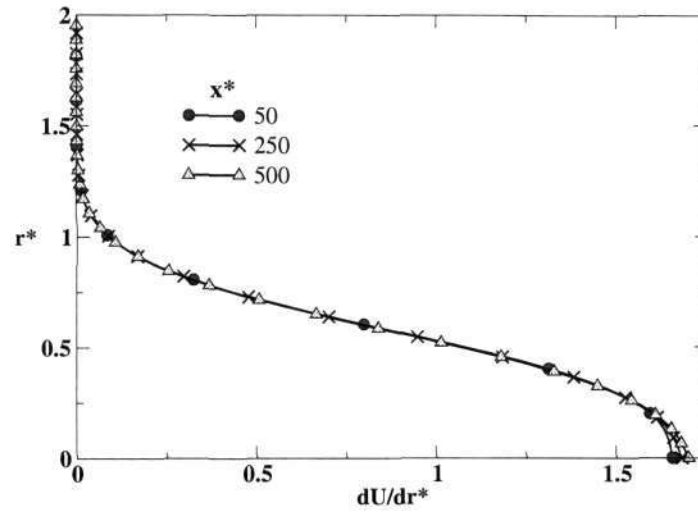


Figure 2.11: First derivative of streamwise velocity (U') for different streamwise locations, at a Reynolds number 400,000.

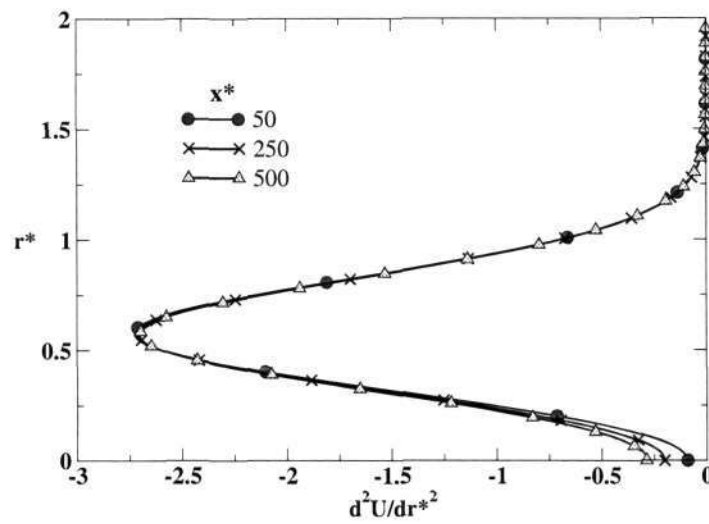


Figure 2.12: Second derivative of streamwise velocity (U'') for different streamwise locations, at a Reynolds number of 400,000.

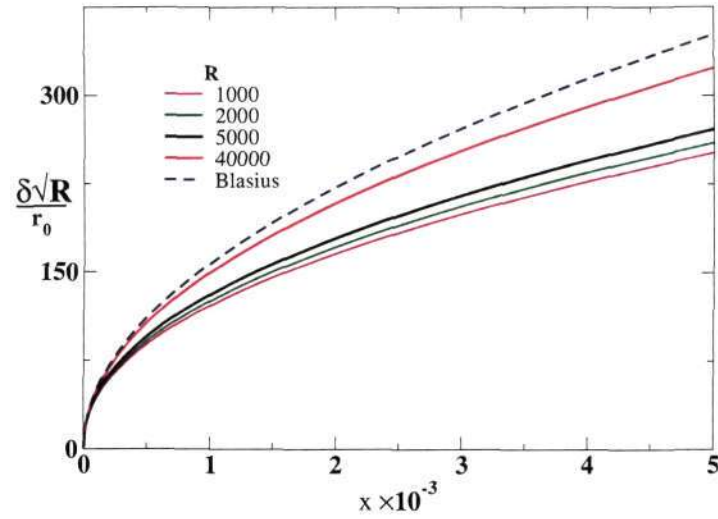


Figure 2.13: Variation of dimensionless boundary layer thickness ($\delta\sqrt{R}/r_0$) along streamwise location, for different Reynolds number.

2.2.3 Does similarity exist?

Defining a similarity parameter as in Glauert & Lighthill (1955),

$$\zeta \equiv \frac{Ur_d^2}{4\nu x} \quad (2.18)$$

converts the partial differential equation (2.1) to an ordinary differential equation:

$$\zeta g''' + g'' + \frac{1}{2}gg'' = 0. \quad (2.19)$$

Here, the primes refer to differentiation with respect to ζ , and the non-dimensional streamfunction is now given by

$$\psi = \nu x g(\zeta). \quad (2.20)$$

The boundary conditions are

$$g' \rightarrow 2 \quad \text{as} \quad \zeta \rightarrow \infty \quad \text{and} \quad g = g' = 0 \quad \text{at} \quad \zeta = \frac{Ur_0^2}{4\nu x_d}. \quad (2.21)$$

The location where the latter boundary conditions are applied changes with x . The resulting solution varies with streamwise location, i.e. similarity does not exist in this flow. This is evident from the velocity profiles and its derivatives shown in figures from 2.7 to 2.12. Further the velocity profiles are identical when the quantity x/R is held constant. This is because ζ is the only parameter in equations 2.19 to 2.21 which is constant when x/R is constant.

2.2.4 Momentum thickness

The momentum thickness θ is calculated taking into consideration the area factor. The velocity deficit because of the shear in the boundary layer is $(U_\infty - U_d)$. The momentum deficit can be written as,

$$U_\infty^2 \int_{r_0}^{r_0+\theta} r_d dr_d = \int_{r_0}^{\infty} U_d(1 - U_d)r_d dr_d \quad (2.22)$$

On integrating and simplifying equation 2.22 becomes;

$$\theta^2 + 2r_0\theta - 2I = 0, \quad (2.23)$$

which is a quadratic equation in θ , and I is given by

$$I \equiv \int_{r_0}^{\infty} U(1 - U)r_d dr_d. \quad (2.24)$$

The physically feasible solution is

$$\theta = -r_0 + \sqrt{r_0^2 + 2I}. \quad (2.25)$$

Similarly the displacement thickness may also be calculated, using

$$\delta^* = -r_0 + \sqrt{r_0^2 + 2I_1} \quad (2.26)$$

where

$$I_1 \equiv \int_{r_0}^{\infty} (1 - U)r_d dr_d. \quad (2.27)$$

The momentum thickness and displacement thickness are scaled with the corresponding Reynolds number and are given in the figures 2.14 and 2.15. For comparison the result from the Blasius solution is also plotted. It is evident from the figure that the Navier-Stokes solutions approach Blasius as the Reynolds number increases, as curvature for a given x is smaller. The shape factor, H , which is the ratio of displacement thickness to momentum thickness, is plotted in figure 2.16 against axial location for various Reynolds numbers. H increases with Reynolds number. The corresponding factor for a Blasius solution is 2.59, which is shown by the dotted lines in the figure. It may be guessed from lower value of H in the axisymmetric case that this flow will be stabler than the two-dimensional.

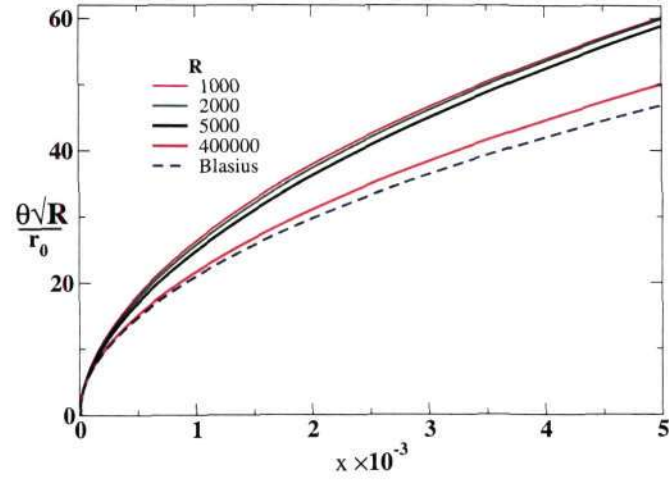


Figure 2.14: Variation of momentum thickness along streamwise coordinate, for different Reynolds numbers.

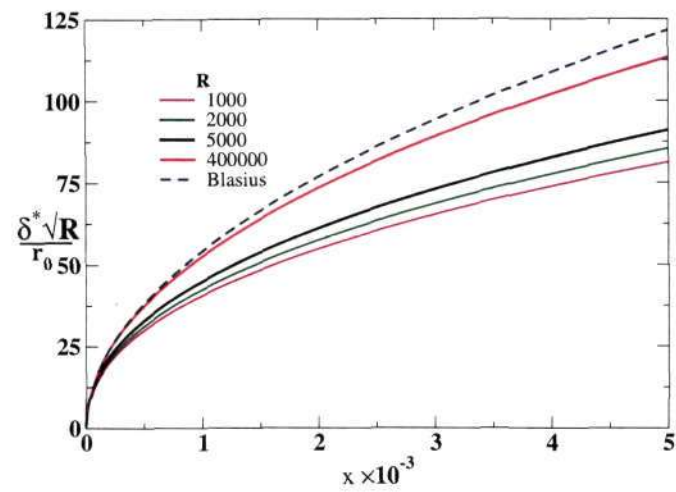


Figure 2.15: Variation of displacement thickness along streamwise coordinate, for different Reynolds numbers.

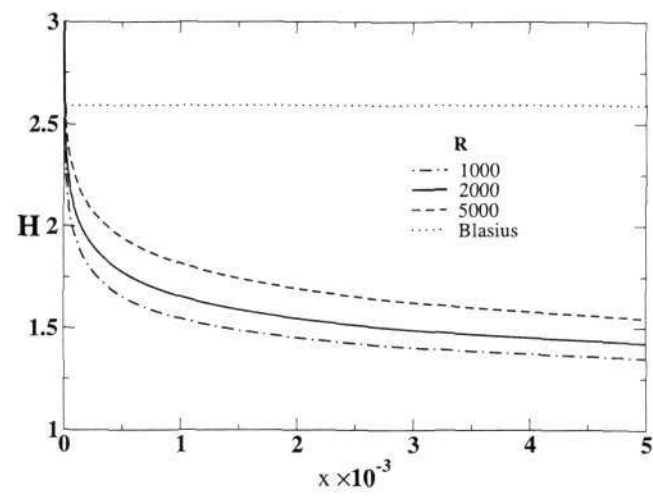


Figure 2.16: Variation of shape factor along streamwise coordinate, for different Reynolds numbers. The Blasius value (dotted line) is shown for comparison.

CHAPTER 3

LINEAR STABILITY ANALYSIS

3.1 Formulation of the stability problem

We conduct a stability analysis of the laminar axisymmetric boundary layer to estimate the conditions under which linear disturbances of particular frequencies begin to grow, and also to obtain the nature and rate of growth of these disturbances. Based on present wisdom, and our own experience in two-dimensional flows, we make the assumption that non-parallel effects are small.

3.1.1 Linear stability equations

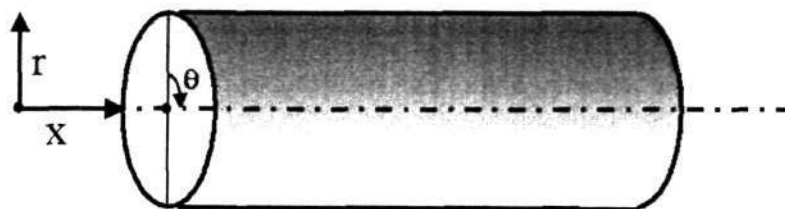


Figure 3.1: Schematic diagram showing the coordinate system

Figure 3.1 shows the coordinate system used for the present study. We begin with Navier-Stokes equations in cylindrical-polar coordinates. The velocity is normalised by the free stream velocity, U_∞ . The stability calculations are carried

out with two types of mean velocity profiles, which were described in the previous chapter. The first one is a Blasius profile and the second one is the solution of the Navier-Stokes equations with boundary layer approximations. For the first case the length scale used is the momentum thickness, θ , whereas in the latter case the body radius, r_0 , is taken as the length scale. The corresponding Reynolds numbers are R_θ and R respectively. In this thesis, these are called the local Reynolds number and the inflow Reynolds number respectively.

Flow quantities are decomposed into their mean and fluctuating part, as

$$\vec{v}_{tot} = U(r)\vec{x} + \vec{v}(x, r, \theta, t) \quad (3.1a)$$

$$p_{tot} = P(x) + p(x, r, \theta, t) \quad (3.1b)$$

$$\text{where } \vec{v} = u\vec{x} + v\vec{r} + w\vec{\theta}. \quad (3.1c)$$

u, v and w are the disturbance velocities in the axial, radial and azimuthal directions respectively. Here the basic flow is assumed to be parallel, with a non-zero component in the axial direction alone. The stability equations are obtained using the standard procedure. The equation for the mean flow is subtracted from the equations for the total velocity field. The resulting equations are then linearised, neglecting the product of two disturbance quantities. The resulting equations are

$$\frac{\partial u}{\partial t} + U \frac{\partial u}{\partial x} + v \frac{\partial U}{\partial r} = \frac{1}{Re} \left(\frac{\partial^2 u}{\partial x^2} + \frac{1}{r} \frac{\partial u}{\partial r} + \frac{1}{r^2} \frac{\partial^2 u}{\partial \theta^2} + \frac{\partial^2 u}{\partial x^2} \right) \quad (3.2a)$$

$$\frac{\partial v}{\partial t} + U \frac{\partial v}{\partial x} = -\frac{\partial p}{\partial r} + \frac{1}{Re} \left(\frac{\partial^2 v}{\partial x^2} + \frac{1}{r} \frac{\partial v}{\partial r} + \frac{1}{r^2} \frac{\partial^2 v}{\partial \theta^2} + \frac{\partial^2 v}{\partial x^2} - \frac{v}{r^2} - \frac{2}{r^2} \frac{\partial w}{\partial \theta} \right) \quad (3.2b)$$

$$\frac{\partial w}{\partial t} + U \frac{\partial w}{\partial x} = -\frac{1}{r} \frac{\partial p}{\partial \theta} - \frac{1}{Re} \left(\frac{\partial^2 w}{\partial x^2} + \frac{1}{r} \frac{\partial w}{\partial r} + \frac{1}{r^2} \frac{\partial^2 w}{\partial \theta^2} + \frac{\partial^2 w}{\partial x^2} - \frac{w}{r^2} + \frac{2}{r^2} \frac{\partial v}{\partial \theta} \right). \quad (3.2c)$$

The disturbance velocities may be represented by the generalized stream-functions ψ and ϕ , and are given by

$$u = \frac{1}{r} \frac{\partial \psi}{\partial r} \quad (3.3a)$$

$$v = -\frac{1}{r} \left(\frac{\partial \psi}{\partial x} + \frac{\partial \phi}{\partial \theta} \right) \quad (3.3b)$$

$$w = \frac{\partial \phi}{\partial r}. \quad (3.3c)$$

The disturbance stream-functions in normal mode form are

$$\psi(x, r, \theta) = \frac{1}{2} \left(\Psi(r) \exp[i(\alpha x + n\theta - \omega t)] + \text{c.c.} \right), \quad (3.4a)$$

and

$$\phi(x, r, \theta) = \frac{1}{2} \left(\Phi(r) \exp[i(\alpha x + n\theta - \omega t)] + \text{c.c.} \right). \quad (3.4b)$$

Here, $\Phi(r)$ and $\Psi(r)$ are the amplitudes of the disturbance stream-functions, α is the wave number in the streamwise direction and n is an integer, which is the number of waves encircling the cylinder. The value of n can be either positive or negative, depending on whether wave propagation is anti-clockwise or clockwise. In the temporal stability analysis carried out here, the frequency ω is a complex quantity. The growth rate of the instability is given by the imaginary part of the frequency (ω_i). The phase speed of the wave is denoted by $c_r = \omega_r/\alpha$.

In equations 3.2 we substitute the disturbance velocities by the disturbance stream-functions given by equation 3.3. Eliminating pressure from these three equations results in two fourth-order ordinary differential equations in Ψ and Φ . These final stability equations are given by

$$\begin{aligned}
& (U - c) (\Psi'' - S\Psi' - \alpha^2\Psi) - \Psi(U'' - SU') - (U - c) \alpha n\Phi - \frac{n}{\alpha} (U''\Phi + U'\Phi' - SU'\Phi) \\
&= \frac{1}{i\alpha R} \left[\Psi^{iv} - 2S\Psi''' + 3S^2\Psi'' - 3S^3\Psi' - 2\alpha^2(\Psi'' - S\Psi') + \alpha^4\Psi \right. \\
&\quad \left. - n^2S^2(\Psi'' - 3S\Psi' - \alpha^2\Psi) - n\alpha[\Phi'' + S\Phi' - (\alpha^2 + n^2S^2)\Phi] \right] \quad (3.5)
\end{aligned}$$

and

$$\begin{aligned}
& (U - c) (\Phi'' + S\Phi' - n^2S^2\Phi) + U'\Phi' - (U - c) n\alpha S^2\Psi = \frac{1}{i\alpha R} \left[\Phi^{iv} + 2S\Phi''' \right. \\
&\quad \left. - S^2\Phi''(1 + 2n^2) - \alpha^2\Phi'' + S^3(1 + 2n^2)\Phi' - \alpha^2S\Phi' - S^4(4n^2 - n^4)\Phi + \alpha^2n^2S^2\Phi \right. \\
&\quad \left. - n\alpha S^2\Psi'' + 3\alpha nS^3\Psi' - (4\alpha nS^4 - \alpha^3nS^2 - \alpha n^3S^4)\Psi \right]. \quad (3.6)
\end{aligned}$$

Here $S = 1/r$. Incidentally Rao (1967) had derived similar equations, but there are several discrepancies. His equations were

$$\begin{aligned}
& (U - c) (\Psi'' - S\Psi' - \alpha^2\Psi) - \Psi(U'' - SU') - (U - c) \alpha n\Phi - \frac{n}{\alpha} (U''\Phi + U'\Phi' - SU'\Phi) \\
&= \frac{1}{i\alpha R} \left[\Psi^{iv} - 2S\Psi''' + 3S^2\Psi'' - 2\alpha^2(\Psi'' - S\Psi') + \alpha^4\Psi \right. \\
&\quad \left. - n^2S^2((\Psi'' - 3S\Psi' - \alpha^2\Psi) - n\alpha[\Phi'' + S\Phi' - (\alpha^2 + n^2S^2)\Phi]) \right] \quad (3.7)
\end{aligned}$$

$$\begin{aligned}
& \text{and } (U - c) (\Phi'' + S\Phi' + n^2S^2\Phi) + U'\Phi' + (U - c) n\alpha S^2\Psi \\
&= \frac{1}{i\alpha R} \left[\Phi^{iv} + 2S\Phi''' - S^2\Phi''(1 - 2n^2) + \alpha^2\Phi'' + S^3(1 + 2n^2)\Phi' - \alpha^2S\Phi' \right. \\
&\quad \left. - S^4(2n^2 - n^4)\Phi - \alpha^2n^2S^2\Phi - n\alpha S^2\Psi'' + 3\alpha nS^3\Psi' - (4\alpha nS^4 - \alpha^3nS^2 - \alpha n^3S^4)\Psi \right]. \quad (3.8)
\end{aligned}$$

There is an additional term $-3S^3\Psi'$ in our equations and some terms are of opposite sign. Our equations have been checked several times, and we are confident about these corrections.

3.1.2 Boundary conditions

At the wall, all disturbance velocity components are zero because of the no slip condition.

$$\Psi = \Psi' = 0, \quad \Phi = \Phi' = 0 \quad \text{at} \quad r = \frac{1}{S_0}. \quad (3.9)$$

Far away from the wall, the disturbance velocities tend to zero, i.e. Ψ and Φ tend towards constant values of K_1 and K_2 respectively. Using equation 3.3b, we get

$$K_2 = -\frac{\alpha}{n}K_1. \quad (3.10)$$

Upon neglecting curvature i.e., putting $S = 0$ and letting $n \rightarrow \infty$ such that nS tends to a finite quantity, namely, the spanwise wavenumber, β , and performing some algebraic manipulations, equations 3.5 and 3.6 reduce to the 3D Orr-Sommerfeld equation and Squire's equation for boundary layers on two-dimensional surfaces, given for example in Schmid & Henningson (2001).

3.1.3 Energy Balance

The disturbance kinetic energy balance throws some light on the radial distribution of disturbance production etc. The energy balance equation is obtained by taking the dot product of the linearised vector stability equations with the disturbance velocity vector,

$$(\vec{v}) \cdot [\mathcal{L}\mathcal{S}(\vec{v})] = 0, \quad (3.11)$$

where $\mathcal{L}\mathcal{S}$ is the linear stability operator. The equation 3.11 after averaging over one cycle in x , θ and time, gives

$$2\omega_i \varepsilon(r) = \nabla \cdot J(r) + W_+(r) - W_-(r). \quad (3.12)$$

The averaged disturbance kinetic energy has been written as

$$\langle \hat{E}(r, x, t) \rangle_x = \varepsilon(r) \cdot \exp(2\omega_i t), \quad (3.13)$$

where $\varepsilon(r)$ is defined as $1/4(|u|^2 + |v|^2 + |w|^2)$. The energy flux $J(r)$ (the quantity being transported across the boundary layer), the energy production $W_+(r)$ and dissipation $W_-(r)$ rates are given respectively by

$$J(r) = \frac{1}{Re} \nabla \frac{v^2}{2} + \vec{v} \cdot \nabla p, \quad (3.14)$$

$$W_+(r) = -\frac{1}{2} (vu^* + v^*u) \frac{dU}{dr}, \quad (3.15)$$

and

$$W_-(r) = -\frac{1}{Re} \left(\alpha^2 (uu^* + vv^* + ww^*) + u'u'^* + v'v'^* + w'w'^* \right. \\ \left. + \frac{1}{r^2} [n^2 uu^* + (1 + n^2)(vv^* + ww^*) + 2in(v^*w - vw^*)] \right). \quad (3.16)$$

Note that the last term of equation 3.16 is real and always positive, since it comes from a sum of whole-square terms. Here the superscript * denotes the complex conjugate.

The total production rate and dissipation rate across the boundary layer are

given by

$$\frac{\Gamma_{\pm}}{2\pi} \equiv \int_1^{\infty} r W_{\pm}(r) dr. \quad (3.17)$$

At neutral stability, the integrated production and dissipation will be equal in magnitude, while Γ_+ would exceed Γ_- for an unstable disturbance.

3.2 Inviscid stability characteristics

Before we make detailed computations of instabilities, it is instructive to study what happens under inviscid conditions. For two-dimensional flow, the inviscid stability is governed by the Rayleigh equation. It was proved by Rayleigh (1880) that a point of inflexion in the velocity profile is a necessary condition for instability in two-dimensional flow. Later Fjortoft (1950) provided a strictly necessary condition. Tollmien (1935) gave heuristic arguments which suggest that the conditions are sufficient for monotone profiles of boundary layer type. A corresponding inviscid criterion for rigidly rotating flows is given in Maslowe (1974). Necessary conditions for inviscid instability of pipe flow are available, e.g. in Shankar & Kumuran (2000).

3.2.1 Governing Equations

Equations 3.5 and 3.6 with the Reynolds number set to ∞ are

$$(U - c)iacu + vU' = -i\alpha p, \quad (3.18a)$$

$$(U - c)ia\alpha v = -p', \quad (3.18b)$$

$$(U - c)i\alpha w = -\frac{1}{r}inp, \quad (3.18c)$$

$$\text{and} \quad i\alpha u + v' + \frac{v}{r} + \frac{1}{r}inw = 0. \quad (3.18d)$$

The streamwise and azimuthal velocities as well as the pressure may be eliminated from these equations. This results in a single equation in the radial velocity as follows

$$(U - c) \left[v'' + \frac{(3n^2 + \alpha^2 r^2) v'}{(\alpha^2 r^2 + n^2) r} - \frac{(\alpha^2 r^2 + n^2 + 2)}{(\alpha^2 r^2 + n^2)} \alpha^2 v + (1 - n^2) \frac{v}{r^2} \right] - \left[U'' - \frac{(\alpha^2 r^2 - n^2)}{r(\alpha^2 r^2 + n^2)} U' \right] v = 0. \quad (3.19)$$

We define a function $\sigma(r)$ to be

$$\sigma = \frac{(\alpha r)^3}{(\alpha^2 r^2 + n^2)}, \quad (3.20)$$

so that

$$\frac{\sigma'}{\sigma} = \left[\frac{3n^2 + \alpha^2 r^2}{r(\alpha^2 r^2 + n^2)} \right]. \quad (3.21)$$

On multiplying equation (3.19) by $\frac{\sigma v^*}{U - c}$ and integrating from 1 to ∞ , we get

$$\begin{aligned} & \int_1^\infty (\sigma v')' v^* dr - \int_1^\infty \sigma \left[\frac{\alpha^2 r^2 + n^2 + 2}{\alpha^2 r^2 + n^2} \right] \alpha^2 |v|^2 dr + \int_1^\infty (1 - n^2) \frac{|v|^2}{r^2} dr \\ & = \int_1^\infty \sigma \left[U'' - \frac{\alpha^2 r^2 - n^2}{r(\alpha^2 r^2 + n^2)} U' \right] \frac{|v|^2}{|U - c|^2} (U - c)^* dr, \end{aligned} \quad (3.22)$$

The first term in equation (3.22) is

$$\int_1^\infty (\sigma v')' v^* dr = \sigma v^* v' \Big|_1^\infty - \int_1^\infty \sigma |v'|^2 dr = - \int_1^\infty \sigma |v'|^2 dr, \quad (3.23)$$

where we have used the boundary conditions that the velocity vanishes at the wall and at ∞ . Since σ is positive [from equation (3.20)], the first and second terms in

equation (3.22) are negative. For any $n \geq 1$ the third term is also zero or negative. For $n = 0$, combining the second and third term in the equation (3.22), we get

$$-\int_1^\infty \sigma \left[\frac{\alpha^2 r^2 + n^2 + 2}{\alpha^2 r^2 + n^2} \right] \alpha^2 |v|^2 dr + \int_1^\infty \sigma (1-n^2) \frac{|v|^2}{r^2} dr = -\int_1^\infty \sigma \frac{|v|^2}{r^2} (1+\alpha^2 r^2) dr. \quad (3.24)$$

This is again a negative quantity. Hence for any n , the left hand side of equation 3.22 is real and negative, and we may write for the real part of equation (3.22),

$$\int_1^\infty \sigma (U - c_r) \left[U'' - \frac{(\alpha^2 r^2 - n^2)}{r(\alpha^2 r^2 + n^2)} U' \right] \frac{|v|^2}{|U - c|^2} dr \leq 0. \quad (3.25)$$

The imaginary part of equation (3.22) is given by

$$c_i \int_1^\infty \sigma \left[U'' - \frac{(\alpha^2 r^2 - n^2)}{r(\alpha^2 r^2 + n^2)} U' \right] \frac{|v|^2}{|U - c|^2} dr = 0, \quad (3.26)$$

where c_i is the imaginary part of the phase speed c . For the flow to be unstable, i.e. for $c_i \geq 0$, we need

$$\int_1^\infty \sigma \left[U'' - \frac{(\alpha^2 r^2 - n^2)}{r(\alpha^2 r^2 + n^2)} U' \right] \frac{|v|^2}{|U - c|^2} dr = 0. \quad (3.27)$$

Defining $I \equiv U'' - [(\alpha^2 r^2 - n^2)/r/(\alpha^2 r^2 + n^2)]U'$, we can immediately see that a necessary condition for instability is that the quantity I has to change sign somewhere in the domain. This expression is identical to that in pipe flow. Letting $r_0 \rightarrow \infty$, we recover the two-dimensional Rayleigh criterion.

Consider now a flow in which I changes sign. Multiplying equation (3.27) with $(c_r - U_s)$ where U_s is the velocity at the point where I changes sign, we get,

$$\int_1^\infty \sigma (c_r - U_s) \left[U'' - \frac{(\alpha^2 r^2 - n^2)}{r(\alpha^2 r^2 + n^2)} U' \right] \frac{|v|^2}{|U - c|^2} dr = 0. \quad (3.28)$$

Now adding equations (3.25) and (3.28), we have

$$\int_1^\infty \sigma(U - U_s) \left[U'' - \frac{(\alpha^2 r^2 - n^2)}{r(\alpha^2 r^2 + n^2)} U' \right] \frac{|v|^2}{|U - c|^2} dr \leq 0. \quad (3.29)$$

Hence, for at least some part of the domain from 1 to ∞ , we must have

$$(U - U_s) \left[U'' - \frac{(\alpha^2 r^2 - n^2)}{r(\alpha^2 r^2 + n^2)} U' \right] \leq 0. \quad (3.30)$$

This is a stricter condition for instability for axisymmetric flows. The two-dimensional analog is called Fjórtoft's theorem.

We note that, unlike in two-dimensional flows, the quantity I has a dependence on streamwise and azimuthal wavenumbers, but in order to check for instability, it is sufficient to evaluate the limiting cases of I . These are $I_1 = U'' - U'/r$ and $I_2 = U'' + U'/r$ respectively for $\alpha \rightarrow 0$ and $n^2/r^2 \rightarrow 0$. From equations 2.18 and 2.19, I_1 and I_2 can be written as

$$I_1 = U'' - \frac{U'}{r} = \frac{1}{2Rx_d/r_0} \zeta g''', \quad (3.31)$$

$$\text{and } I_2 = U'' + \frac{U'}{r} = \frac{1}{2Rx_d/r_0} (\zeta g''' + g'') \equiv -\frac{1}{4Rx_d/r_0} g g''. \quad (3.32)$$

The quantity I_2 is zero at the wall and at the freestream, since g is zero at the wall and g'' is zero at the freestream. Inside the boundary layer, I_2 is always negative since both g and g'' are positive. I_2 is zero at the wall since g is zero. I_1 is always negative i.e. I never changes sign. Hence the axisymmetric boundary layer is inviscidly stable. In figure 3.2 these quantities are plotted for a sample case.

In two-dimensional boundary-layers, the inflexion point criterion has provided a general guideline for the instability of viscous flows as well. For example, a flow

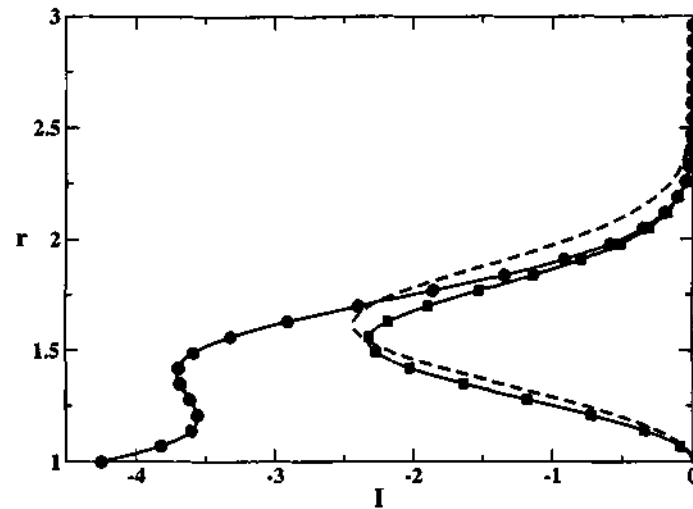


Figure 3.2: Inviscid stability characteristics. I_1 is shown by circles and I_2 by squares. The Reynolds number and curvature are 5000 and 0.8 respectively. The U'' of the Blasius profile is shown by the dotted line. The normal coordinate is scaled with body radius r_0 .

with an inflexion point usually goes unstable at a lower Reynolds number than one without. A future direction of investigation on converging axisymmetric bodies could tell us whether and when the inviscid mode becomes dominant.

3.3 The eigenvalue problem and its numerical solution

Equations 3.5 and 3.6 together with the boundary conditions form an eigenvalue problem, with a dispersion relation

$$\mathcal{F}(\alpha, R, n, S, \omega) = 0. \quad (3.33)$$

In our approach to the axisymmetric boundary layer problem, the curvature (S_0) and the number of waves (n) around the body are specified. Hence a complex eigenvalue ω exists for every combination of R and α .

Equations 3.5 and 3.6 can be discretised and written as matrix equations of the form:

$$\begin{bmatrix} A_{11} & A_{12} \\ A_{21} & A_{22} \end{bmatrix} \begin{bmatrix} \Psi \\ \Phi \end{bmatrix} = \omega \begin{bmatrix} B_{11} & B_{12} \\ B_{21} & B_{22} \end{bmatrix} \begin{bmatrix} \Psi \\ \Phi \end{bmatrix}. \quad (3.34)$$

If the computational domain is covered by a grid of size N , A_{ij} and B_{ij} would be N^{th} order square matrices. The numerical solution of the system (3.34) would thus yield $2N$ eigenvalues. A Chebyshev spectral collocation method is used for the numerical solution (Canuto *et al.*, 1987; Sreenivasan *et al.*, 1994). The collocation points are given by

$$y_{\text{Cheb}}(i) = \cos\left(\frac{\pi i}{N}\right), \quad i = 0, 1, 2, \dots, (N-1), N. \quad (3.35)$$

Here N is an even integer.

3.3.1 Grid stretching

We consider a computational domain extending from $r = 1$ to $r = L$, where $(L-1)$ is at least 5 times the boundary layer thickness, so that the far-field boundary conditions will hold. A grid stretching algorithm given by equation 3.36 is used to (i) transform the computational domain from $(-1, 1)$ to $(1, L)$ and (ii) to distribute the grids such that more points lie in regions of large gradients (close to the wall):

$$y(i) = \frac{(1 + y_{\text{Cheb}}(i))^\gamma}{1 + \frac{2\gamma}{L} - y_{\text{Cheb}}(i)}. \quad (3.36)$$

A smaller value of the clustering factor γ gives rise to a larger number of points close to the wall. A spectral code was developed to compute eigenvalues for equations 3.5 & 3.6. We used 81 and 161 grid points to solve the stability equations, and found that the eigenvalues match up to the sixth decimal place.

3.4 Stability results: thick cylinders

In this section, the analysis deals with thick cylinders where the boundary layer thickness is much less compared to the body radius. The Blasius profile is used as the mean flow. This is a useful exercise since we are thereby isolating the effect of curvature on the disturbance alone. The velocity profiles and its derivatives were given in figure 2.2. The relative surface curvature is defined as the inverse of the body radius and is non-dimensionalised by the momentum thickness, θ :

$$S_0 = \frac{\theta}{r_0}. \quad (3.37)$$

We first validate our code by comparing the eigenspectrum we compute at $S = 0$ and $n = 0$ with the Orr-Sommerfeld solutions of Mack (1976). The comparison is given in figure 3.3. The five most unstable discrete modes are calculated here to an accuracy of 7 decimal places. It is clear that the comparison with Mack's results is excellent. We have compared the results similarly at different Reynolds numbers (not shown). A range of surface curvatures, beginning from almost 2D surfaces (curvature tending to 0) and extending across the regime of 'thick bodies' is considered for the stability analysis. The lowest curvature studied is $S_0 = 0.001$ and the neutral stability curve is plotted in comparison with an Orr-Sommerfeld solution for a zero pressure gradient over a flat plate (figure 3.4). Here the critical

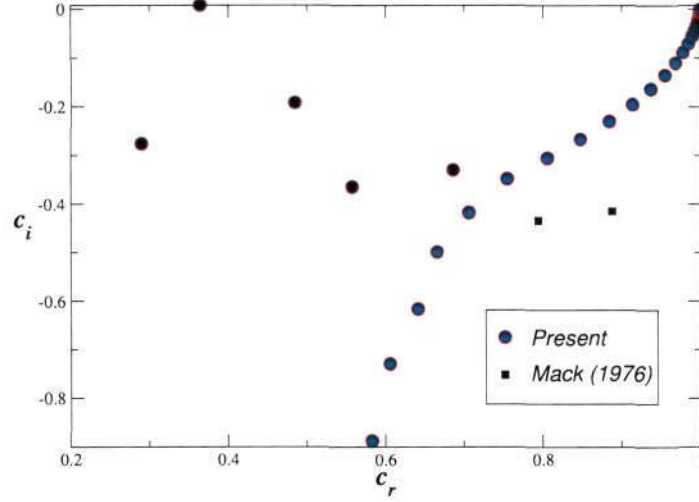


Figure 3.3: Comparison of present eigenspectrum with Mack (1976). $R_\theta = 385.12$ and $\alpha = 0.1189$ when scaled with θ . (In Mack's units, these were $R_{L^*} = 580$ and $\alpha_{L^*} = 0.179$).

Reynolds number (R_{cr}) based on momentum thickness (θ) is found to be 200.3, matching perfectly with the standard Orr-Sommerfeld solution. Moreover the differences everywhere on the neutral stability curve are seen to be negligibly small. The code is thus validated for $S = 0$ and $n = 0$. No numerical comparisons are available for thick cylinders for $S \neq 0$.

Figure 3.5 shows the variation of the most dominant eigenvalue with curvature at a constant Reynolds number and axial wavenumber α . The first mode is stabilized with increase in transverse curvature. A representative eigenfunction of the disturbance velocity for the temporally growing mode is plotted in figures 3.6 to 3.8. The figures show only the region upto $r = 50$, whereas the actual computational domain extends up to $r = 200$.

Figure 3.9 represents the neutral stability curves in the $\alpha - R$ plane for different surface curvatures. As the curvature increases, there is a gradual shift towards

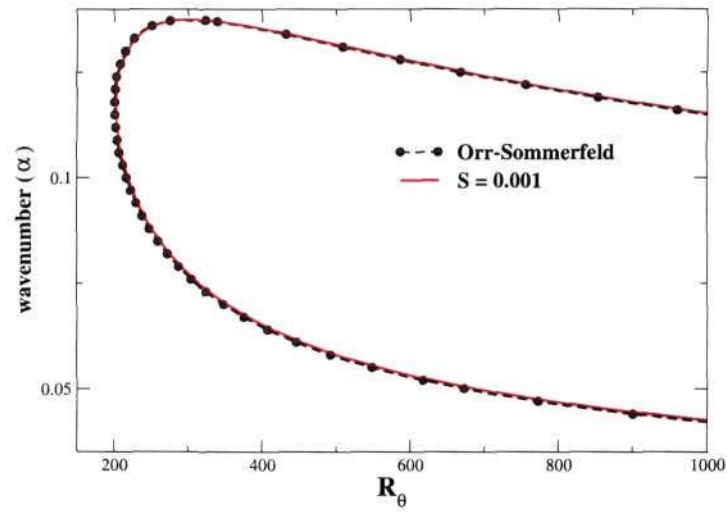


Figure 3.4: Comparison of neutral stability curves at $S = 0.001$ with the Orr-Sommerfeld solution.

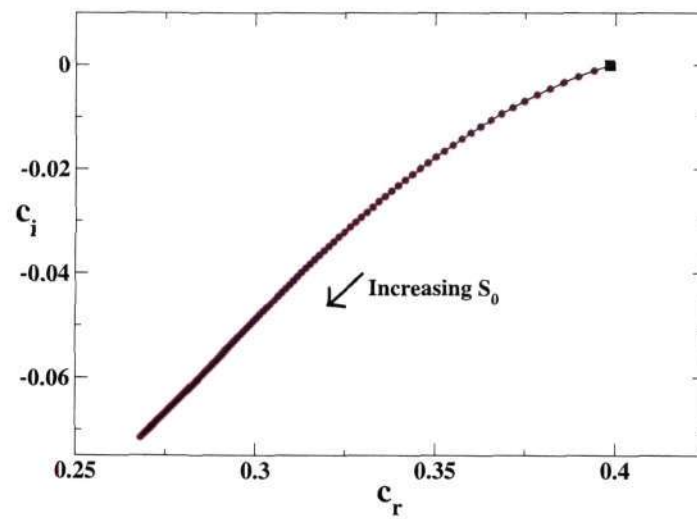


Figure 3.5: Variation of the most dominant eigenvalue with curvature. The Reynolds number and wavenumber are held constant at $R = 200$ and $\alpha = 0.14$. The flat plate eigenvalue is shown by the square. The curvature ranges from $S_0 = 0$ to $S_0 = 0.20$.

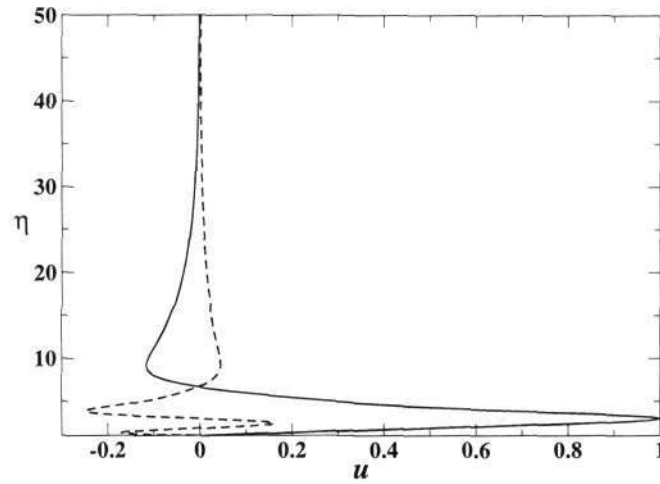


Figure 3.6: Amplitude of disturbance velocity in the streamwise direction, for the non-axisymmetric mode $n = 1$. The Reynolds number is 300, $\alpha = 0.10$ and $S_0 = 0.05$. The solid and dashed lines are the real and imaginary parts respectively.

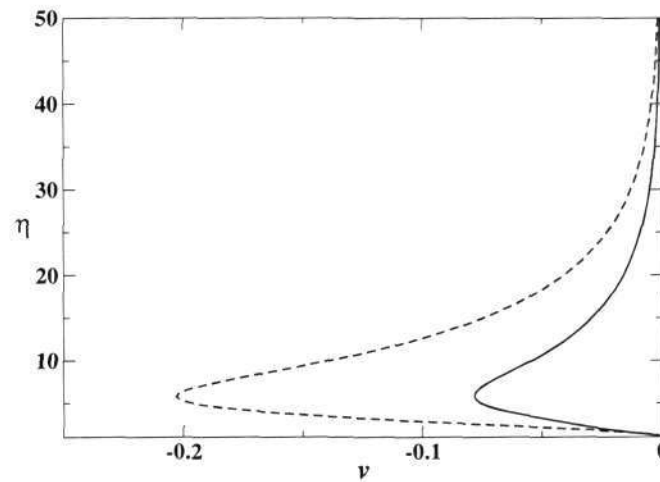


Figure 3.7: Amplitude of disturbance velocity in the radial direction, for the case shown in figure 3.6.

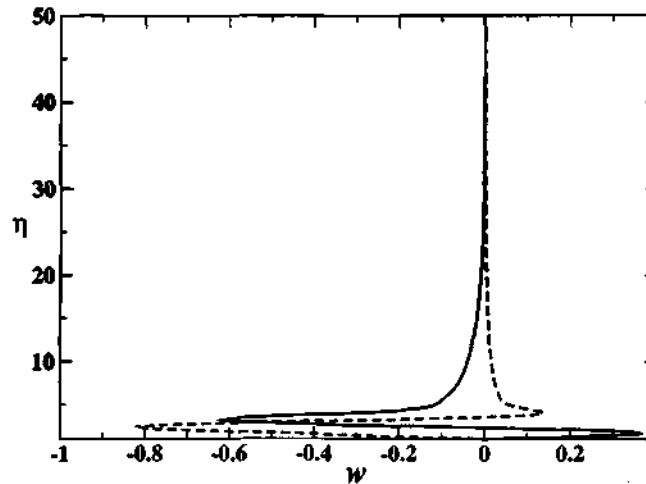


Figure 3.8: Amplitude of disturbance velocity in the azimuthal direction, for the case shown in figure 3.6.

higher streamwise wavenumbers. However, the range of unstable wavenumbers reduces as the curvature increases. The critical Reynolds number increases with curvature, i.e. transverse curvature has a stabilising effect on the two-dimensional mode in the boundary layer over a thick cylinder. The neutral stability curves in the $\omega - R$ plane are plotted in figure 3.10. The range of unstable frequencies again become narrower as the curvature increases. We define the critical wavenumber as the wavenumber of the neutral mode at the critical Reynolds number. This is found to decrease as the surface curvature increases. The critical frequency (similarly defined) also decreases in the same fashion.

The neutral stability loops ($\alpha - R$ plane) for the non-axisymmetric mode ($n = 1$) are shown in figure 3.12. As the curvature increases, the critical Reynolds numbers increases to a maximum and then decreases. The range of wavenumbers for which the flow is unstable also varies with curvature. The critical wavenumber is found to decrease with curvature. The lower branch of the neutral curves becomes steeper

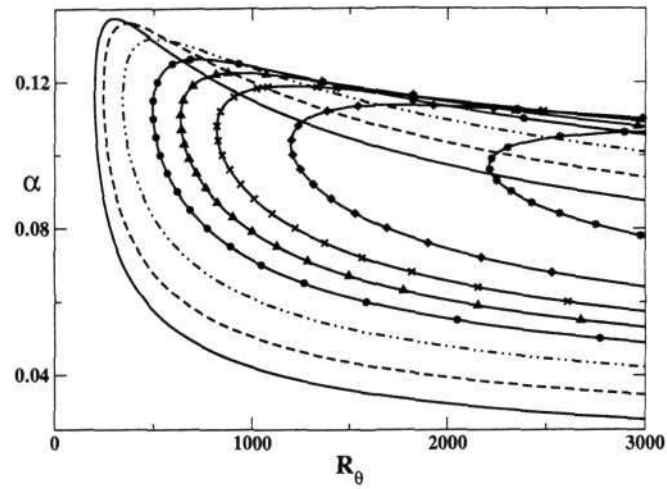


Figure 3.9: Neutral stability curves ($\alpha - R$ plane) for the axisymmetric mode ($n = 0$) for different surface curvatures. The outer-most curve is for $S_0 = 0$ and the inner-most curve is for $S_0 = 0.2$. The other curves are for $S_0 = 0.02, 0.05, 0.08, 0.10, 0.12,$ and 0.15 respectively.

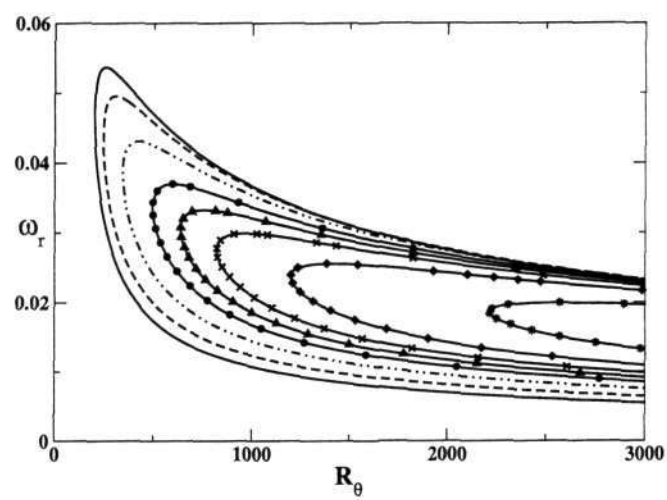


Figure 3.10: The neutral stability curves in the $\omega - R$ plane of figure 3.9.

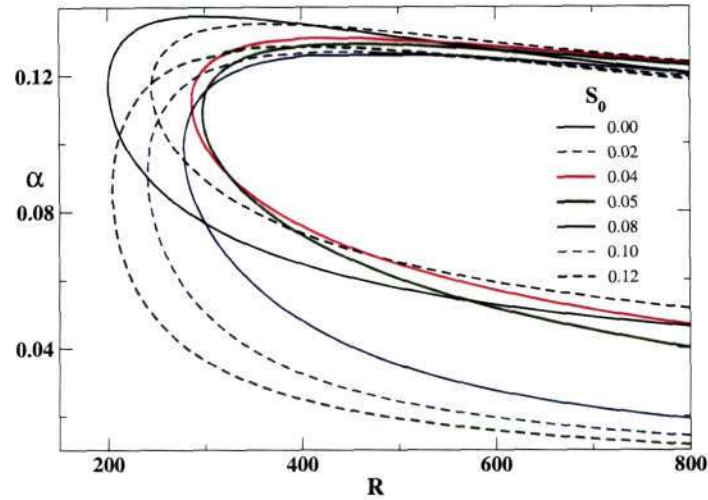


Figure 3.11: Neutral stability curves in the $\alpha - R$ plane for the axisymmetric mode ($n = 1$) for different surface curvatures.

as the curvature increases and upper branch becomes more flat. In figure 3.11 neutral stability curves in the $\omega - R$ plane are plotted. The frequency band for which the flow is unstable varies with curvature. The critical frequency decreases with curvature.

In figure 3.13 the neutral stability curves in the $\alpha - R$ plane are plotted for the second non-axisymmetric mode $n = 2$. As the curvature changes, the range of wavenumbers for which the flow is unstable becomes narrower. At smaller curvatures the critical Reynolds number increases to a maximum and then decreases. However, further increase in curvature again stabilises the flow. When the curvature is 0.10, the critical Reynolds number reaches a minimum. The value of critical wavenumber is found to be decreasing with curvature. Figure 3.14 shows neutral loops in the $\omega - R$ plane.

The variation of phase speed c_r and growth rate c_i with curvature are plotted in figures 3.15 and 3.16 for a fixed Reynolds number (300) and α (0.10). When the

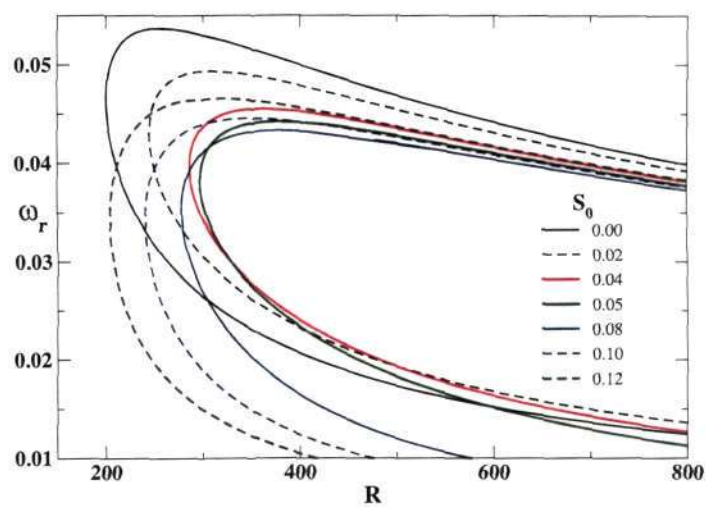


Figure 3.12: Neutral stability curves in the $\omega - R$ plane for the axisymmetric mode ($n = 1$) for different surface curvatures.

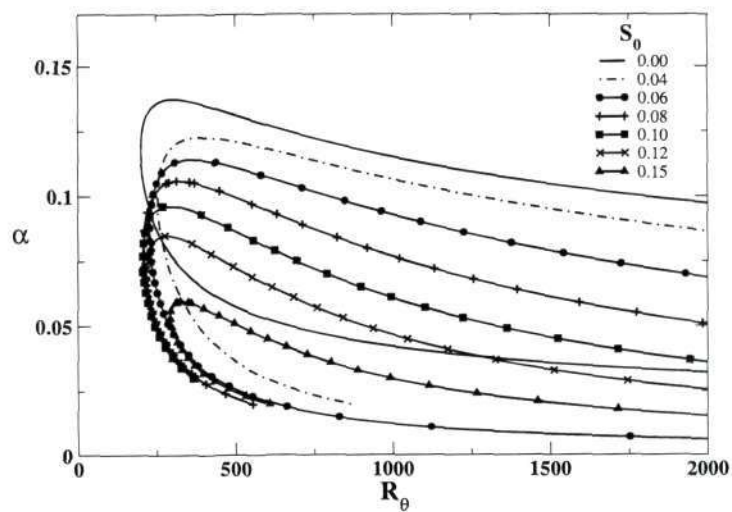


Figure 3.13: Neutral stability curves ($\alpha - R$ plane) for the non-axisymmetric mode ($n = 2$) for different surface curvatures.

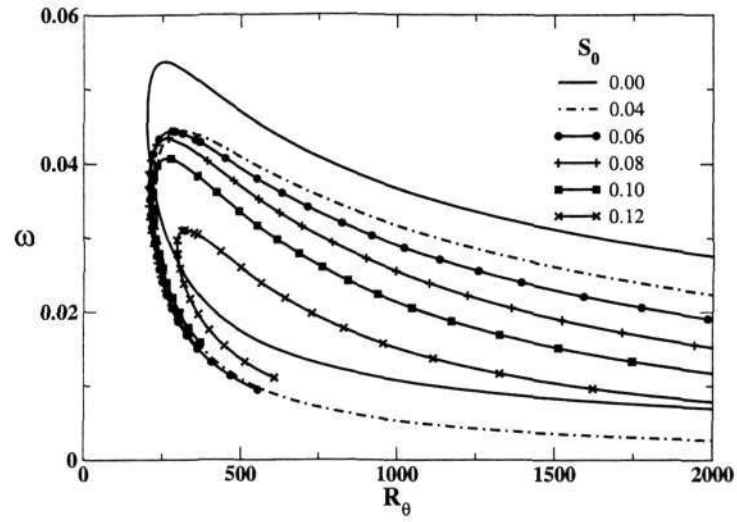


Figure 3.14: Neutral stability curves ($\omega - R$ plane) for the non-axisymmetric mode ($n = 2$) for different surface curvatures.

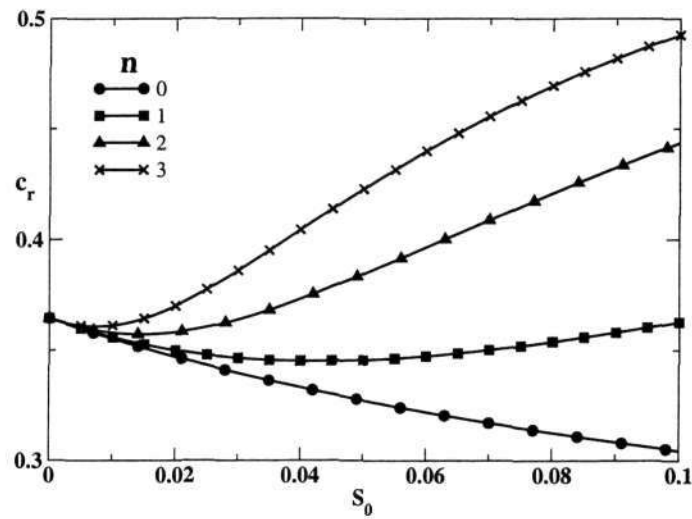


Figure 3.15: Variation of the phase speed (c_r) with curvature for different modes ($n = 0, 1, 2, 3$). The Reynolds number and wavenumber are held constant at $R = 300$ and $\alpha = 0.10$.

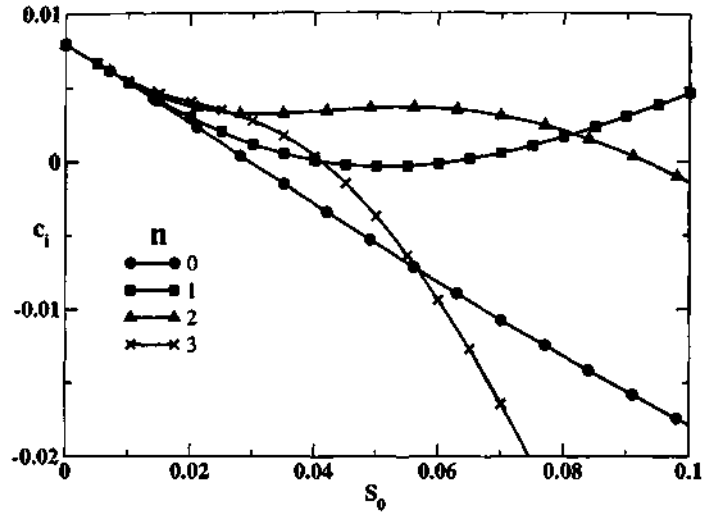


Figure 3.16: Variation of growth rate (c_i) with disturbance wavenumber for the case shown in in figure 3.15.

curvature is small all modes are similar, since $S \sim 0$ and the spanwise wavenumber $\beta = nS \sim 0$. As the curvature increases, the modes begin to behave differently from each other. As the value n increases (obliqueness), c_r also increases, therefore the location of critical layer moves away from the wall.

To summarise the results, we have plotted the critical Reynolds number in figure 3.17 against surface curvature. It is seen that at very small curvatures, the dependence of critical Reynolds number on curvature is almost the same for all modes. At higher curvatures there is a qualitative difference. For the axisymmetric mode, the critical Reynolds number increases monotonically with curvature. When the curvature is zero, the critical Reynolds number is about 200 which is consistent with flat plate results. For the first non-axisymmetric mode ($n = 1$), the critical Reynolds number initially increases with curvature, reaches a maximum and then starts decreasing. The second axisymmetric mode ($n = 2$) initially stabilises as the curvature increases, and critical Reynolds number reaches a local maximum of 256

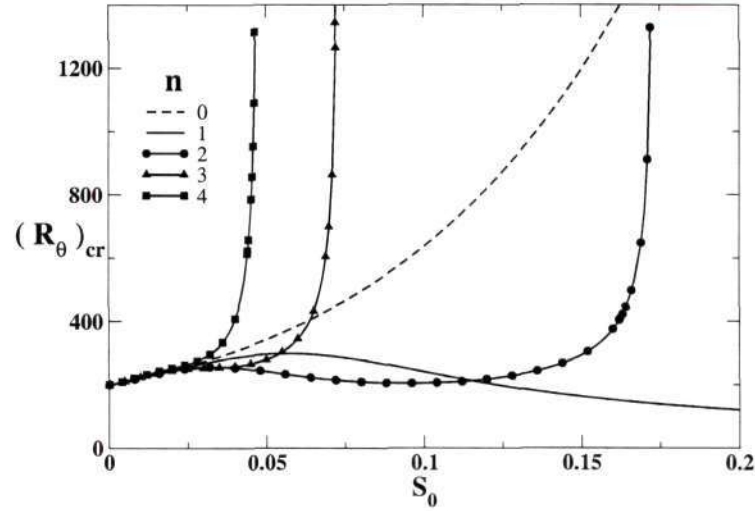


Figure 3.17: Variation of critical Reynolds number (R_{cr}) with surface curvature for different modes.

when curvature is 0.033. After this point, the critical Reynolds number decreases with the curvature. When the curvature is 0.095, the critical Reynolds number reaches a minimum of 205. Beyond this curvature the critical Reynolds number increases constantly with curvature. For the third and fourth modes ($n = 3$ and $n = 4$), the critical Reynolds number increases with curvature. It is found that except for $n = 1$, there exists a critical curvature for all non-axisymmetric modes above which the flow is always stable.

From the above analysis it can be concluded that the modes $n = 0$ and $n \geq 2$ are highly stabilising by curvature. Beyond a certain curvature, no instability is found due to these modes. However, the mode $n = 1$ behaves differently.

The stability analysis so far discussed are based on Blasius profile, therefore the effect of curvature solely on the disturbance quantities. However, mean flow also changes with curvature. As a result, the validity of the stability results obtained using Blasius profile as the mean flow, is reduced at higher curvatures. In figure

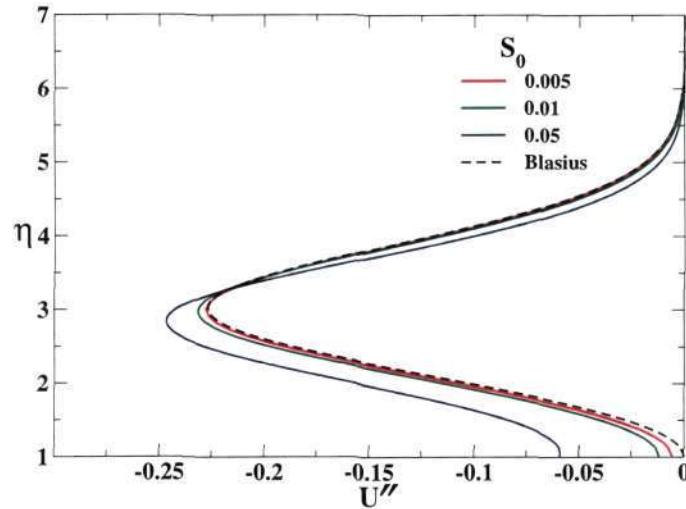


Figure 3.18: Comparison of second derivative (U'') of velocity for Blasius profile and Navier-Stokes solution. In the y -axis Blasius parameter η is shown.

3.4 the second derivative of velocity is plotted for different surface curvatures S_0 . It is evident from the figure that results for the thick cylinders are only valid upto an S_0 of about 0.01.

The variation of the production and dissipation of disturbance kinetic energy across the boundary layer is shown in figure 3.19 to 3.21. The curvature S_0 and Reynolds number R_θ are 0.025 and 260 respectively. The wavenumber is chosen to be close to the neutral for each mode. i.e. $\alpha = 0.116, 0.111$ and 0.117 for $n = 0, 1, 2$ modes respectively. The production is maximum near the location of the critical layer, where $U = c$, whereas the dissipation shows maximum near the wall.

It is to be noted that the production layer of the three modes studied here ($n = 0, 1$ and 2) are overlapping. We may guess that this can result in interaction among these modes which can lead to earlier non-linearity and transition.

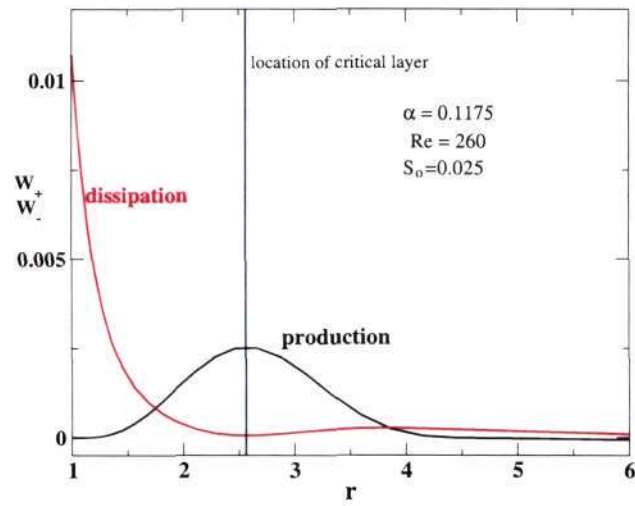


Figure 3.19: Distribution of production (W_+) and dissipation (W_-) of an axisymmetric mode.

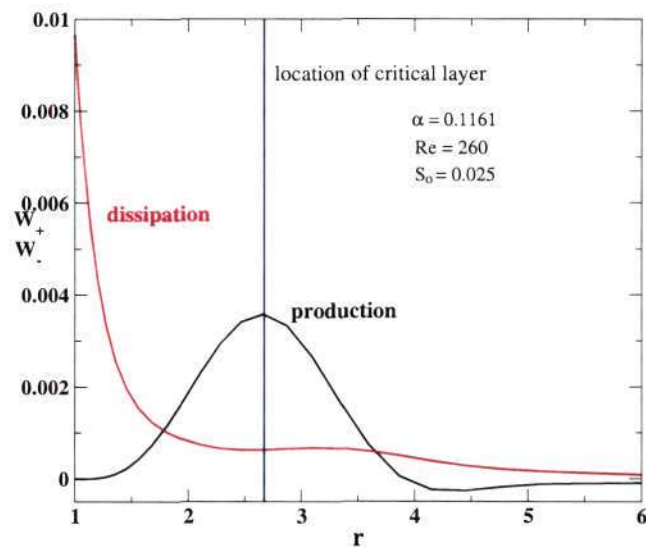


Figure 3.20: Distribution of production (W_+) and dissipation (W_-) of the non-axisymmetric mode $n=1$.

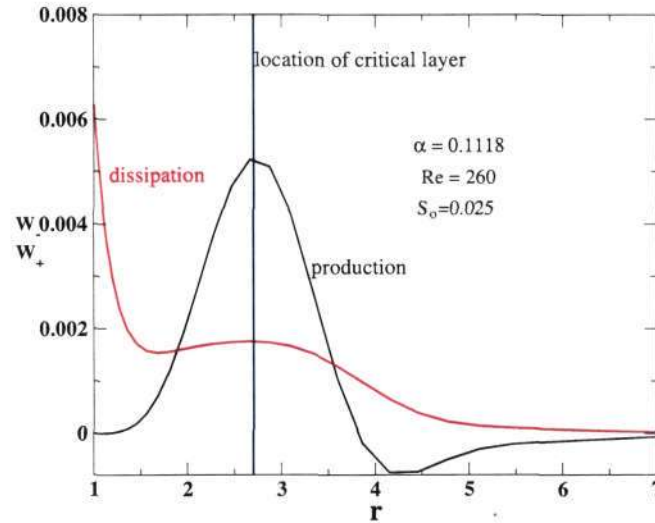


Figure 3.21: Distribution of production (W_+) and dissipation (W_-) of the mode $n=2$.

3.5 Linear stability results: cylinders of arbitrary radius

In this section the stability is analysed using the mean flow velocity profile which is computed from momentum equations under the boundary layer approximation. The Reynolds number is now defined as $R \equiv Ur_0/\nu$, where r_0 is the body radius, U is the freestream velocity and ν is the kinematic viscosity. The velocity profiles for different Reynolds numbers are given in figures 2.7 to 2.12. The base flow varies slowly with streamwise location, but an assumption of locally parallel flow is employed and we seek temporal solutions of the stability equations (3.5 and 3.6). The boundary conditions and the solution approach are the same as of section 3.3 and 3.1.2.

Table 3.1 shows a comparison of critical values with Tutty *et al.* (2002) and

n	Tutty <i>et al.</i> (2002)				Present			
	x_c	R_c	α_c	c_r	x_c	R_c	α_c	c_r
0	47.0	12439	2.730	0.317	47	12463	2.730	0.318
1	543.0	1060	0.125	0.552	581	1013	0.115	0.552
2	91.1	6070	0.775	0.442	91.0	6093	0.775	0.421
3	43.4	10102	1.600	0.403	43.0	10110	1.580	0.410
4	26.8	13735	2.540	0.398	27.0	13742	2.520	0.401

Table 3.1: Critical Reynolds number and other parameters for different modes, in comparison with Tutty *et al.* (2002). The streamwise location where instability first occurs is denoted as x_c . α_c and c_r are the streamwise wavenumber and phase speed corresponding to the critical Reynolds number.

they are in reasonable agreement. The first non-axisymmetric mode ($n = 1$) is destabilised first with a Reynolds number of 1013, at a streamwise location $x = 581$. The corresponding values of the streamwise wavenumber and wave speed are 0.115 and 0.552 respectively. The axisymmetric mode is found to be unstable above a Reynolds number of 12463. The computed growth rate for this mode is shown in figure 3.22. The maximum growth is obtained when α is 3.5. The surface curvature $S_0 = \theta/r_0$ is shown in the upper x -axis. All disturbances decay at larger curvatures. In particular, small wavelength disturbances decay very fast. The growth rate (ω_i) of disturbance waves for $n = 1$ is plotted in figure 3.23 for various streamwise wavenumbers. The Reynolds number is 1000, where no instability is found. It is to be noted that the curvature increases along the streamwise distance. The slowest decay is obtained when $\alpha = 0.10$. In figure 3.24 the growth rate is plotted at a Reynolds number of 2000. The maximum growth is obtained at a streamwise wavenumber $\alpha = 0.20$. All disturbances are found to be decaying out at higher curvatures.

Now we look into the stability characteristics of the second non-axisymmetric mode ($n = 2$). From table 3.1 it is seen that the flow is unstable only if the Reynolds

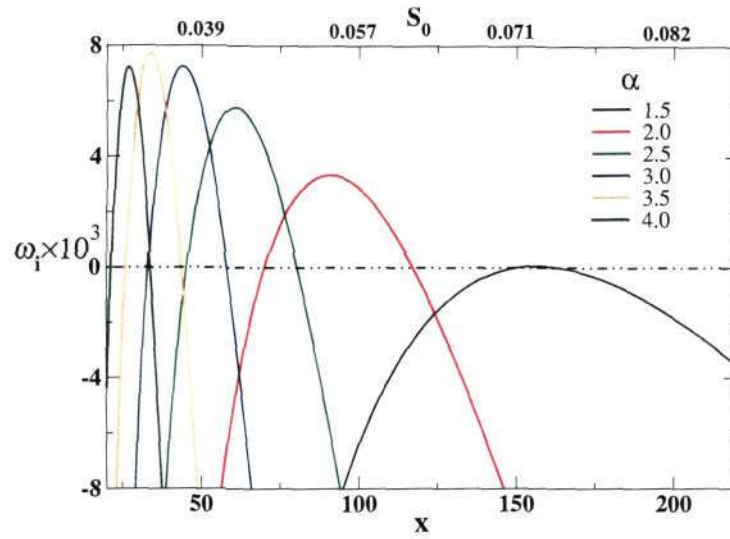


Figure 3.22: Growth rates of disturbance waves along the cylinder axis for the axisymmetric mode at $R = 15,000$.

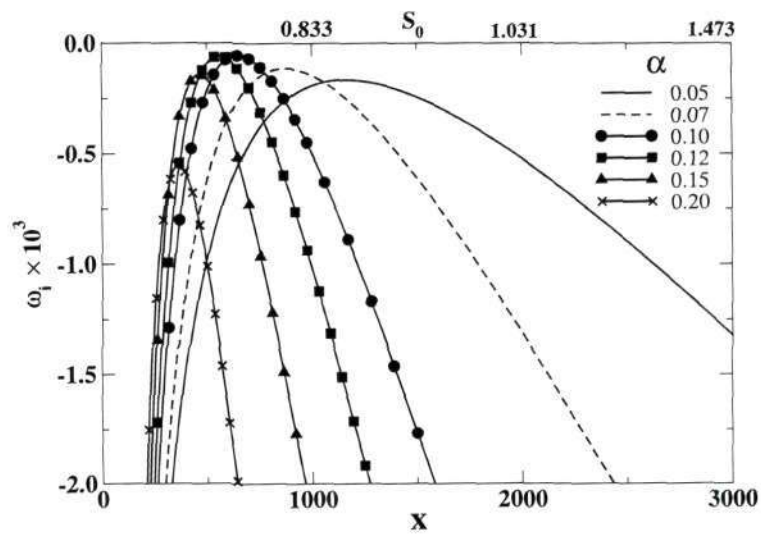


Figure 3.23: Decay rates of disturbance waves along the cylinder axis for the non-axisymmetric mode $n = 1$ at $R = 1000$.

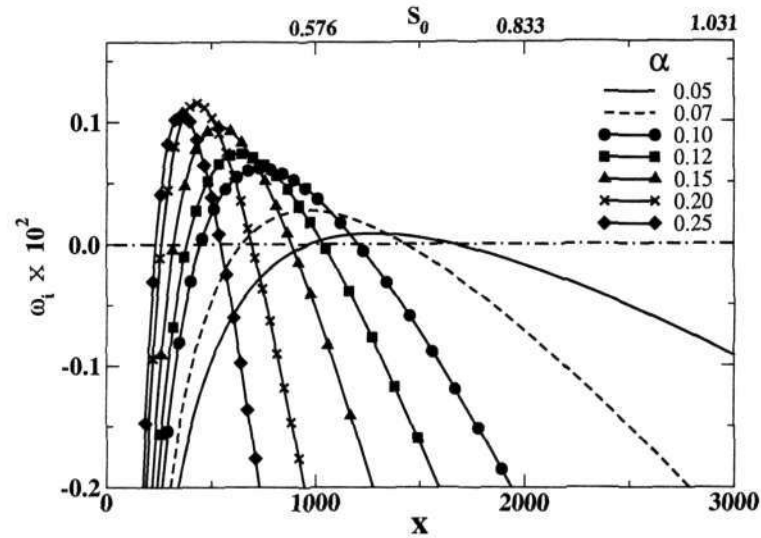


Figure 3.24: Growth rate of disturbance waves along streamwise coordinate for the non-axisymmetric mode $n = 1$ at $R = 2000$.

number is higher than 6093. At $R = 5000$, therefore, all disturbances are stable (see figure 3.25). At a Reynolds number of 10000, only waves within a certain range of frequencies become unstable (see figure 3.26). Here too all disturbances decay at higher curvatures.

In figure 3.27 the decay rate of the non-axisymmetric mode $n = 3$ is presented. The first instability occurs at $R = 10110$, hence all the disturbances considered in this case are decaying. At a higher Reynolds number a certain range of frequencies grow for a small range of curvatures.

Neutral stability curves

A consistent picture that seems to emerge from figures 3.22 to 3.27 is that the flow is unstable to a given mode only for a relatively narrow range of wavenumbers and curvature. At high curvature, instability is unlikely to occur. This is in accordance

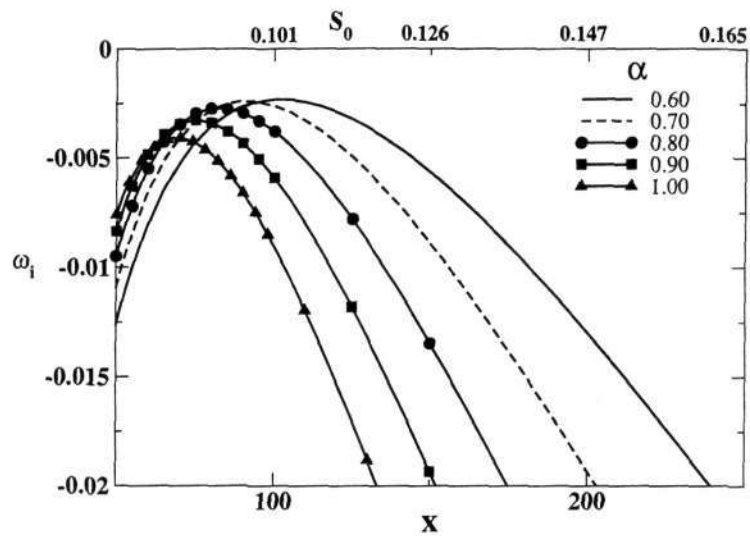


Figure 3.25: Decay rate of disturbance waves along the cylinder surface for the non-axisymmetric mode $n = 2$ at $R = 5000$.

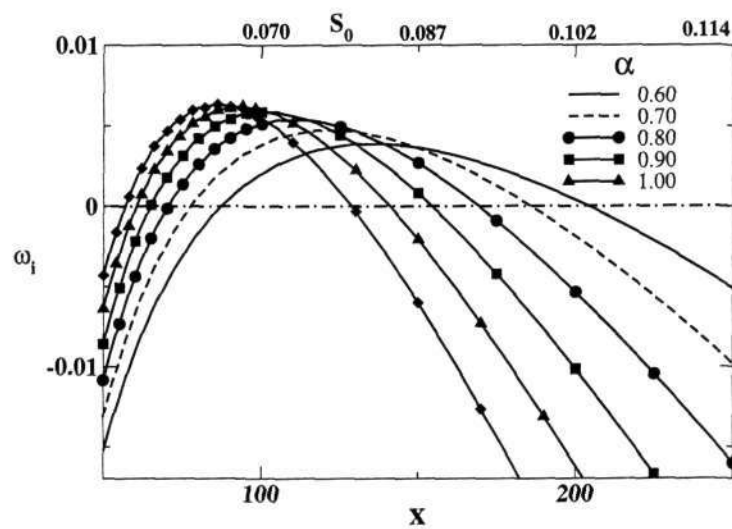


Figure 3.26: Growth rate of disturbance waves along streamwise coordinate for the non-axisymmetric mode $n = 2$ at $R = 10000$.

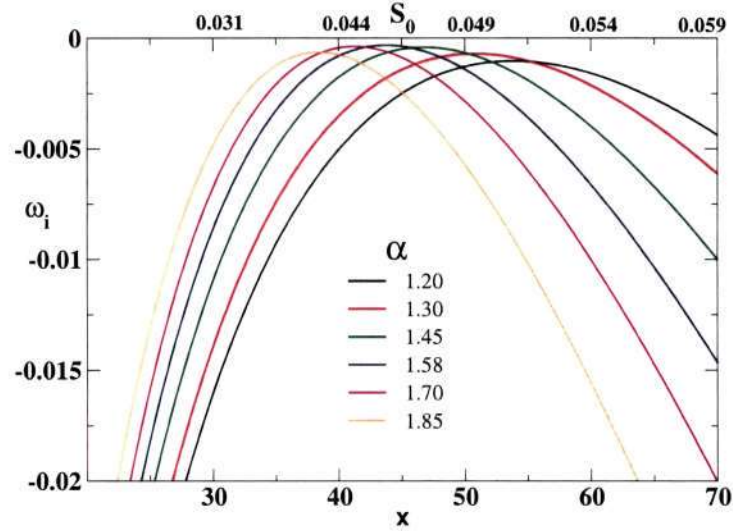


Figure 3.27: Growth rate of disturbance waves along streamwise coordinate for the non-axisymmetric mode $n = 3$ at $R = 10000$.

with our initial guess from the inviscid instability criterion discussed in Section 3.2.

Rather than estimate the effect of curvature from a few sample frequencies, it would be instructive to view the stability boundaries, which is what we do next. It is found that all the neutral boundaries form closed loops. The neutral stability boundaries of the axisymmetric mode is shown in figure 3.28. The Reynolds number ($R = Ur_0/\nu$) determines the first location of instability as well as the closing tail of the neutral loop. In figure 3.29, the neutral stability curves for different R are plotted for $n = 1$. The curvature at which instability first occurs is $S_0 = 0.612$. We have considered a range of R varying from a few hundreds to 100,000. However, in the graph we present only upto Reynolds number = 5,000 for clarity. As the inflow Reynolds number increases, the flow becomes unstable at more upstream locations. Also the loops close at further downstream locations. The range of unstable α also increases with the Reynolds number. In figure 3.30 the neutral curves for the same

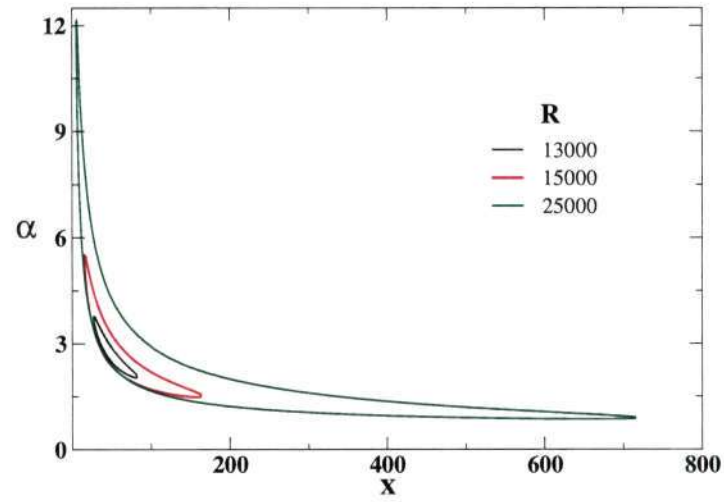


Figure 3.28: Neutral stability loops for axisymmetric mode along the streamwise coordinate at different Reynolds numbers.

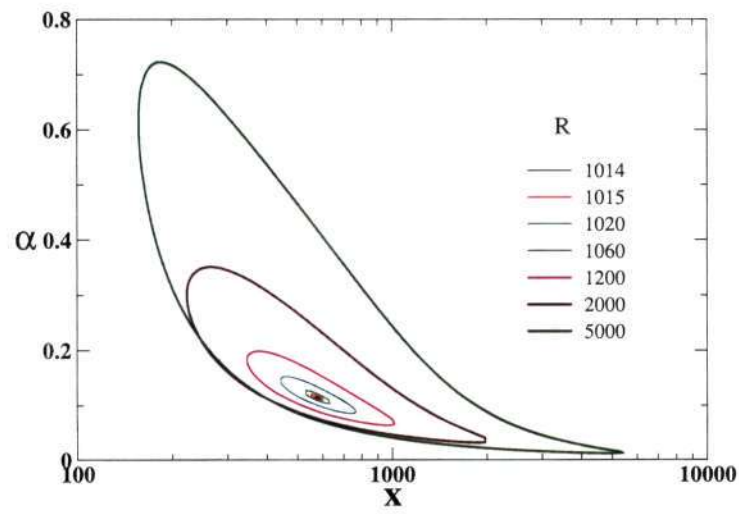


Figure 3.29: Neutral stability loops for non-axisymmetric mode $n = 1$ along the streamwise coordinate at different Reynolds numbers.

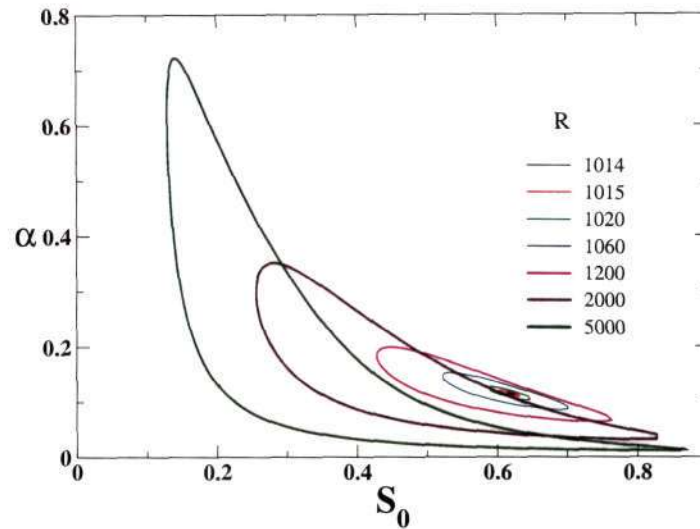


Figure 3.30: Neutral stability loops for non-axisymmetric mode $n = 1$ as a function of surface curvature at different Reynolds numbers.

data as in figure 3.29 are plotted with surface curvature on the abscissa. Note that the surface curvature is a function of streamwise location. It is clear that all linear disturbances are damped at higher curvatures. The closing tail of the neutral loops becomes thinner at higher curvatures and values of α are very small in this region, i.e. only large wavelength disturbances are sustained at higher curvatures.

In figure 3.31 the neutral stability loops for the $n = 2$ mode is plotted along the axial location. At very high Reynolds numbers, the neutral stability loop becomes thinner and extends upto far downstream locations. The neutral curves for the non-axisymmetric mode $n = 3$ are presented in figure 3.32. The axial location is much upstream of the location of the first instability in the $n = 1$ case ($x = 581$). In figure 3.33 the neutral curves are plotted against the curvature. The flow is unstable only for very small curvatures. Next we analysed the stability characteristics of the non-axisymmetric mode $n = 4$ (see figure 3.34 and 3.35). Here again the flow

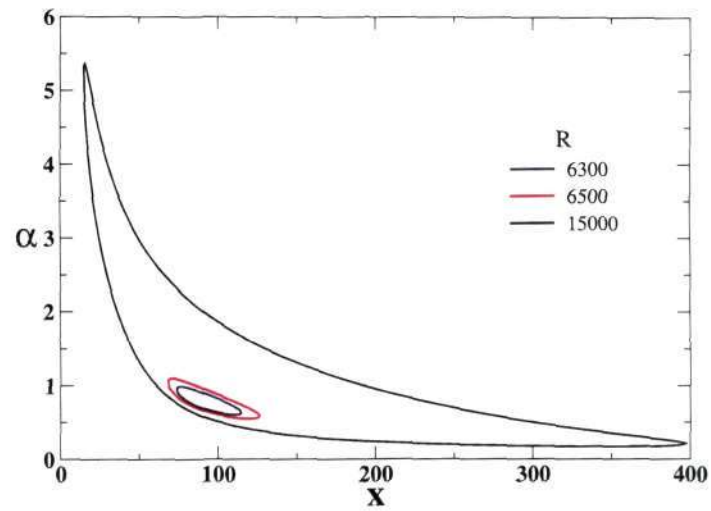


Figure 3.31: Neutral stability loops for non-axisymmetric mode $n = 2$ along the streamwise coordinate at different Reynolds numbers.

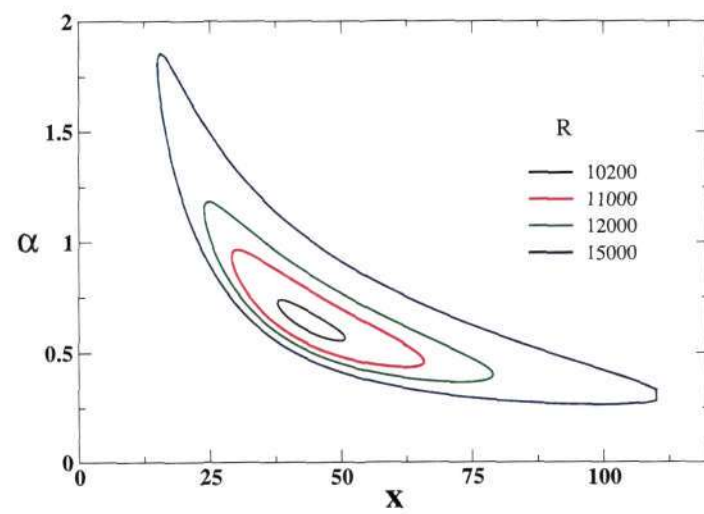


Figure 3.32: Neutral stability loops for non-axisymmetric mode $n = 3$ along the streamwise coordinate at different Reynolds numbers.

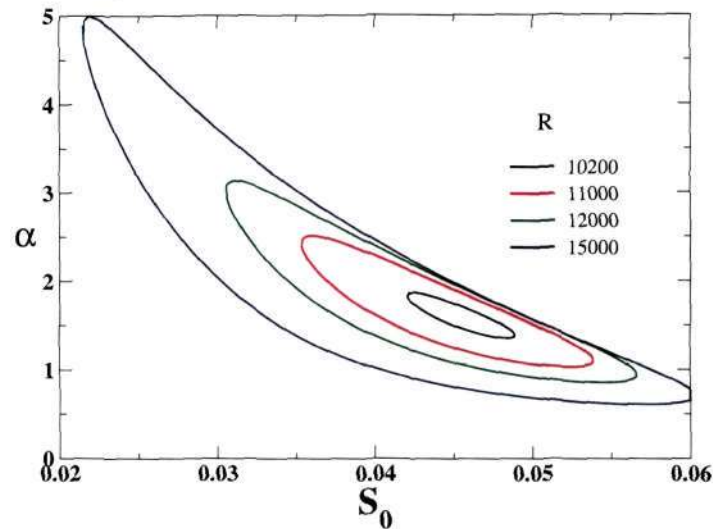


Figure 3.33: Neutral stability loops for non-axisymmetric mode $n = 3$ as a function of surface curvature at different Reynolds numbers.

is unstable only for very small curvatures.

3.5.1 Energy balance

The energy budget of axisymmetric disturbance ($n = 0$) is shown in figure 3.36 and 3.37 at two different streamwise locations. The Reynolds number is 20,000 and $\alpha = 0.125$. The production shows a maximum near the critical layer, where $U \approx c_r$ and the dissipation is maximum near the wall. There is a local minimum of the dissipation near the critical layer, which becomes less pronounced downstream. In figures 3.38 and 3.39 the production and dissipation rates are plotted for the mode $n = 1$. The flow conditions are the same as in the previous case. The behaviour is similar to the axisymmetric mode. The energy balance of mode $n = 2$ is plotted in figures 3.40 and 3.41. The flow conditions are same as the previous cases. The production is maximum near the critical layer. At streamwise location

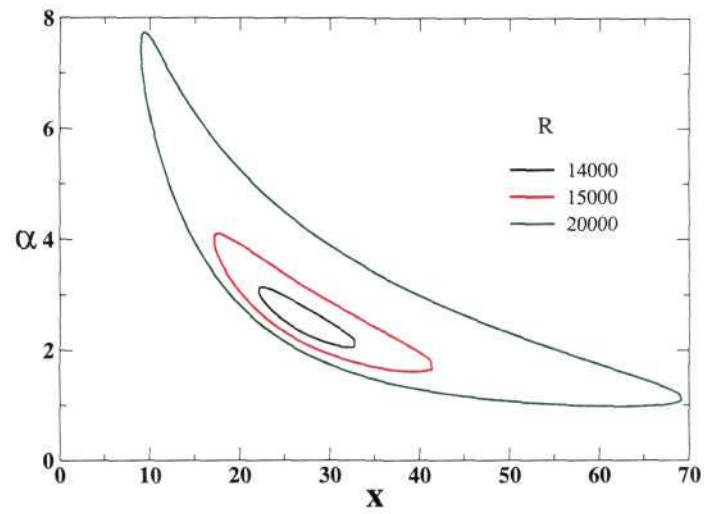


Figure 3.34: Neutral stability loops for non-axisymmetric mode $n = 4$ along the streamwise coordinate at different Reynolds numbers.

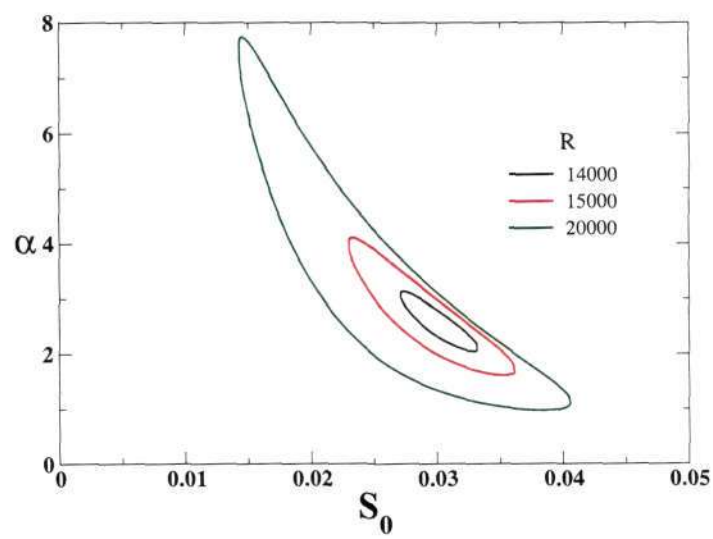


Figure 3.35: Neutral stability loops for non-axisymmetric mode $n = 4$ as a function of surface curvature at different Reynolds numbers.

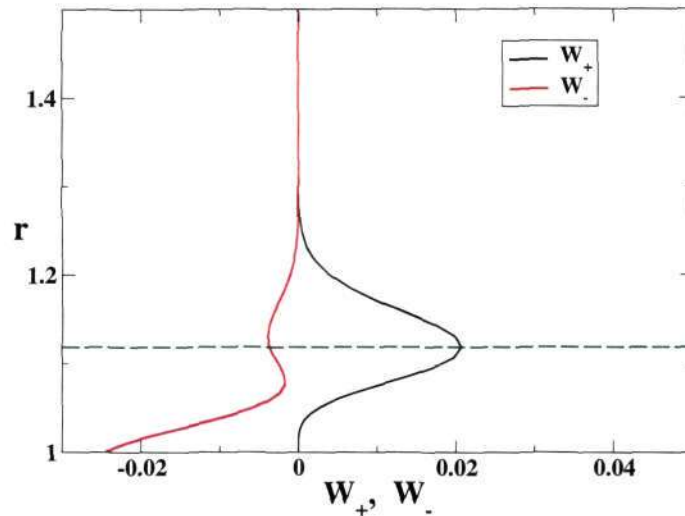


Figure 3.36: Production (W_+) and dissipation (W_-) rate of axisymmetric disturbance at $x = 60$, $R = 20,000$ and $\alpha = 0.125$. The location of the critical line $U = c_r$ is shown by the dashed line.

$x = 60$ the dissipation is maximum near the wall. However at a downstream point, $x = 200$, the maximum dissipation occurs near the critical layer. The behaviour of the mode $n = 3$ is similar to the $n = 2$ mode, as shown in figures 3.42 and 3.43.

Since the production layers overlap, we again hazard a guess that many modes can interact to give earlier non-linearity than in a two-dimensional boundary layer.

3.6 Summary of linear instability studies

The axisymmetric boundary layer is inviscidly stable for any curvature, this result is intuitively expected.

Some qualitative differences between axisymmetric and two-dimensional boundary layers have become apparent. Firstly, any two-dimensional boundary layer which extends to infinity, will become linearly unstable at some point. This how-

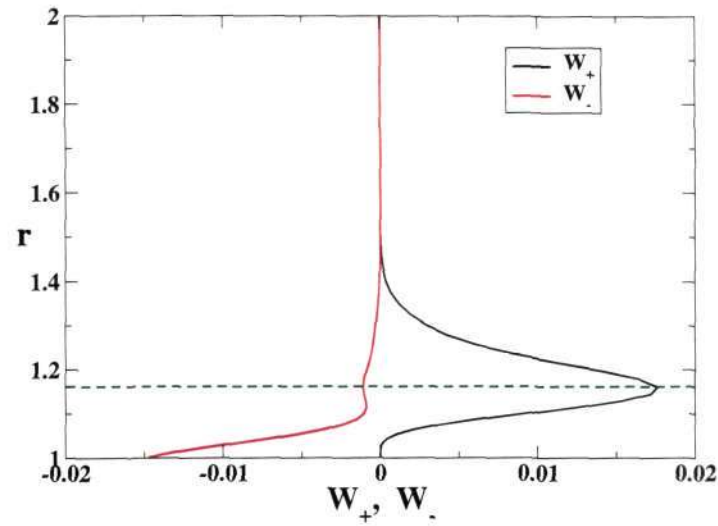


Figure 3.37: Production (W_+) and dissipation (W_-) rate of axisymmetric disturbance at $x = 200$, $R = 20,000$ and $\alpha = 0.125$. The location of the critical line $U = c_r$ is shown by the dashed line.

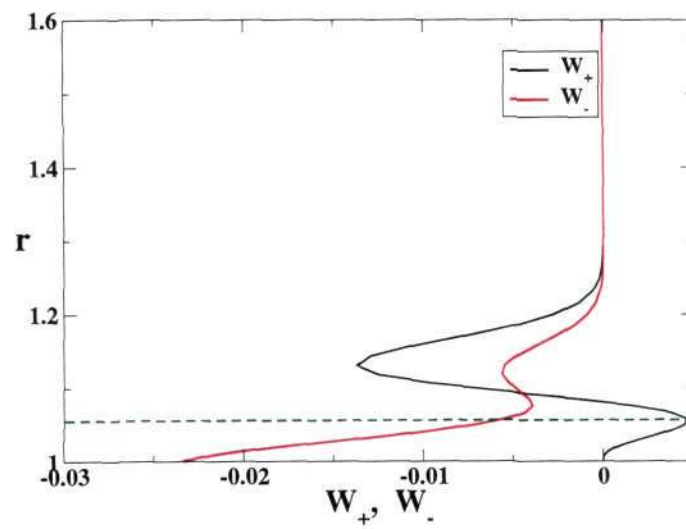


Figure 3.38: Production (W_+) and dissipation (W_-) rate of non-axisymmetric disturbance ($n = 1$) at $x = 60$, $R = 20,000$ and $\alpha = 0.125$. The location of the critical line $U = c_r$ is shown by the dashed line.

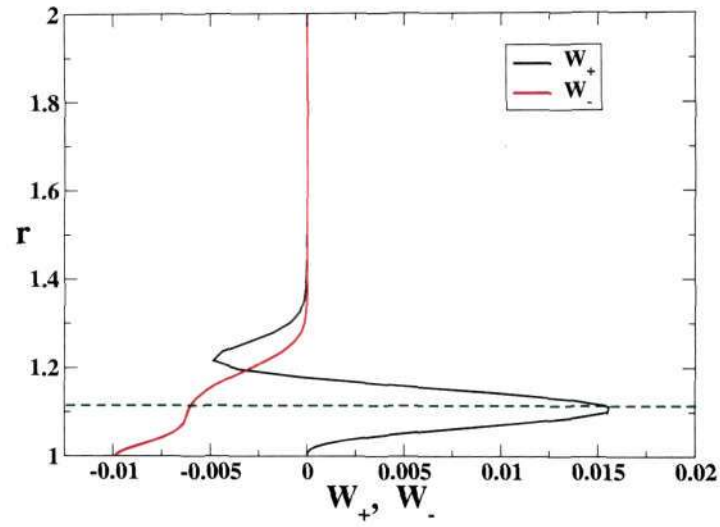


Figure 3.39: Production (W_+) and dissipation (W_-) rate of non-axisymmetric disturbance ($n = 1$) at $x = 200$, $R = 20,000$ and $\alpha = 0.125$. The location of the critical line $U = c_r$ is shown by the dashed line.

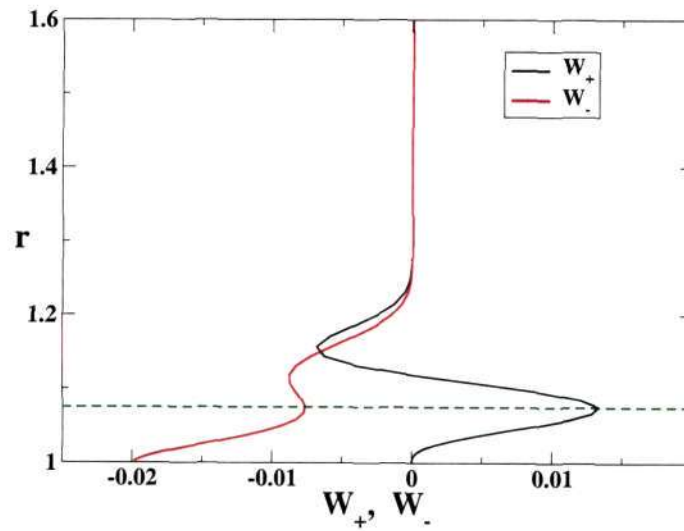


Figure 3.40: Production (W_+) and dissipation (W_-) rate of non-axisymmetric disturbance ($n = 2$) at $x = 60$, $R = 20,000$ and $\alpha = 0.125$. The location of the critical line $U = c_r$ is shown by the dashed line.

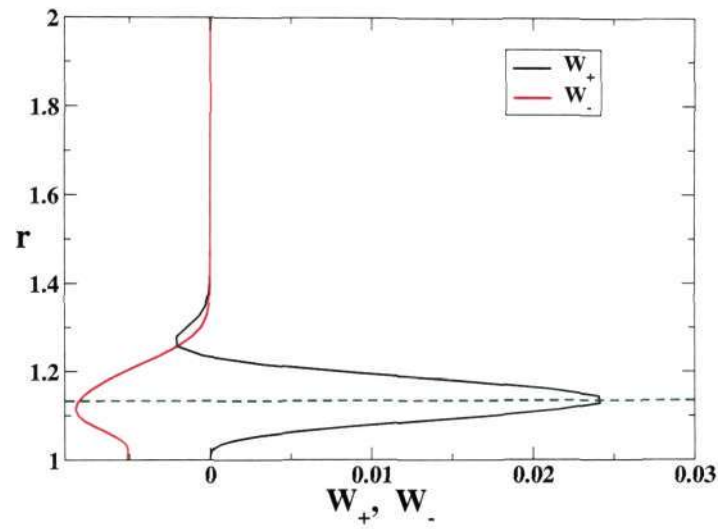


Figure 3.41: Production (W_+) and dissipation (W_-) rate of non-axisymmetric disturbance ($n = 2$) at $x = 200$, $R = 20,000$ and $\alpha = 0.125$. The location of the critical line $U = c_r$ is shown by the dashed line.

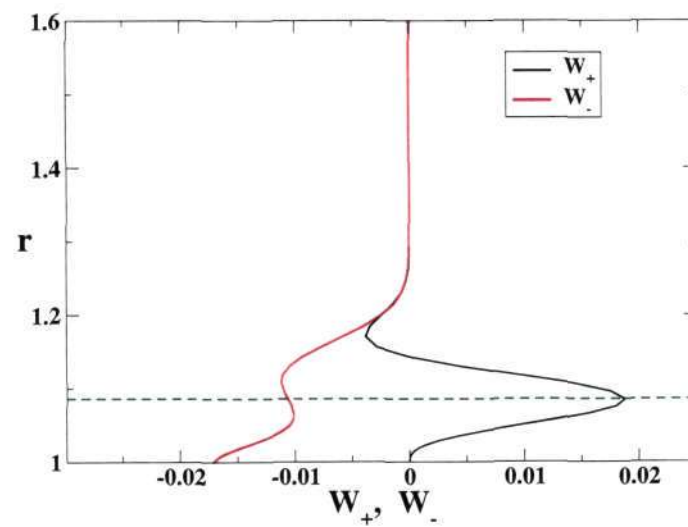


Figure 3.42: Production (W_+) and dissipation (W_-) rate of non-axisymmetric disturbance ($n = 3$) at $x = 60$, $R = 20,000$ and $\alpha = 0.125$. The location of the critical line $U = c_r$ is shown by the dashed line.

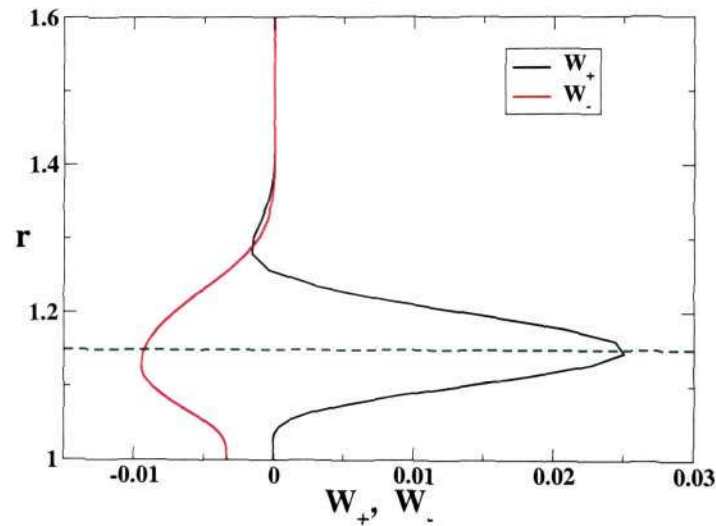


Figure 3.43: Production (W_+) and dissipation (W_-) rate of non-axisymmetric disturbance ($n = 3$) at $x = 200$, $R = 20,000$ and $\alpha = 0.125$. The location of the critical line $U = c_r$ is shown by the dashed line.

ever, is not true for our flow. When the Reynolds number based on the body radius is below about 1000, the flow is always linearly stable. This would apply to long thin wires in low winds. Secondly, even at low curvatures, non-axisymmetric modes become dominant, in contrast to two-dimensional boundary layers, where Squire's theorem holds. At low curvatures, several non-axisymmetric modes are simultaneously unstable, and the production layers of the disturbance kinetic energy have a significant overlap. This could indicate earlier nonlinear interactions than in two-dimensional boundary layers, but further studies are required to confirm this.

An important feature is that all neutral boundaries close at high curvature. Higher non-axisymmetric modes ($n \geq 2$) are linearly unstable only for a very small range of curvatures. Computations have been made for very large values of n , which are not shown, since the trend is the same. It is only the helical ($n = 1$)

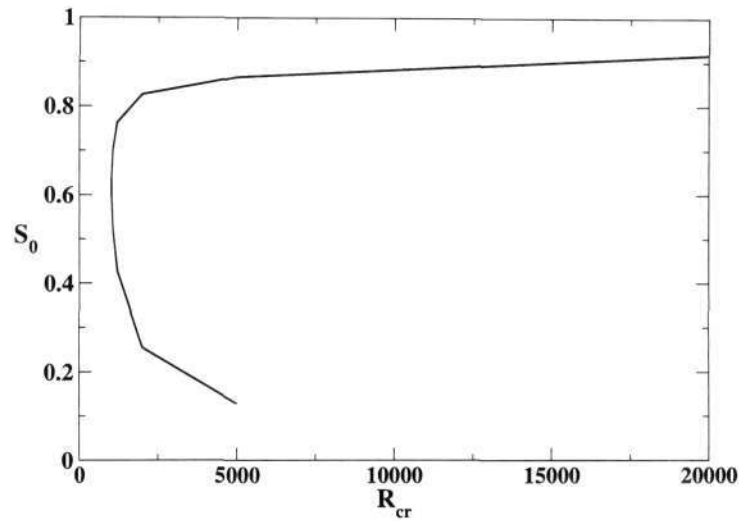


Figure 3.44: Critical Reynolds number as a function of curvature for the mode $n = 1$.

mode which is unstable over a significant axial extent of the cylinder. Even this mode is never unstable for curvatures above 1, as may be seen in figure 3.44. At curvature levels below this, as well as at low Reynolds numbers, the helical mode is expected to decide dynamics. Detailed studies are required to tell whether the above nonlinear interaction can lead to turbulence, and if so, whether the flow will relaminarise at higher curvatures.

Curvature has an overall stabilising effect, both via the mean flow, as well as directly through the stability equations, as studies on the thick cylinder reveal.

CHAPTER 4

SECONDARY INSTABILITY ANALYSIS

The previous chapter was restricted to the linear stability analysis of axisymmetric boundary layers. In this chapter we analyse the secondary instability of axisymmetric as well as two-dimensional zero and adverse pressure gradient boundary layers. A laminar flow in which linear disturbances have grown to a significant amplitude may no longer be considered to be steady. As a thumb rule the non-linearity becomes detectable when the amplitude of the primary disturbance becomes 1% of the mean flow. Typically unstable linear modes lie within a narrow range of frequencies. Their growth rates are very slow compared to the frequency of oscillation. We may therefore consider the new flow to be periodic. The new periodic flow is now linearly unstable to secondary, typically three-dimensional modes.

In two-dimensional flows this instability has been documented, for example in the transition experiments of Klebanoff *et al.* (1962) and Kachanov (1994), and there are many analytical results (e.g. Bayly *et al.*, 1988; Herbert, 1988). The Λ -structures we have seen are signatures of this secondary instability and are considered to be a precursor to the breakdown into turbulent spots (Kachanov, 1994). The secondary instability occurs at Reynolds numbers close to that of experimentally observed onset of transition. The new stability problem involves a Floquet analysis. In Blasius boundary layers for example sub-harmonic disturbances are the most dangerous. This result is consistent with the N -type transition observed in the experiments of Kachanov *et al.* (1977), where the Λ -structures are staggered.

An alternate secondary instability is in a resonant-triad interaction (Craik, 1971), where a two-dimensional TS wave interacts with two oblique three-dimensional waves, the sum of whose wavenumbers is equal to that of the TS wave. This mechanism leads to C -type, breakdown which was described in section 1.1.

4.1 Governing Equations

The approach we follow is as in Bayly *et al.* (1988) and Herbert (1988). The new basic flow is periodic and is obtained from the linear stability analysis, described in Chapter 3. This basic flow is given by

$$v_{basic} = U(\vec{r}) + A_p \vec{v}_p \quad (4.1)$$

where $U(\vec{r})$ is the solution of Navier-Stokes equation and \vec{u}_p is the primary disturbance velocity, given by

$$\vec{v}_p = u_p(x, r, \theta, t) \hat{x} + v_p(x, r, \theta, t) \hat{r} + w_p(x, r, \theta, t) \hat{\theta}. \quad (4.2)$$

We have introduced a subscript p for the primary (linear) disturbance. A_p is the amplitude ratio of the disturbance velocity to the meanflow velocity. The direct interaction between primary instability modes is neglected, which means A_p^2 is neglected. In other words assuming $1 \gg A_p > A_s$, where A_s is the amplitude of the secondary disturbance, we get a linear system of partial differential equations whose co-efficients are periodic functions of t . The total velocity field is given by

$$\vec{v}_{tot} = v_{basic} + \vec{v}_s \equiv U(\vec{r}) + A_p \vec{v}_p + \vec{v}_s, \quad (4.3)$$

In normal mode form,

$$\begin{aligned} \vec{v}_s(x, r, \theta, t) = \frac{1}{2} & \left(\vec{v}_+(r) \exp[i(k_+x + m_+\theta - \omega_+t)] + c.c \right. \\ & \left. + \vec{v}_-(r) \exp[i(k_-x + m_-\theta - \omega_-t)] + c.c \right) \end{aligned} \quad (4.4)$$

For the flow under consideration, the growth/decay rates of primary modes are small, hence $d(A_p)/dt$ can be neglected during one period of time. As we have seen in Chapter 3, Squires theorem does not apply and therefore the primary modes must be taken to be three-dimensional.

Equations for the secondary instability are obtained by substituting 4.3 and 4.4 into the Navier-Stokes equations, retaining linear terms in the secondary disturbances, and deducting the primary stability equations. The streamwise component of the velocity u_+ and u_- are eliminated using the continuity equation. The final equations contain v , w and p . On averaging over x , θ and t , only the resonant modes survive, which are related as follows:

$$k_+ + k_- = \alpha, \quad m_+ + m_- = n \quad \text{and} \quad (\omega_+ + \omega_-)_r = \omega. \quad (4.5)$$

4.1.1 Secondary instability equations

The final stability equations are given by,

$$\begin{aligned} & \left\{ (U-c) \left(\frac{1}{r} + D \right) - U' - \frac{i}{k_+ R} \left[\frac{1}{r} \left(k_+^2 + \frac{m_+^2 - 1}{r^2} \right) + \left(k_+^2 + \frac{m_+^2 + 1}{r^2} \right) D - \frac{2}{r} D^2 - D^3 \right] \right\} v_+ \\ & + \left\{ (U-c) \frac{im_+}{r} + \frac{m_+}{k_+ r R} \left(k_+^2 + \frac{m_+^2 - 1}{r^2} + \frac{1}{r} D - D^2 \right) \right\} w_+ - ik_+ p_+ \end{aligned}$$

$$\begin{aligned}
& + \frac{1}{2k_-} \left[\frac{k_+}{r} u_p + \frac{i}{r^2} v_p - \frac{m_-}{r^2} w_p + k_- u'_p + (k_+ u_p - \frac{i}{r} v_p - \frac{m_-}{r} w_p) D - i v_p D^2 \right] v_-^* \\
& + \left[\frac{i}{2r} \left(n - \frac{k_+}{k_-} m_- \right) u_p + \frac{m_-}{2k_- r^2} v_p + \frac{i m_-^2}{2k_- r^2} w_p - \frac{m_-}{2k_- r} v_p D \right] w_-^* = 0 \quad (4.6)
\end{aligned}$$

$$\begin{aligned}
& - \frac{2im_+}{r^2 R} v_+ + \left[ik_+(U - c) + \frac{1}{R} \left(k_+^2 + \frac{m_+^2 + 1}{r^2} - \frac{1}{r} D - D^2 \right) \right] w_+ + \frac{im_+}{r} p_+ \\
& + \left[\frac{1}{2r} \left(\frac{\alpha}{k_-} - 1 \right) w_p + \frac{1}{2} w'_p + \frac{\alpha}{2k_-} w_p D \right] v_-^* \\
& + \left[- \frac{ik_-}{2} u_p + \frac{1}{2r} v_p + \frac{i}{2r} \left(m_+ - \frac{m_- \alpha}{k_-} \right) w_p \right] w_-^* = 0 \quad (4.7)
\end{aligned}$$

$$\begin{aligned}
& \left[ik_+(U - c) + \frac{1}{R} \left(k_+^2 + \frac{m_+^2 + 1}{r^2} - \frac{1}{r} D - D^2 \right) \right] v_+ + \frac{2im_+}{r^2 R} w_+ + p'_+ \\
& + \left[- \frac{ik_-}{2} u_p - \frac{im_-}{2r} w_p + \frac{\alpha}{2k_- r} v_p + \frac{v'_p}{2} + \frac{1}{2} \left(1 + \frac{\alpha}{k_-} \right) v_p D \right] v_-^* \\
& + \left[\frac{i}{2r} \left(n - \frac{\alpha m_-}{k_-} \right) v_p - \frac{w_p}{2r} \right] w_-^* = 0 \quad (4.8)
\end{aligned}$$

The operator D stands for differentiation with respect to the radial coordinate r . The boundary conditions are

$$\vec{v}_s = 0 \quad \text{at } r = 1, \quad (4.9a)$$

$$\vec{v}_s \rightarrow 0 \quad \text{as } r \rightarrow \infty, \quad (4.9b)$$

$$\text{and } p \rightarrow 0 \quad \text{as } r \rightarrow \infty. \quad (4.9c)$$

Equations 4.6, 4.7 and 4.8 and three corresponding equations in v_-^* , w_-^* and p_-^* together with the boundary conditions (equations 4.9) describe an eigenvalue

problem for the secondary instability. As in the case of primary instability the sign of c_+ determines the stability of the flow. The formulation leads to an eigenvalue problem with a dispersion relation

$$\mathcal{F}(\alpha, k_+, R, n, m_+, S, A_p, c_+) = 0 \quad (4.10)$$

where c_+ are the eigenvalues.

4.2 Method of solution

The equations 4.6 to 4.8 can be discretised and written in matrix form:

$$\begin{aligned} & \left[\mathcal{A} \right] \left[v_{s+} \quad w_{s+} \quad p_{s+} \quad v_{s-}^* \quad w_{s-}^* \quad p_{s-}^* \right]^T \\ & = c_+ \left[\mathcal{B} \right] \left[v_{s+} \quad w_{s+} \quad p_{s+} \quad v_{s-}^* \quad w_{s-}^* \quad p_{s-}^* \right]^T \end{aligned} \quad (4.11)$$

If the computational domain is covered by a grid of size N , \mathcal{A} and \mathcal{B} are $6N \times 6N$ matrices. The numerical solution of the system (4.11) thus gives $6N$ eigenvalues. The numerical method is similar to primary stability analysis as described in Section 3.3.

We first validate our code by comparing results for flat plate boundary layer. The equations 4.6 to 4.8 reduce to the secondary instability equations of a flat plate boundary layer by letting $S = 0$, $m_+ S \rightarrow \beta$, $m_- S \rightarrow -\beta$ and $nS = 0$. The results for zero pressure gradient boundary layer are compared with those of Herbert (1988) and found to be well matching (see figure 4.1). Results including the effect of curvature are not available.

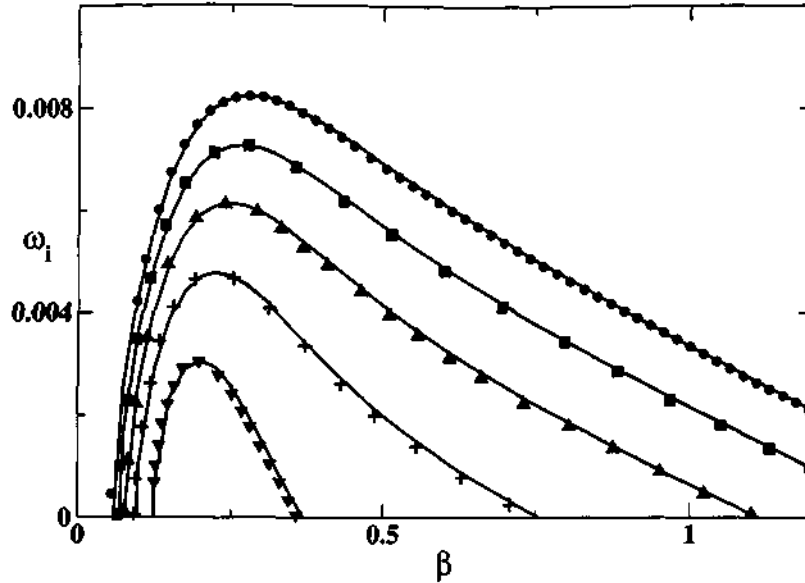


Figure 4.1: Growth rate of most dangerous secondary mode on a flat plate at a Reynolds number (R_θ) of 402.4. Solid lines: present computations; symbols: Herbert (1988). The amplitudes A_p for each curve from the bottom up are 0.002, 0.004, 0.006, 0.008 and 0.01.

4.3 Results and discussions

The results are given in detail below. The main findings are that instability is found at higher curvatures than in the linear stability analysis, but there is a maximum value for curvature for which instability is sustained. As in the case of a two-dimensional boundary layer subharmonic modes are dominant here too. It is found that secondary modes having opposite obliqueness are the most unstable. To be specific, the most unstable secondary modes are those with azimuthal wavenumber $m_+ = 2n$ and $m_- = -n$, where n is the azimuthal wavenumber of the primary. We have computed the growth rates for different primary modes and a range of Reynolds numbers and found that this relation holds for all cases.

The temporal growth rate of secondary modes along the streamwise direction at a Reynolds number of 1000 and $n = 1$ is presented in figure 4.2. The amplitude

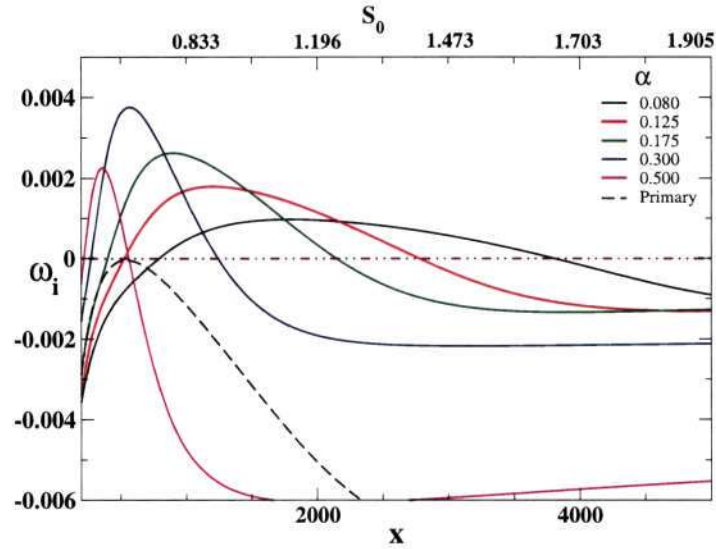


Figure 4.2: Growth rate of secondary disturbance waves along the cylinder axis for the non-axisymmetric mode $n = 1$ at $R = 1000$ and $A_p = 0.02$. The azimuthal wave numbers of secondary modes are $m_+ = 2$ and $m_- = -1$. The most unstable primary mode is shown by the dashed line.

A_p of the primary wave is taken to be 2% of U_∞ and the growth rate is computed for different primary wave numbers. The flow is found to be unstable to secondary modes whereas all the primary modes decay under these conditions. For comparison the growth rate of the least stable TS mode ($\alpha = 0.125$ and $n = 1$) is shown as a dotted line. At small primary wave numbers the growth rate is found to be small but for a wider band of streamwise locations. As the wavenumber increases the growth rate also increases and instability is restricted to a narrow streamwise region. The maximum growth occurs when $\alpha = 0.30$, and $k_+ = k_- = 0.15$. As discussed earlier the maximum growth occurs when $m_+ = 2$ and $m_- = -1$. Secondary modes also decay at higher curvature, but the extent of curvatures for which the instability is sustained is much larger.

The growth rate of secondary waves at higher Reynolds numbers ($=2000$ and

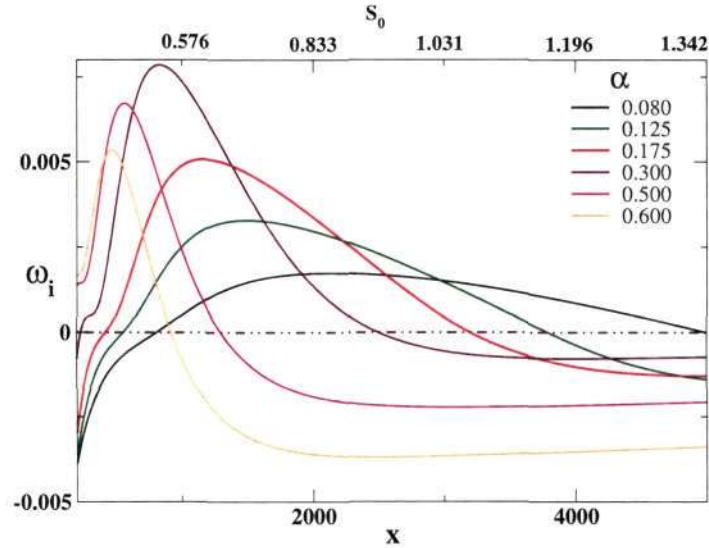


Figure 4.3: Growth rate of secondary disturbance along the cylinder axis for $R = 2000$. The other parameters are the same as in figure 4.2.

5000) where the primary is unstable are shown in figures 4.3 and 4.4. All other flow conditions are kept the same as in the previous case. The growth rate of the secondary modes is higher. A small local maximum of growth rate is found at low x .

The amplification rate of non-axisymmetric mode $n = 2$ for Reynolds numbers 3000 and 5000 are shown in figures 4.5 and 4.6 respectively. The azimuthal wavenumbers are $m_+ = 4$ and $m_- = -2$ and $A_p = 0.02$. The maximum growth rate is obtained when $\alpha = 1.5$. It is to be noted that primary mode is stable for these Reynolds numbers (see figure 3.25). Here all the disturbances decay at moderate curvatures. The large wavelength disturbances sustain themselves for larger range of curvatures compared to small wavelength modes.

Next we consider the non-axisymmetric mode $n = 3$. The flow is linearly unstable to this mode above a Reynolds number of 10110. As in the case of other

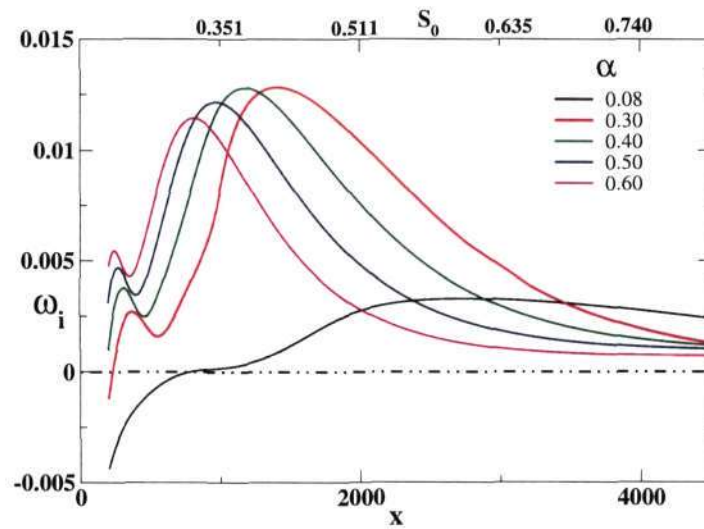


Figure 4.4: Growth rate of secondary disturbance along the cylinder axis for $R = 5000$. The other parameters are the same as in figure 4.2.

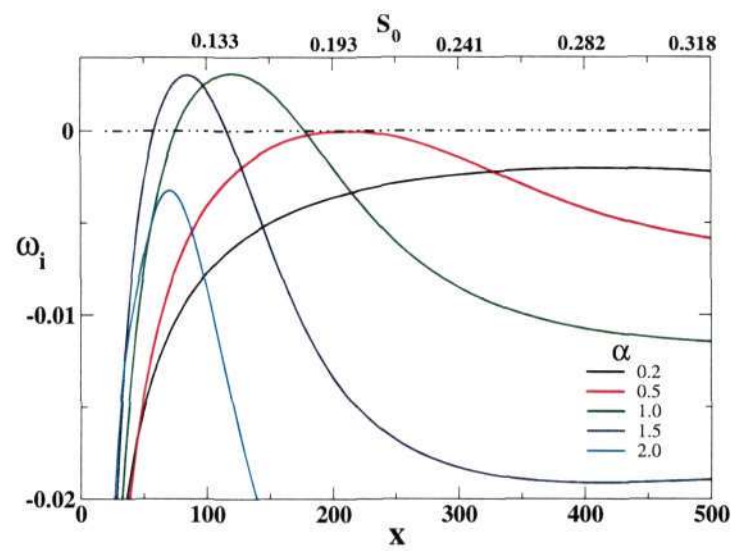


Figure 4.5: Growth rate of secondary disturbance waves along the cylinder axis for the non-axisymmetric mode $n = 2$ at $R = 3000$ and $A_p = 0.02$. The azimuthal wave numbers of secondary modes are $m_+ = 4$ and $m_- = -2$.

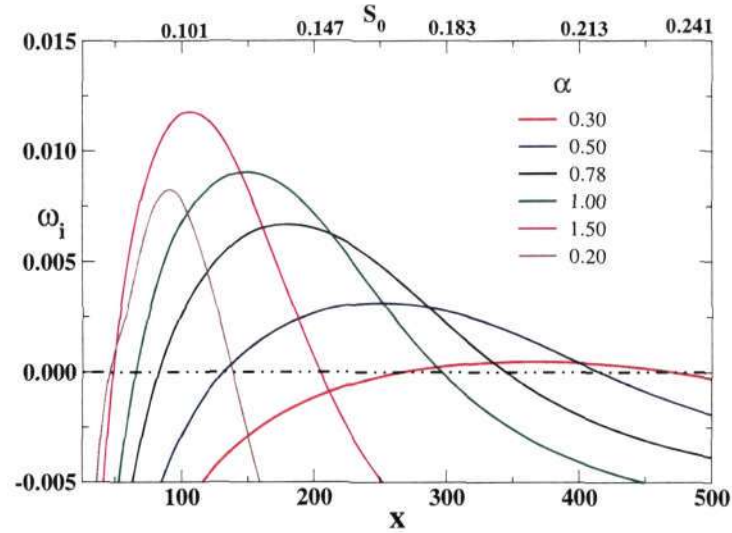


Figure 4.6: Growth rate of secondary disturbance along the cylinder axis for $R = 5000$. The other parameters are the same as in figure 4.5.

non-axisymmetric modes, the most unstable secondary has azimuthal wavenumbers $m_+ = 6$ and $m_- = -3$, and subharmonic modes are dominant. In figure 4.7 the growth rates of these modes are plotted. Note that the primary modes decay rapidly at this Reynolds number. The growth rate of secondary modes for a Reynolds number of 10,000 are presented in figure 4.8. The qualitative picture is the same but growth rates are higher.

Representative eigenfunctions for the secondary modes are shown in figures 4.9 to 4.13.

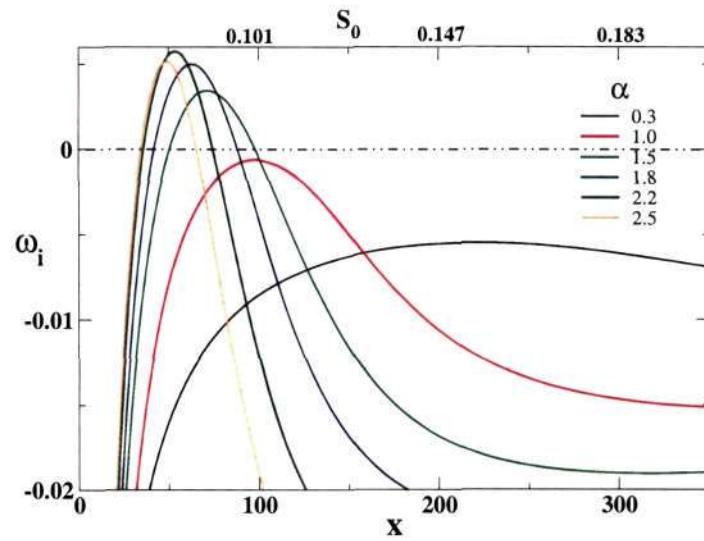


Figure 4.7: Growth rate of secondary disturbance waves along the cylinder axis for the non-axisymmetric mode $n = 3$ at $R = 5000$ and $A_p = 0.02$. The azimuthal wave numbers of secondary modes are $m_+ = 6$ and $m_- = -3$.

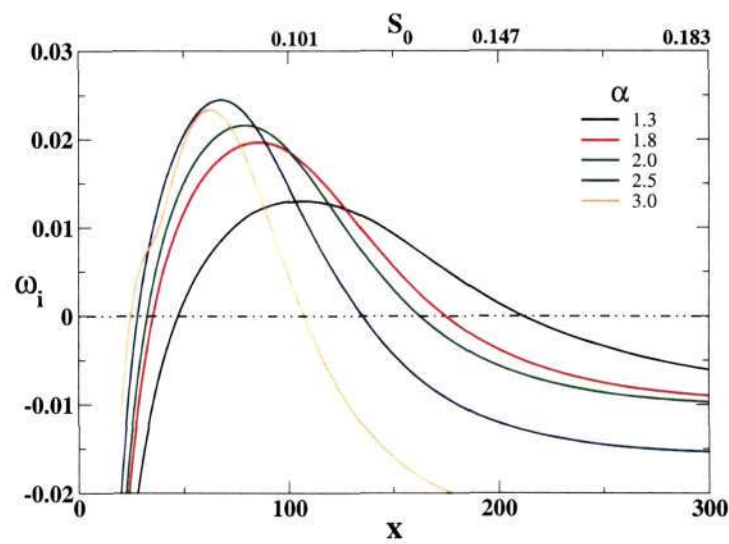


Figure 4.8: Growth rate of secondary disturbance along the cylinder axis for $R = 10,000$. The other parameters are the same as in figure 4.7.

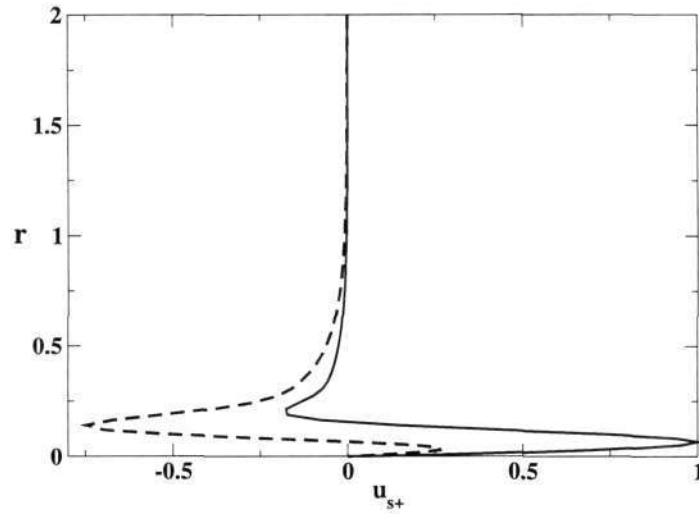


Figure 4.9: Axial component u_+ of the secondary disturbance. The Reynolds number is 1000, $n = 1$, $\alpha = 0.14$, $x = 200$, $k_+ = k_- = \alpha/2$. A_p of primary wave A_p is taken as 0.02. The solid and dashed lines are real and imaginary part respectively.

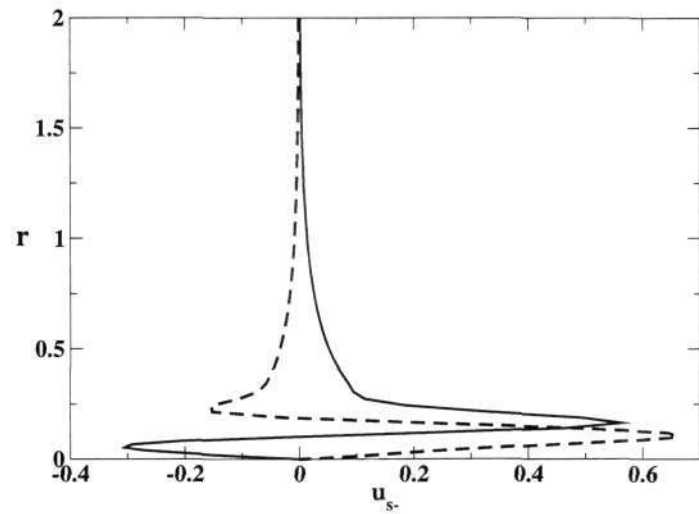


Figure 4.10: Axial component u_- of disturbance velocity. The parameters are same as the figure 4.9.

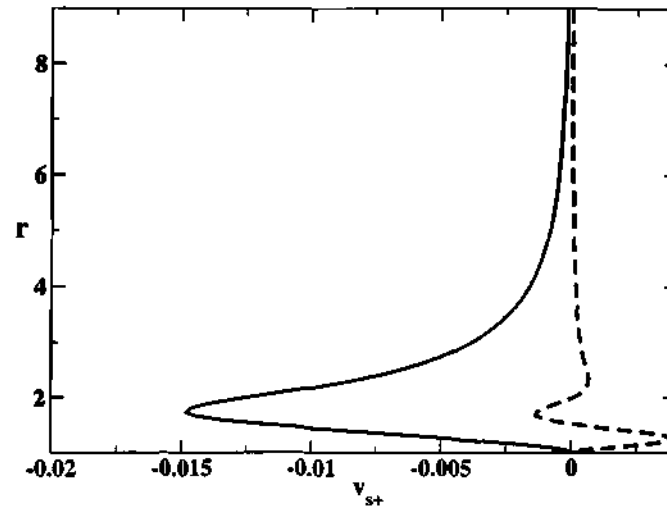


Figure 4.11: Radial component u_+ of disturbance velocity. The parameters are same as the figure 4.9.

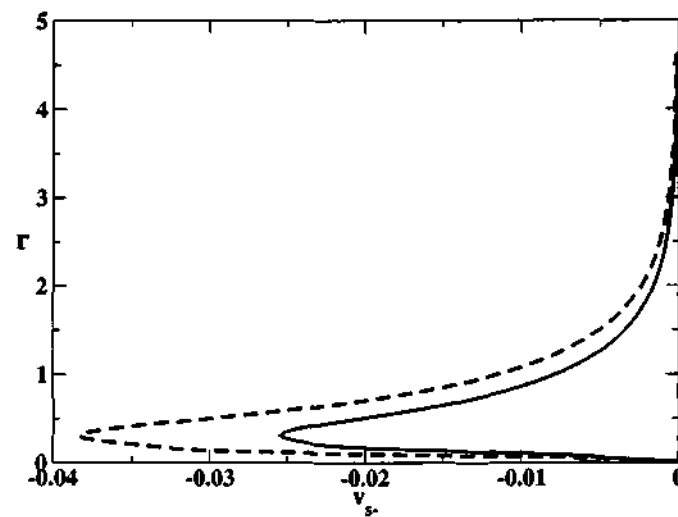


Figure 4.12: Radial component u_- of disturbance velocity. The parameters are same as the figure 4.9.

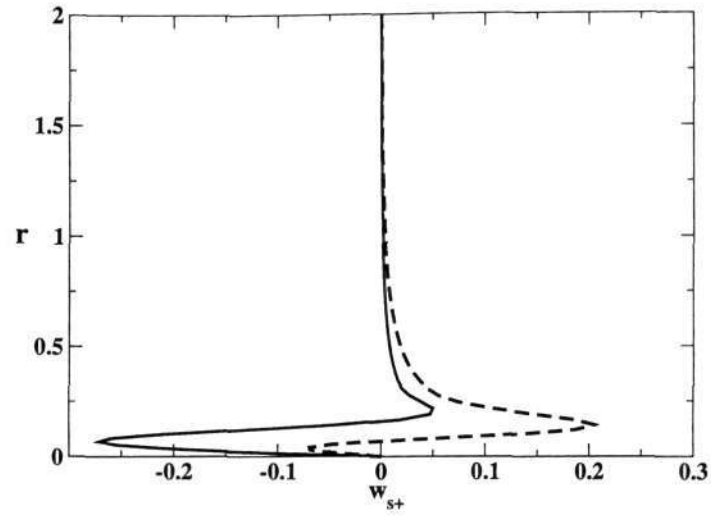


Figure 4.13: Azimuthal component w_+ of disturbance velocity. The parameters are same as the figure 4.9.

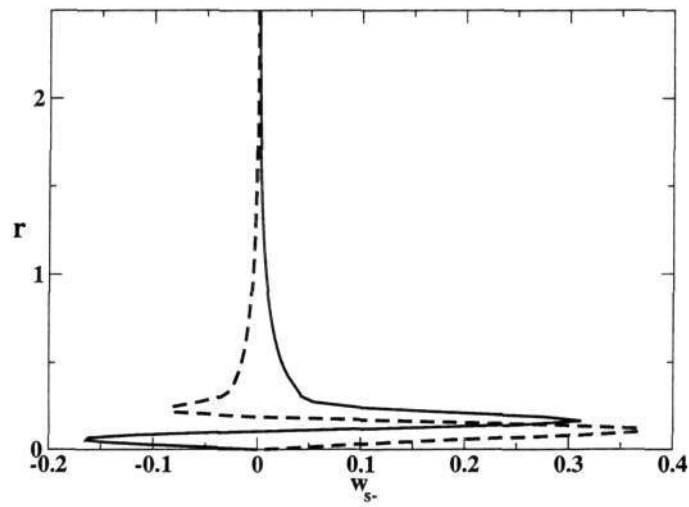


Figure 4.14: Azimuthal component w_- of disturbance velocity. The parameters are same as the figure 4.9.

4.4 Secondary instability analysis of two-dimensional boundary layers

We compute secondary instability for two-dimensional boundary layers. The results are used in chapter 5 for establishing a connection between the pattern of breakdown into turbulent spots and the laminar instability.

We study Falkner-Skan profiles, with the local freestream velocity $U_\infty = cx^m$, where m is the Falkner-Skan pressure gradient parameter. (The notation m is used here since it is standard, it is not connected to the azimuthal wavenumber m_+ and m_- used in the previous section). At a Reynolds number (based on momentum thickness and local freestream velocity) $R_\theta = 600$, with A_p taken to be 1% of U_∞ . The results have been checked to be representative of a wide range of R_θ and A_p . For all cases presented here, the most unstable secondary mode is the sub-harmonic, with a streamwise wavenumber $k (= k_+ = k_-) = \alpha/2$.

In figure 4.15 the growth of secondary modes at a Reynolds number of 600 in zero and adverse pressure gradient boundary layers are shown. The pressure gradient parameter considered here is $m = -0.06$. As seen from the figure the growth of secondary modes in an adverse pressure gradient is much higher compared to that of a Blasius boundary layer. The maximum growth occurs when $k_+ = 0.14$ for the adverse pressure gradient case, while $k_+ = 0.085$ gives the maximum for Blasius boundary layer.

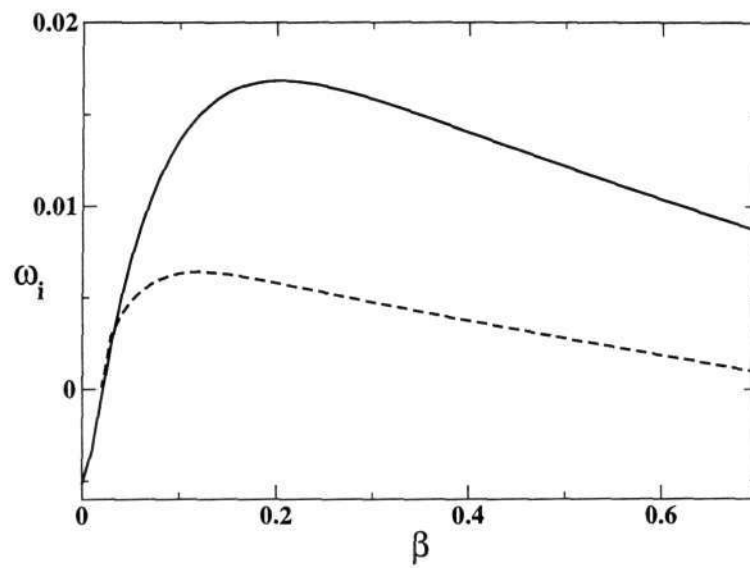


Figure 4.15: Growth rate of most dangerous secondary sub-harmonic mode at a Reynolds number $R = 600$ (based on the momentum thickness of the boundary layer and U_∞). Solid line: $m = -0.06, k_+ = 0.14$, dashed line: $m = 0, k_+ = 0.085$.

Part II

THE TRANSITION ZONE

CHAPTER 5

TRANSITION MODELLING IN BOUNDARY LAYERS

5.1 Introduction

We begin by recapitulating the transition process. The flow within a typical boundary layer is laminar close to the leading edge. With increasing streamwise distance, a sequence of events takes place until, far downstream, the boundary layer is fully turbulent. Much insight into the process which leads to transition has been gained over the past few decades. In incompressible two-dimensional boundary layers, at low freestream turbulence levels, the sequence of events from a laminar state to a turbulent state occurs through a TS wave mechanism, which is as follows. The first instabilities in low disturbance environments are linear and two-dimensional (see Bayly *et al.*, 1988). When these primary disturbances attain a certain amplitude, they are able to destabilize three-dimensional secondary modes (Hogberg & Henningson, 1998; Koch *et al.*, 2000; Malik *et al.*, 1994). Depending on several factors such as the amplitude of the primary mode, often either a sub-harmonic or a harmonic mode is dominant. This gives rise to a pattern of staggered (H-type/N-type, for Herbert/Novosibirsk) or aligned (K-type, for Klebanoff) vortices respectively (see e.g. Corke & Mangano, 1989; Herbert, 1988; Kachanov & Levchenko, 1984; Kachanov, 1994; Saric *et al.*, 1984; Zelman & Maslennikova, 1993). More details

were given in section 1.1.

We have conducted linear and secondary instability analyses in axisymmetric boundary layers as described in the previous chapters. The next step in the route to turbulence is the transition. Except for Lauchle & Gurney (1984) we were unable to find any experiments measuring transition zone parameters in axisymmetric boundary layers. However several such experimental results are available for two-dimensional zero and decelerating boundary layers (see e.g. Gostelow & Blunden, 1988; Gostelow *et al.*, 1994, 1995; Narasimha, 1985; Seifert & Wygnanski, 1995; Walker & Gostelow, 1990).

Due to a paucity of data in axisymmetric flows we switch temporarily to two-dimensional flows. Towards the end of the chapter we return to axisymmetric flow and make some predictions. No connection has been made between the laminar instability and spot breakdown even for two-dimensional flows. Our objective in this chapter is to make such a connection.

The secondary instability, either of TS waves or of streamwise streaks, is a precursor to turbulent spot breakdown. The two stages are separated by a short non-linear domain which we jump across. The question we pose is thus: does the regular pattern observed in secondary growth of disturbances give rise to any regularity in the birth of turbulent spots, contrary to the assumption hitherto that spot birth is totally random? To answer this we perform cellular automaton type stochastic simulations of spot breakdown (birth) and propagation in the transition zone, from which we obtain transition zone intermittencies.

In this thesis, we consider both low and high disturbance environments. For low disturbance levels a secondary instability analysis of the TS modes is performed and we establish a connection between the patterns made by different alignments of Λ vortices and inferred spot birth distribution. In a high disturbance environment

growing three-dimensional disturbances in a laminar boundary layer (via stream-wise streaks/concentrated patches of vorticity) finally become turbulent spots. The stability analysis of boundary layer at a very high free-stream turbulence level has been carried out by many researchers (see Brandt *et al.*, 2003; Brandt & Henningson, 2002; Matsubara & Alfredsson, 2001). We use their results for the secondary instability of streaks to perform the simulations to show again that patterns formed by the secondary instability is manifested by spot breakdown.

Our results indicate that a direct relationship between the birth of spots and the secondary waves is evident in strongly decelerating flows and in flat plate boundary layer at high free-stream turbulence (q , defined in equation 1.2) levels. In the boundary layer over a flat plate at low q , the connection is still likely to exist, but is difficult to observe for reasons discussed below. We therefore contend that decelerating boundary layers and/or flat plate boundary layers under high freestream turbulence are excellent candidates for exploring, both experimentally and numerically, the last nebulous frontiers of our understanding of the transition process in boundary layers.

5.1.1 Effect of pressure gradient

Adverse pressure gradient boundary layers are usually much more unstable than flat plate boundary layers. Corke & Gruber (1989), for example, observed much higher amplification rates than in Blasius flow, and a larger maximum amplitude of the fundamental mode with a shortened amplitude saturation region. The simulations of Liu & Maslowe (1999) reveal sub-harmonic three-dimensional waves to be the most dangerous in adverse pressure gradients. Here too, amplification rates are found to be much higher than in Blasius flow. Consequently, transition sets in

at a much lower Reynolds number in decelerating boundary layers. Secondly, the transition zone is much shorter (Gostelow *et al.*, 1994). However, the shape and downstream growth of turbulent spots is experimentally observed to be similar in all pressure gradients: a turbulent spot maintains an arrowhead shape when viewed from above, and remains self-similar as it grows (Narasimha, 1985; Seifert & Wygnanski, 1995). On a flat plate, the velocity of the leading and trailing edges of a spot are $U_h \sim 0.9U_\infty$ and $U_r \sim 0.5U_\infty$ respectively (see Narasimha, 1985), where U_∞ is the freestream velocity at the transition onset (x_t) and the subscripts h and r stand for 'head' and 'rear' respectively. A schematic diagram of spot growth in a flat plate boundary layer is given in figure 1.4. In adverse pressure gradients, e.g., when the pressure gradient parameter $m \approx -0.06$, the experiments of van Hest *et al.* (1994), give $U_h \sim 0.9U_\infty$ and $U_r \sim 0.4U_\infty$. The angle (ζ) subtended by the spot projected onto its location of birth is about 10° in zero pressure gradients, while in a strongly decelerating flow, Gostelow *et al.* (1994) found that it could be as high as 24° .

5.2 The transition zone

It is relatively straightforward to measure average transition zone quantities such as the intermittency, the burst rate and the persistence time distribution of laminar or turbulent flow as functions of the streamwise distance. The intermittency parameter is described in section 1.2. The burst rate B is here defined as the mean number of switches from laminar to turbulent flow per unit time at a given location, and the persistence time W of laminar flow is the duration of time for which the flow remains continuously laminar at a given location. The transitional intermittency has been measured in many experiments, but there are no data available for

the other measures, as far as we know. The burst rate may be expected to have a maximum somewhere in the middle of the transition zone. For a Poisson process, it is related to the local intermittency by

$$B \propto (1 - \gamma) (-\ln(1 - \gamma))^{1/2}. \quad (5.1)$$

The probability density function of persistence time W of laminar flow for a Poisson process can be written in the form

$$p(W + 1) \propto (1 - \gamma)^W (-\ln(1 - \gamma)). \quad (5.2)$$

5.2.1 Qualitative difference in pressure gradient boundary layer

We present here the observed qualitative difference in the behaviour of the transition zone in zero and adverse pressure gradients. (Favourable pressure gradient flows behave differently too, see Katz *et al.* (1990), but are not considered here).

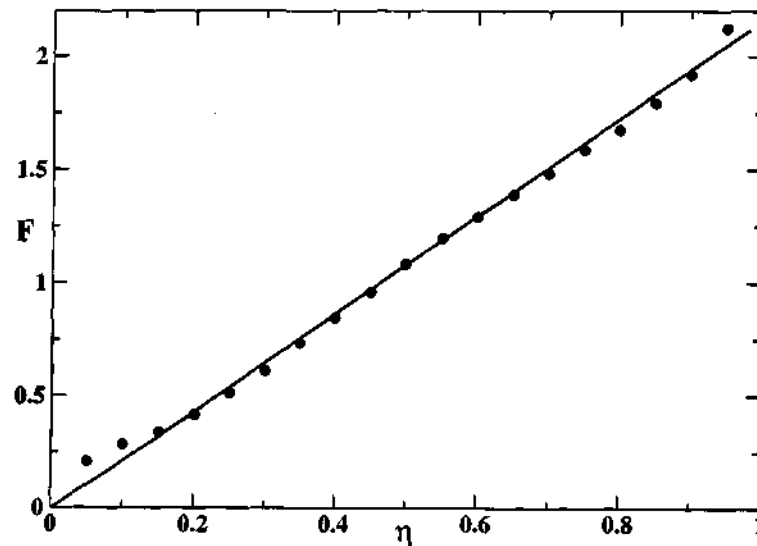


Figure 5.1: Growth of the intermittency parameter F in flat plate flow. Symbols: experiment Dhawan & Narasimha (1958).

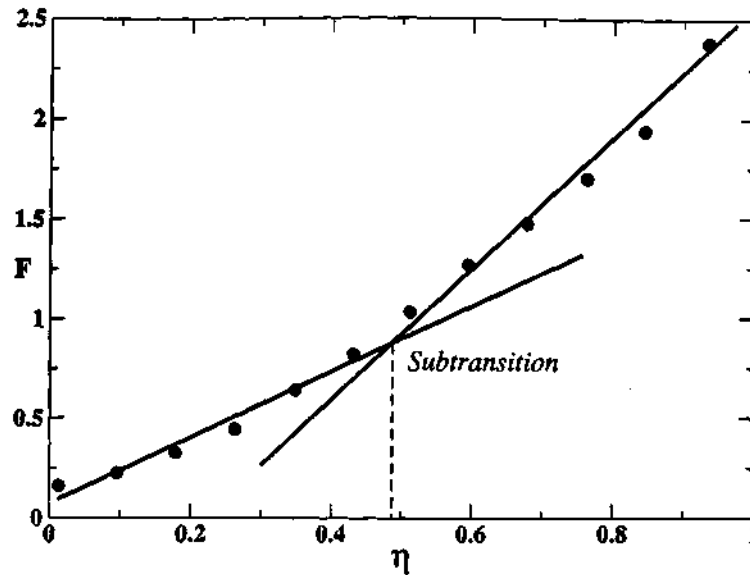


Figure 5.2: Adverse pressure gradient, $m = -0.05$. Symbols: experiment Gostelow & Blunden (1988); lines: best fit for data, depict observed sub-transition. L is the distance from x_t at which $\gamma = 99\%$.

The intermittency parameter F was defined in equation 1.4. While F in a large number of experiments in Blasius flow varies almost perfectly linearly with x (see figure 5.1), its variation in decelerating flows is different (figure 5.2). In the latter case the variation of F is slow in the initial region, followed by a distinctly rapid attainment of full turbulence. Narasimha (1984) modelled the observed variation as two straight lines, as shown in figure 5.2, and termed the change in slope a “sub-transition”. There is no satisfactory explanation for this sub-transition in adverse pressure gradients.

Differences in intermittency behaviour in adverse pressure gradient boundary layers can be brought about either by downstream variation of the spot propagation parameter, σ , or by changes (deviations from a Poisson distribution) in the nature of spot breakdown. Since the geometrical quantities remain fairly constant at a given pressure gradient [see Dey & Narasimha (1988); Seifert & Wagnanski (1995)],

σ is independent of x . A change in σ can therefore only alter the length of the transition zone, not the intermittency behaviour. (In flows where m varies strongly downstream, σ is likely to vary downstream. The simulations presented here can be suitably modified for such flows if experimental measurements of σ become available.) We therefore ask what will change $F(x)$ qualitatively. Walker & Gostelow (1990) argued that the reason the transition zone in an adverse pressure gradient is very short could be due to more frequent breakdown: once in every cycle of the basic Tollmien-Schlichting wave. We develop this idea here, and relate a periodic breakdown, not only to the length of the transition zone, but to the qualitative behaviour within the transition zone. Since the actual precursors to transition are the secondary (three-dimensional) modes, it is likely that the breakdown pattern is dictated by these modes rather than the Tollmien-Schlichting waves, as they had suggested. We show evidence here for a direct relation between the pattern made by the secondary waves and the birth of spots. We also propose an explanation for the experimentally observed phenomenon of sub-transition within the transition zone, based on the pattern of spot-merger that can be expected from instability. The merger scenario turns out to be similar to that proposed for axisymmetric boundary layers (Govindarajan & Narasimha, 2000; Narasimha, 1984).

5.3 The stochastic model and simulations

Stochastic simulations of the transition zone (using a cellular automaton-like approach) are performed. The simulations employ the hypothesis of concentrated breakdown and observed properties of spot growth and convection. We specify two different scenarios for spot breakdown. The first is a random breakdown, as used in the literature [see e.g. Narasimha (1985)], where spots appear in accordance with

a Poisson distribution, with no relation to instability. The second is regular breakdown, where most spots are born equally spaced in the spanwise coordinate and staggered in time; in the pattern decreed by the most unstable secondary mode. The former describes well the intermittency in mild or zero pressure gradient at low external disturbance. Our stochastic simulations using the latter predict extremely well the observed intermittency behaviour in high disturbance environments, as well as in decelerating boundary layers.

The transition zone (as viewed from above) is discretised into a rectangular grid in the streamwise (x) and spanwise (z) coordinates, a schematic is shown in Fig. 5.3. Each site is represented by an integer $\chi(X, Z, T)$, which is assigned a value 0 if the flow there is laminar and 1 if it is turbulent. (Upper case variables are used here to represent discretised quantities.) All spots are born at $X = 1$, which corresponds to the location x_t of transition onset. Each spot is approximated to be triangular, but the precise shape is immaterial to our results. Several simulations have been performed using much blunter and sharper spot shapes. The intermittency behaviour is not very sensitive to the shape, unless the spot is very close to rectangular. As detailed experimental information on spot propagation and shape, especially in adverse pressure gradients, becomes available, these could be incorporated into the simulations. During each time interval ΔT , the head of a spot moves forward by two grid locations, while its rear moves by one location. This is a discrete approximation of observed forward velocities in any pressure gradient, see Section 1.2. Simultaneously, the spot spreads laterally on each side by one spanwise grid location. The aspect ratio $\Delta Z/\Delta X$ of the grid thus corresponds to the tangent of the half-angle ζ of lateral spot propagation. Simulations with more complicated longitudinal spot propagation rules have been conducted with

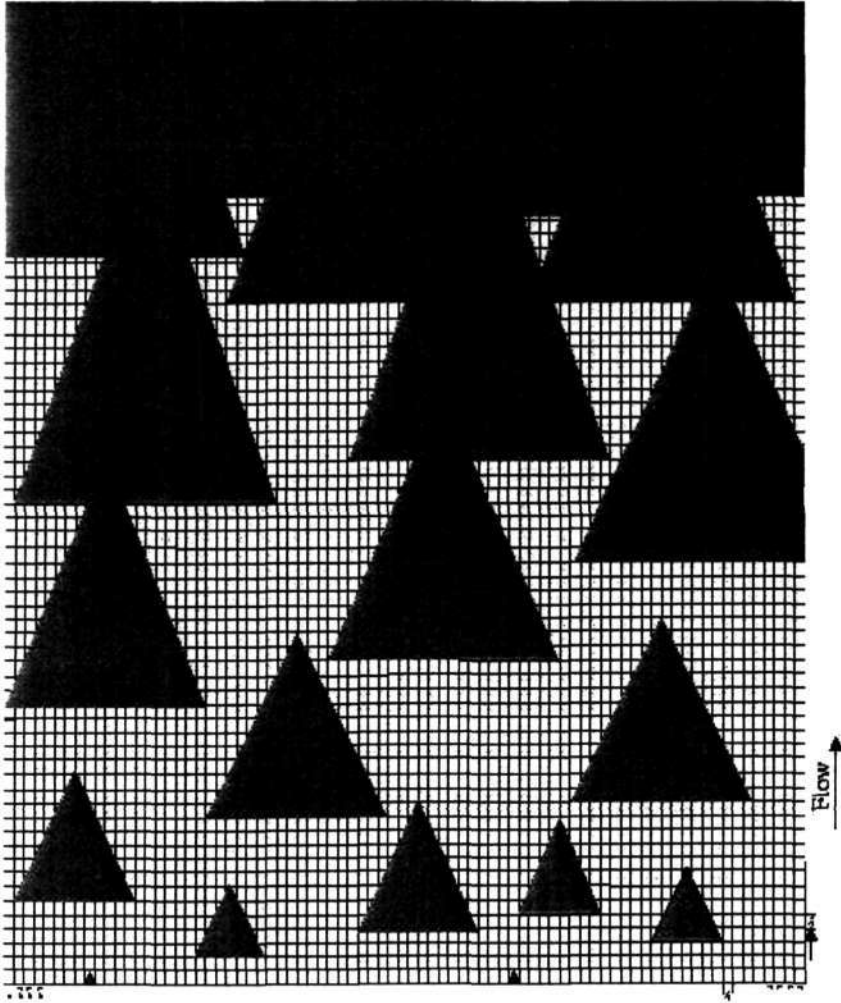


Figure 5.3: Schematic diagram of the simulation domain. This figure corresponds to a random breakdown scenario, where spots appear according to a Poisson distribution in time, and are uniformly distributed in the spanwise direction.

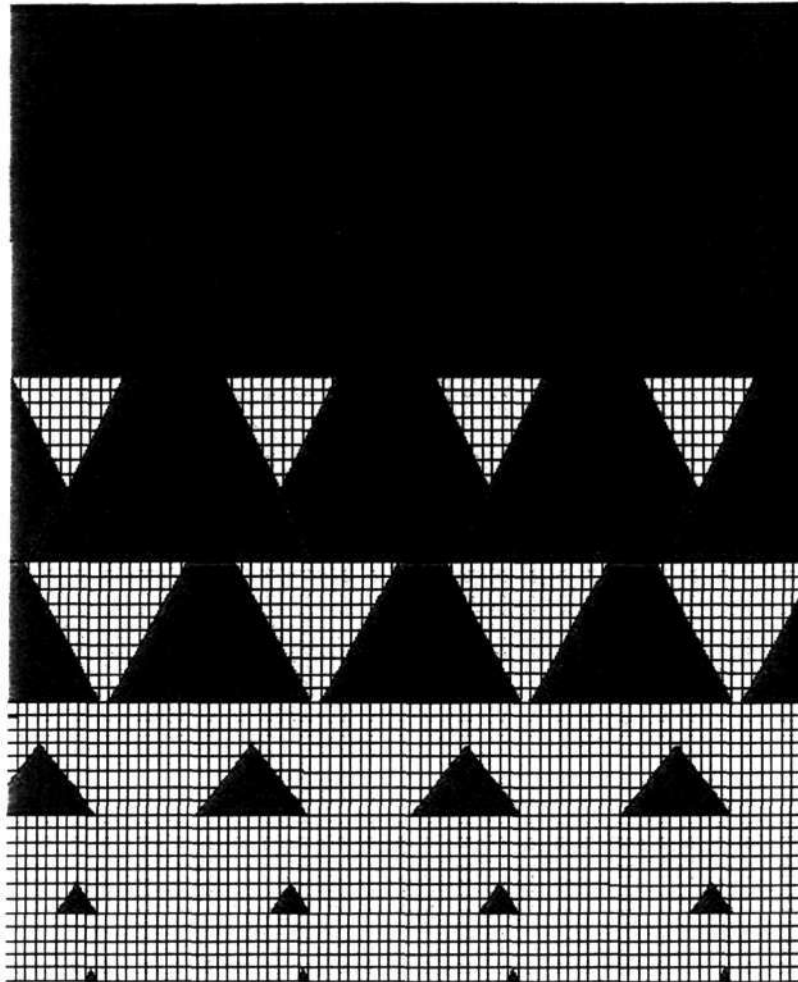


Figure 5.4: Schematic diagram of the simulation domain with a regular breakdown. Spots are formed at regular intervals in the spanwise direction and are staggered after every time period, as dictated by the secondary instability. The harmonic arrangement is shown here.

little difference to the results. The simulations are performed over long times (after achieving a statistical steady state) by prescribing a particular rule for spot generation with a given mean generation rate n per unit spanwise length per unit time at x_i . In the cases presented, the number of sites L_x and L_z in the streamwise and spanwise directions respectively are taken to be $L_x = 200$ and $L_z = 400$. Spot statistics are obtained by averaging over 5 million time steps after the first 50,000, which is sufficient time for the simulations to reach a statistically steady state. At each end of the span 50 sites are ignored in the averaging procedure to avoid edge effects. Alternatively, periodic boundary conditions may be applied in the spanwise direction, but we found no difference in the intermittency if L_z is high enough. The intermittency at a given streamwise location is obtained by averaging χ over the span and time.

With random spot generation, i.e., with spots appearing in accordance with a Poisson distribution in time and a uniform distribution in z , the simulations (as they should) bear out equation (1.4) and the variation of parameter F is linear as shown in Fig. 5.1.

We next prescribe a spot breakdown which is periodic in the spanwise direction and staggered in time. The term “staggering” is used here to represent obliqueness, and not the pattern observed in sub-harmonic breakdown. The staggering is related to ratio of wave numbers (α/β) , as follows. During the first time interval, one spot is generated every N_z sites at $X = 1$, and $Z = kN_z + i$, $k = 0, 1, 2 \dots L_z/N_z$, where i is an integer between 1 and N_z . After N_t time steps, in the case of harmonic secondary waves, the spots form at spanwise locations which are staggered by one grid location with respect to the earlier. Hence for a harmonic arrangement of spot precursors, $Z = kN_z + j$, where $j = i + 1$. In the case of sub-harmonic breakdown of secondary waves, which is more commonly observed in boundary layers, the

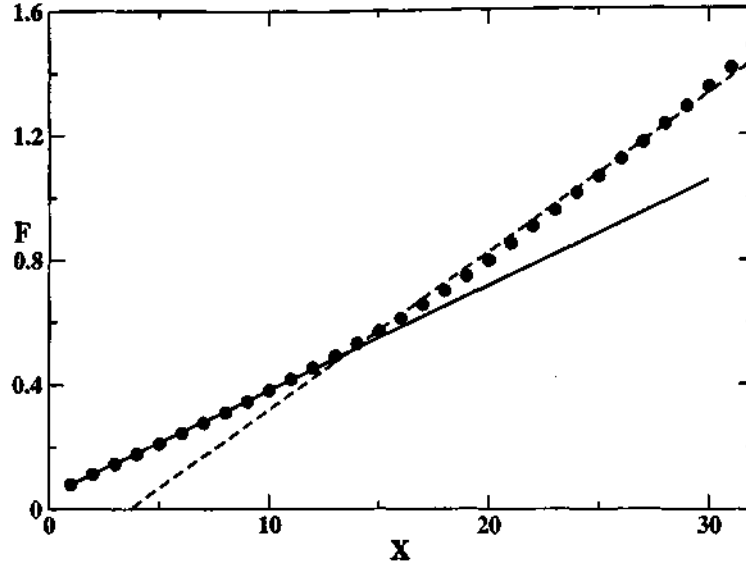


Figure 5.5: Variation of intermittency parameter in harmonic breakdown for $N_z = 49$ and $N_t = 10$. Symbols: regular breakdown, solid line: random breakdown. The mean spot generation rate is $N = 0.01$ in both cases. The dashed line shows the best linear fit for the downstream part of F .

corresponding breakdown locations are $Z = (k + 1/2)N_z + j$. The spot formation rate is now given by $n = L_z / (N_z \Delta Z N_t \Delta T)$. This prescription corresponds to spots forming at the crests of an oblique wave of spanwise and streamwise wavenumbers

$$\beta = \frac{2\pi}{N_z \Delta Z} \quad \text{and} \quad \alpha = \frac{2\pi}{N_t \Delta T v} \quad (5.3)$$

respectively, where v is the streamwise velocity of the wave crest. The phase of the oblique wave is randomised with a small probability (1%), and a small fraction (5%) of the spots are generated randomly.

In Fig. 5.5 and 5.6 it is demonstrated that intermittency behaviour is sensitive to the ratio of spanwise to streamwise wavenumbers; this fact will be used to strengthen the connection we make between instability and its signature in macroscopic parameter measurements in the transition zone. It is immediately evident

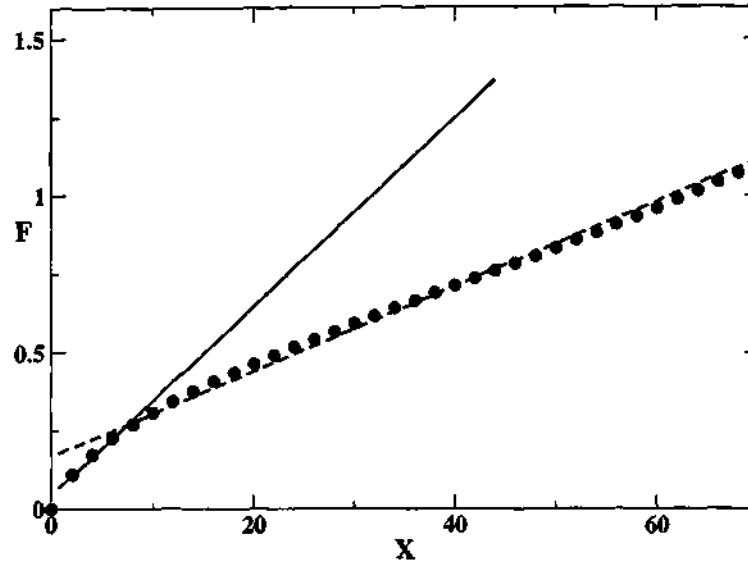


Figure 5.6: Variation of intermittency parameter for $N_z = 10$ and $N_t = 49$. Symbols: regular breakdown. All other parameters are same as in figure 5.5.

that the intermittency behaviour with a dominant regular component in the breakdown is very different from that in random breakdown. In figure 5.5 the slope in the later portion of the transition zone is seen to be much higher than in the early part. In this case, a relatively sharp “sub-transition” could be imagined between $X = 13$ and $X = 16$. The reader is cautioned however, that this sharpness in the change is an artefact of the birth location of all spots having been fixed at the same location $X = 1$. In reality, spots will form in a narrow neighborhood around $X = 1$. This, and any increase in randomness, will affect the merger scenario discussed below, and a more smooth slope change will result. This simulation is made for demonstration of the merger scenario we propose. The slope change observed here is just downstream of the location ($X = 11$) at which the heads of a set of spots formed at a time T just touch the rears of the spots formed at $T - N_t \Delta T$. In the simulations of Fig. 5.6, all parameters have been kept the same, except that the values of N_z and N_t have been switched. In this case the spots touch each

other laterally first (at $X = 6$) downstream of which a sharp sub-transition is again evident. At low F , i.e., upstream of spot merger, the intermittency behaviour in each case is exactly the same as that when spots form randomly (with the same breakdown rate). This is not surprising, given that the spots are too small to “see” each other. At higher intermittencies, quite surprisingly, for the same mean breakdown rate and identical spot growth, the length of the transition zone is seen to be very different, which tells us that spot-merger plays a large role in transition. A purely lateral merger as in Fig. 5.6 results in a much higher degree of overlap (on both sides), and consequently, less of the region is occupied by spots. This of course means that transition to turbulence will proceed much more slowly. A purely longitudinal overlap (Fig. 5.5) on the other hand, results in far less spot overlap, meaning more occupancy by spots, and a shortened transition zone. The latter scenario is closer to observations in adverse pressure gradients. This immediately begs the question: which kind of merger would be consistent with growing instability modes? As we shall see, a study of secondary instability patterns, both in adverse pressure gradient and in zero pressure gradient with bypass transition, tells us that the pattern corresponds very well with what we have in figure 5.5. The ratio of wavenumbers in zero pressure gradients at low free stream turbulence levels, on the other hand, does not give a clear answer.

Environmental disturbances play a large role in the transition process. In this work we have not considered these directly, except in the adhoc introduction of a randomisation of phase: cellular automaton type simulations afford us this and other luxuries, enabling us to isolate the effect of various parameters.

5.4 The connection between secondary instability and transitional intermittency

As mentioned earlier, the pattern of the breakdown, i.e., the periodicity in z and time and the staggering to be prescribed in the stochastic simulations are obtained from secondary stability analysis. The streamwise and spanwise wavenumbers for which the secondary wave grows fastest are found by the approach described in Chapter 4. For example, for an adverse pressure gradient flow of Falkner-Skan parameter $m = -0.06$, the maximum growth rate ω_i of the secondary instability wave is 0.067, and occurs when the wavenumbers k and β are 0.165 and 0.215 respectively. The corresponding phase speed is $0.524U_\infty$. Using the fact that the rear of a spot travels at approximately half the freestream velocity, we have $\tan \zeta = 2\Delta Z/U_\infty \Delta T$. The spot propagation angle is taken as $\approx 20^\circ$ [Gostelow *et al.* (1995)], and from equation (5.3) we may estimate the breakdown ratio N_z/N_t to be ~ 4.9 . The analysis is done at a Reynolds number R_θ of 220 to be consistent with experimental transition onset [Gostelow & Blunden (1988)]. Incidentally, the breakdown ratio is practically independent of Reynolds number, it changes only by 2% for a 50% change in Reynolds at this pressure gradient.

Figure 5.7 shows the intermittency variation obtained from the stochastic simulations, with the ratio N_z/N_t taken to be 4.9 ($N_z = 49$ and $N_t = 10$). A harmonic pattern of Λ vortices is assumed in this simulation. The streamwise distance η here is scaled in such a way that the locations of $\gamma = 25\%$ and $\gamma = 75\%$ match with those of the experiment. The results are in good agreement with experiments at $m = -0.06$. In particular, the experimentally observed change in slope of the intermittency parameter $F(x)$ is followed well by the simulations. Simulations with other combinations of N_z and N_t which maintain the ratio, e.g., 98 and 20, change

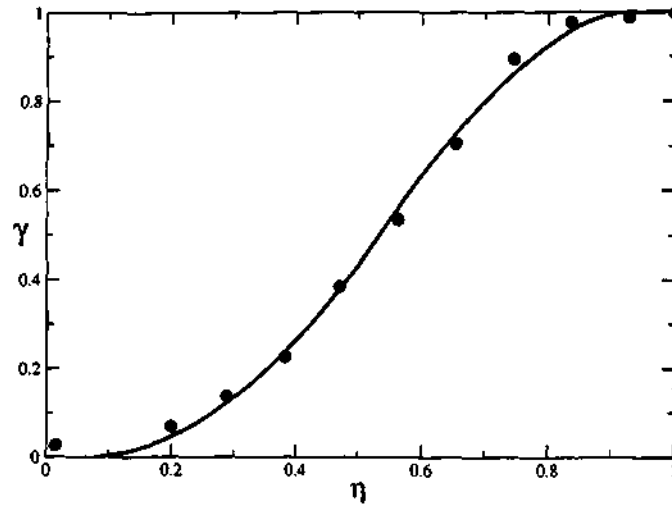


Figure 5.7: Variation of the intermittency in an adverse pressure gradient flow, $m = -0.06$. Solid line: stochastic simulations, with $N_z = 49, N_t = 10$, in accordance with the wavelengths of the dominant secondary mode; symbols: experiments (Gostelow & Blunden, 1988).

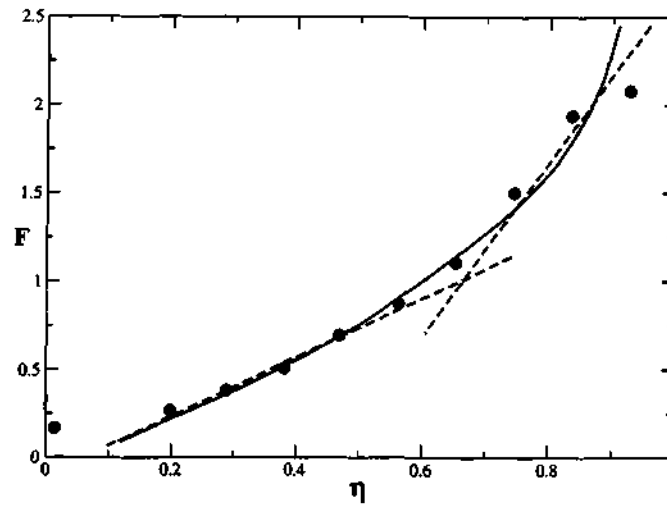


Figure 5.8: Variation of the parameter F for the data shown in figure 5.7. The dashed lines are the best fit of the observed F , as proposed in the sub-transition model of Narasimha (1985).

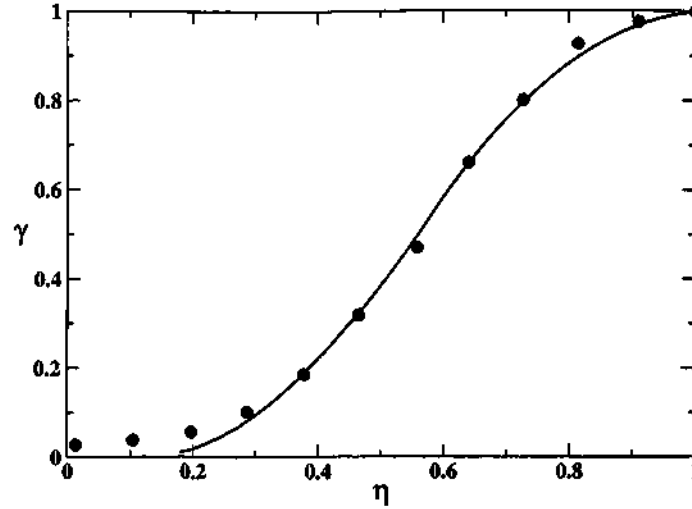


Figure 5.9: Variation of the intermittency in an adverse pressure gradient of $m = -0.04$. Solid line: stochastic simulations with $N_z = 39, N_t = 12$, from in accordance with the wavelengths of the dominant secondary mode; symbols: experiments (Gostelow *et al.*, 1994).

the effective size of the grid, and give results very close to this one, as expected. In figure 5.8 we also indicate by two straight lines what would be the best-fit if the sudden change in slope of parameter F proposed by Narasimha (1985) were to be valid. In figure 5.9 and 5.10 we consider a slightly less adverse pressure gradient, $m = -0.04$. The ratio N_z/N_t obtained from the stability analysis is 3.23 and in the stochastic simulations we use $N_z = 39$ and $N_t = 12$. From these and other comparisons (not shown), we may conclude that a spot breakdown pattern as prescribed by the secondary instability gives rise to intermittency behaviour in qualitative agreement with experiments.

When the freestream turbulence level q is high, breakdown is triggered by a bypass mechanism. Intermittency data for such a situation for a flat plate boundary layer at $q = 0.015$ are available in Matsubara & Alfredsson (2001), for which the ratio N_z/N_t is estimated from Andersson *et al.* (2001) to be about 5. Figure

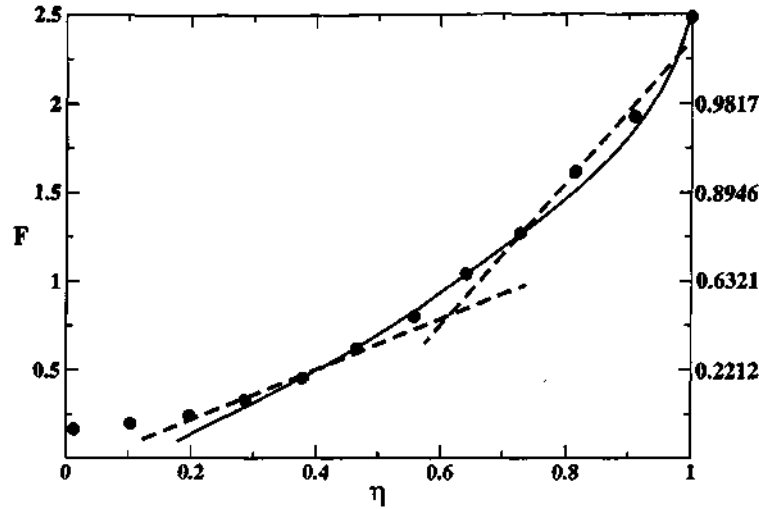


Figure 5.10: Variation of the parameter F for the data shown in Figure 5.9. (Gostelow *et al.*, 1994).

5.11 shows that simulations with this ratio compare very well with experimental measurements.

It may be noticed that there is some small discrepancy at the beginning and the end of the transition zone, where it is known that experimental data may be inaccurate: errors could arise unless the data is collected over extremely long times. Secondly, a short laminar patch within a turbulent signal (at γ close to 1) is often difficult to distinguish experimentally, as tiny patches of turbulence (at γ close to 0) can be difficult to distinguish from noise. It is also to be remembered that the hypothesis of concentrated breakdown is an idealisation: most spots in reality would be forming within a narrow streamwise strip around $x = x_t$, rather than at one particular location.

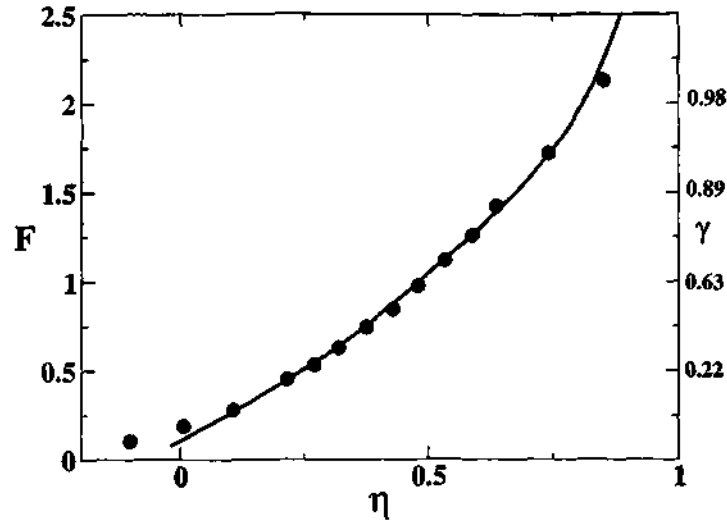


Figure 5.11: Transition through a bypass mechanism, streak breakdown. Symbols: experiment Matsubara & Alfredsson (2001); line: regular breakdown, $N_z/N_t = 5$.

5.4.1 Why there is no apparent connection in zero pressure gradient.

We now have seen that in adverse pressure gradient boundary layer as well as in high disturbance environments the intermittency variation is consistent with the pattern of instability waves while the results at low q and $m = 0$ seem to fit very well with completely random spot birth. If secondary instabilities play a role in spot birth, why then does random spot-birth explain observations so well here? The answer is two-fold: (i) The spanwise/streamwise wavelength ratio of the dominant secondary mode is such that the slope change to be expected is small in this case (as discussed with figure 5.12 and 5.13). (ii) the spot breakdown is not expected to be as regular as in adverse pressure gradients, as discussed below.

The ratio of wavelengths of the dominant modes is shown as a function of the pressure gradient in figure 5.12. The ratio decreases with decreasing pressure

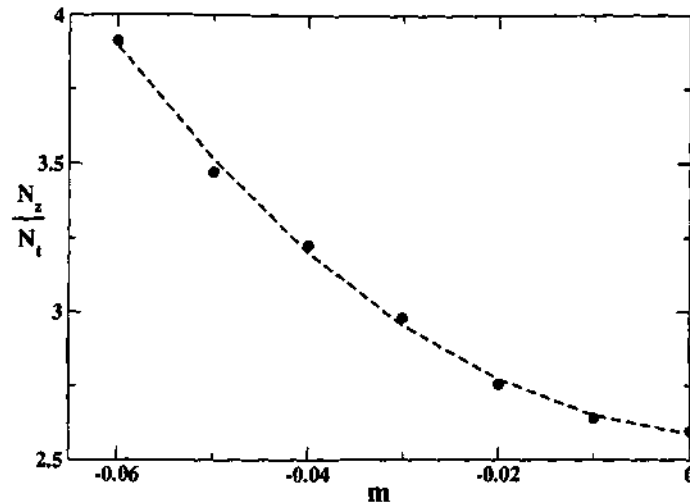


Figure 5.12: The variation of the breakdown ratio (N_z/N_t) as determined by the most unstable secondary instability with adverse pressure gradient (m).

gradient, and N_z/N_t is about 2.3 for a Blasius boundary layer (since now $k = 0.085$, $\beta = 0.146$ and $v = 0.353$ for the most dangerous mode). We would first like to see how the intermittency would vary if the breakdown were to be predominantly regular. The results of such a simulation are shown in figure 5.13: a linear F is seen upto about $\gamma = 0.75$, while at high values of intermittency, the slope increases. From the discussion on Fig. 5.5 and 5.6, we may expect that spot mergers are now a combination of lateral and longitudinal, with longitudinal being marginally dominant. The weakened dominance takes a greater streamwise distance to be displayed in the intermittency slope.

Secondly the actual breakdown in Blasius flow is likely to comprise a much higher random component than this simulation assumes. There are various reasons to expect this. In Blasius flow, wave packets may be expected to undergo a significant amplitude modulation, which would result in different waves reaching the critical amplitude at different streamwise stations. This means that spot birth could be smeared out over a streamwise distance. In the case of decelerating flow,

Pressure gradient (m)	Reynolds number	phase speed	group velocity
0	200	0.412	0.295
0	600	0.353	0.188
-0.06	200	0.492	0.655
-0.06	600	0.510	0.666

Table 5.1: Typical phase and group velocities in Blasius and decelerating boundary layers.

the group velocities of the waves are much larger, as seen in table 5.1, and the amplitude modulation would therefore take place over a much shorter length. Another reason is that secondary waves in an adverse pressure gradient are amplified much faster than on a flat plate. This is demonstrated in Figure 5.14. The amplification of the secondary mode is computed by making a quasi-static assumption about the primary wave. Since the primary wave is slowly growing, we assume that the secondary mode at a given time can be computed by taking the primary wave to be of constant amplitude, this is a temporal analog of the “parallel-flow” assumption often employed in spatially-developing flow. It is to be noted that the growth of the secondary mode can be faster than exponential, since ω_i is directly related to A_p . As expected, secondary instabilities grow much faster in a decelerating flow than over a flat plate. Therefore within a very short time span most of the waves achieve the threshold required for breaking down into spots. In the zero pressure gradient case the attainment of the required threshold is much slower, offering greater opportunity for stochastic effects.

In addition, the wavelength ratio of the dominant mode varies significantly with primary disturbance amplitude in flat-plate flow (see Zelman & Maslennikova, 1993). This, however, is not the case in strongly decelerating flow, as seen in table

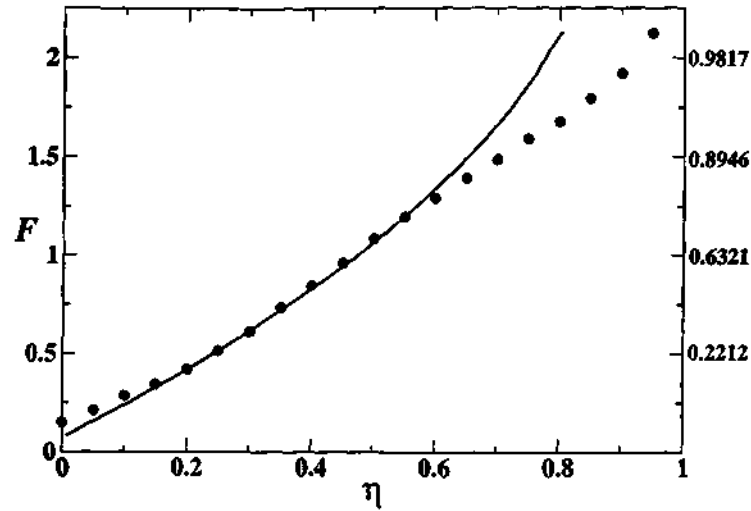


Figure 5.13: Variation of intermittency parameter F in the boundary layer over a flat plate. Solid line: stochastic simulations with $N_x = 32, N_t = 13$ as dictated by secondary instability; dots are the experimental data in zero pressure gradient boundary layers from Dhawan & Narasimha (1958).

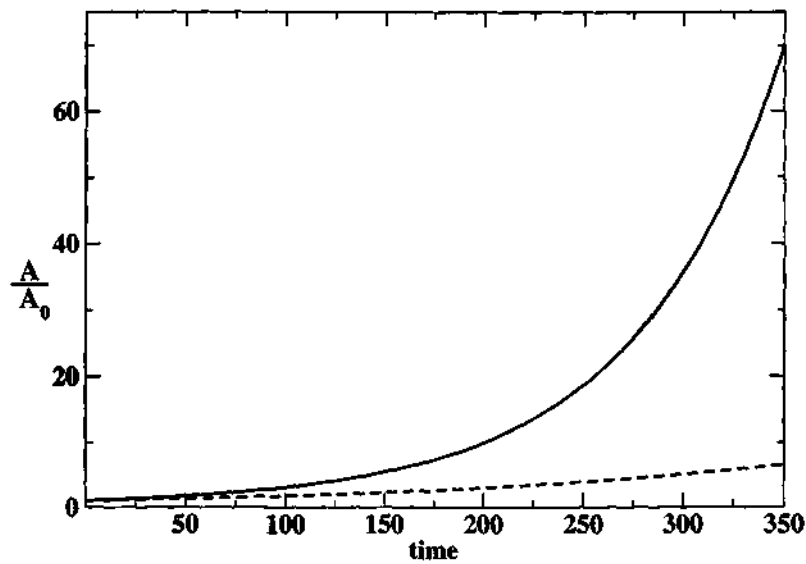


Figure 5.14: The variation of amplitude of secondary disturbance wave with time in adverse ($m = -0.06, \alpha = 0.185$ and $\beta = 0.12$, solid line) and zero ($\alpha = 0.13$ and $\beta = 0.805$, dashed line) pressure gradient boundary layers.

		k_+/β	
A_p	R	$m = 0.00$	$m = -0.06$
0.01	200	0.77	0.75
0.005	200	0.91	0.70
0.01	600	0.65	0.70
0.005	600	0.81	0.75

Table 5.2: Effect of the primary disturbance amplitude on the obliqueness of the most dangerous mode.

5.2. Hence, if the primary disturbance contains a range of amplitudes, the Blasius boundary layer would show a more random birth, with the corresponding constant slope in the intermittency parameter.

5.5 Measures to infer the breakdown scenario

The space-time distribution of spot birth in a natural transition boundary layer is difficult to measure directly. We may however infer the nature of the breakdown in quite a straightforward manner by measuring transition zone quantities as a function of the streamwise distance, and comparing with stochastic simulations. An example of this is of course the transitional intermittency, which has been discussed in detail. As discussed in Chapter 1, the spot birth scenario can be reconstructed with the help of several other easily measurable quantities, such as the burst rate and the persistence time distribution of laminar flow.

The present simulations with a random breakdown prescribed give rise to burst rates which agree well with the relationship given by equation 5.1, as seen in Figure 5.15. Any deviation from this behaviour is a sign that spot breakdown is not random. When the breakdown is mostly regular, it is clear that the burst rate distribution is more “peaky” and symmetric with respect to $\gamma = 0.5$ than when

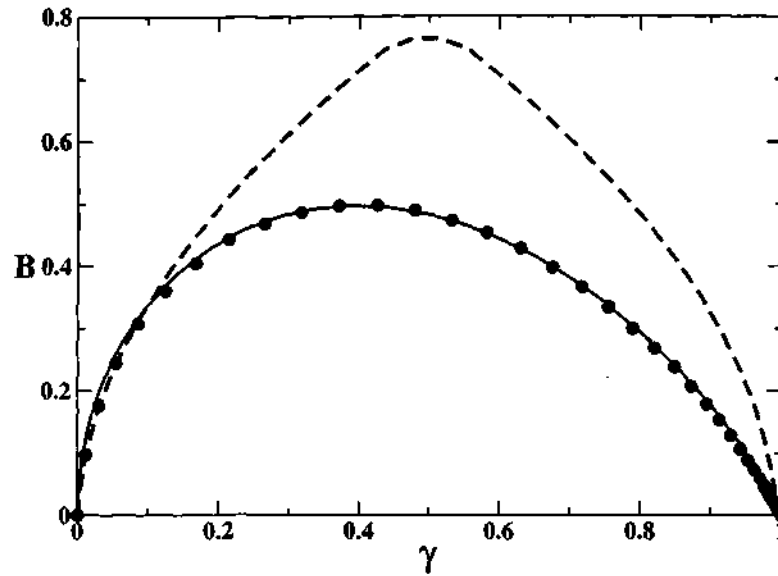


Figure 5.15: Variation of the burst rate with the intermittency γ for different scenarios of spot breakdown. Symbols: Random breakdown according to Poisson distribution, Solid line: equation 5.1, Dashed line: regular breakdown.

the breakdown is random. The burst rate variation with intermittency is the same for sub-harmonic and harmonic type breakdowns. We suggest here that there is a need for experimental measurements of this quantity, especially in adverse pressure gradient boundary layers, which will help us quantify the breakdown scenario.

The probability density function of the persistence time w_t , defined here as the extent of time that the flow continuously remains laminar is plotted in figure 5.16. The data is obtained by running the simulation over 20 million time steps (after reaching stationary state), monitoring a particular streamwise location in the middle of the span (in this case $X = 15$, $N_z = 40$, $N_t = 10$) and collecting the statistics of lengths of strings of zeroes between two 1's. In the case of random breakdown, the pdf of the persistence time decays exponentially with persistence time, whereas

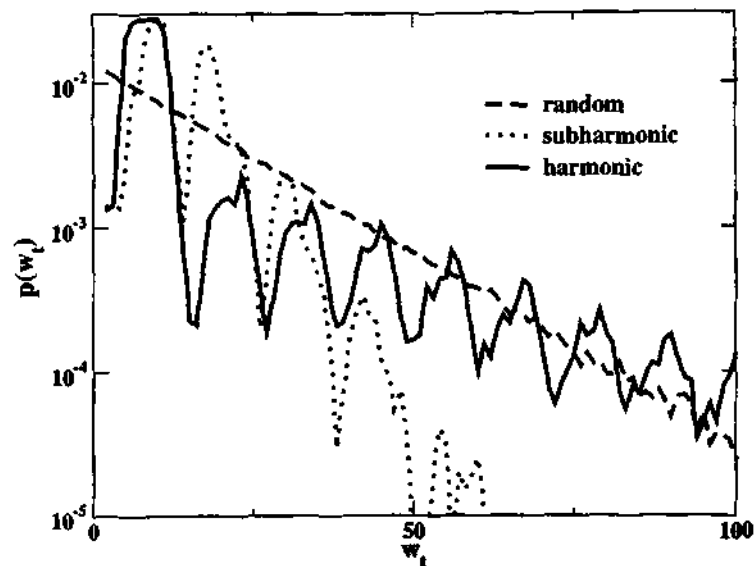


Figure 5.16: Probability density function (pdf) of 'persistence time w_t '.

in the case of regular breakdown, an overall decay is significantly modulated by ups and downs. The persistence times of laminar flow are significantly shorter for sub-harmonic breakdown than for harmonic as is to be expected. We present here only the basic idea. Further theoretical and experimental efforts are called for before the connection between instability and the transition region is completely understood.

5.6 Effect of concentrated breakdown

Narasimha (1957) proposed the hypothesis of concentrated breakdown in which all spots form within a narrow spanwise belt around the location of transition onset, i.e., within $x_t \pm \epsilon$, where $\epsilon \ll x$. While the intermittency behaviour resulting from the hypothesis and the assumption of a random breakdown matches experiment very well in constant-pressure low-disturbance environments, its validity has been

a matter for debate, see e.g. Johnson & Fasihfar (1994). Since a particular disturbance amplitude is achieved at a particular Reynolds number, it is plausible at least that upstream of a given x location, no spots will form. A large number of spots are likely to form in the vicinity of x_t , but given that instability modes which are not dominant could continue to grow in the transition zone, a small number could be born at any location downstream. We conduct simulations to estimate how much the intermittency and other parameters depend on making this hypothesis. We do this by allowing an increasing fraction of the spots to form with equal probability anywhere downstream of x_t . A random breakdown is prescribed. Our conclusion is that even in the unlikely event of a large fraction of spots being born downstream, the intermittency is dominated by spots forming at x_t , since at any given x , these spots are much larger than those born more recently.

The intermittency distributions for the extreme cases tried are shown in figure 5.17. It is seen that even when 80% spots form downstream of the onset location, the variation of F is still practically linear. However when all the spots are born downstream of x_t , as modelled by Emmons (1951), there is a noticeable departure from linearity. In an instability-driven transition, this last situation is highly likely, as discussed above. It may be noticed that the intermittency behaviour in the case of Emmons breakdown (spots born with equal probability anywhere in the domain) does not appear very different qualitatively from a regular breakdown (all spots forming at x_t , but according to a prescribed pattern), and would thus be difficult to distinguish in an experiment. However, an experiment which measures persistence times can distinguish very simply between them, as is evident from figure 5.18. In an Emmons breakdown, the persistence time distribution decays exponentially, but with a smaller slope than for the concentrated breakdown, as expected.

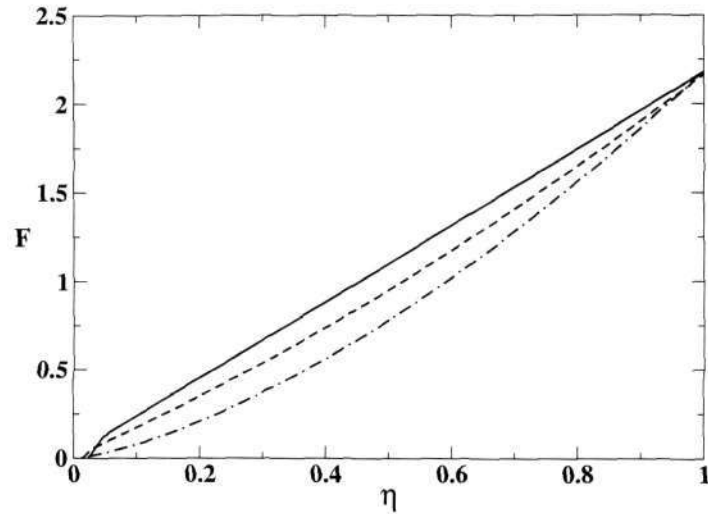


Figure 5.17: Effect of the hypothesis of concentrated breakdown on the intermittency distribution. Solid line: spots are allowed to form only at x_t . Dashed line: 80% spots are born downstream of the onset location. Dot-dashed line: all spots form downstream of the transition onset (Emmons breakdown). The x -axis is scaled with $x_{\gamma=0.99}$

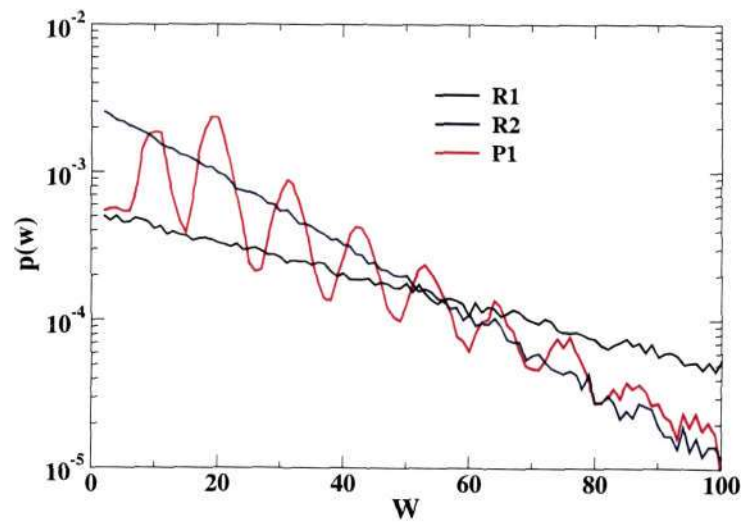


Figure 5.18: Effect of concentrated breakdown on persistence time distribution. The persistence time is computed at the location where intermittency $\gamma = 0.1$. The curve marked R2 is according to the hypothesis of concentrated breakdown, R1 is for random breakdown anywhere downstream of x_t (Emmons, 1951), P1 represents periodic breakdown (sub-harmonic), the pattern is obtained from secondary instability.

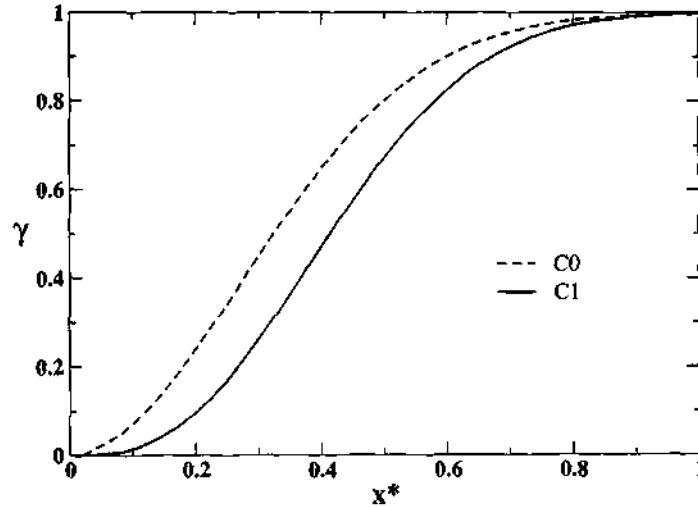


Figure 5.19: Effect of the calmed region behind a spot on the intermittency for a random breakdown scenario. *C0* is for simulations without a calmed region. In the scenario *C1* each spot is followed by a calmed region. The x -axis is scaled with $x_{\gamma=0.99}$.

5.7 Effect of calmed region

The calmed region behind a spot has received attention in recent years. It has been noticed that immediately behind a turbulent spot, the flow is highly stable and the probability of breakdown is negligible. Not much is understood yet about why the patch of turbulence is followed by an extra calm region. It has however been noticed that the velocity profile in this region is fuller (see e.g. van Hest *et al.*, 1994; Schulte & Hodson, 1998; Seifert & Hodson, 1999; Walker & Gostelow, 1990). Therefore instability and formation of turbulent spot is very unlikely in this region. Incidentally this is one of the justifications given in favour of the hypothesis of concentrated breakdown. Ramesh & Hodson (1999) proposed a new model for intermittency in flat plate boundary layers, where calming effect was modelled by a modified spot propagation parameter.

We have conducted simulations to account for the effect of the calmed region

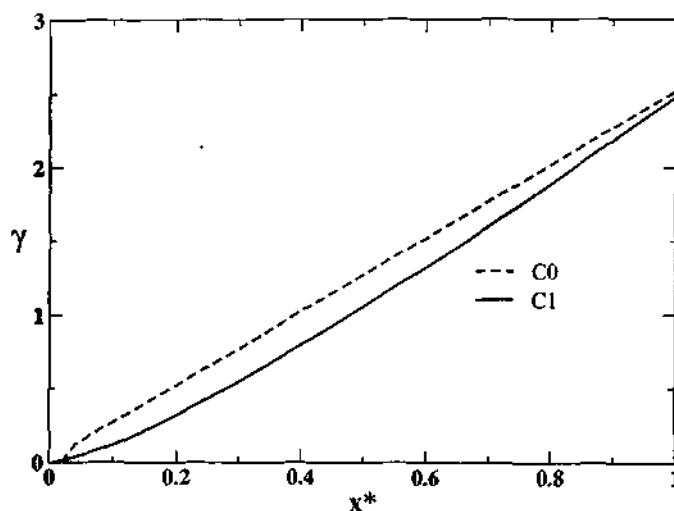


Figure 5.20: The intermittency parameter F for the results shown in figure 5.19.

trailing behind the spots. In the simulation the formation of spot is prevented from a prescribed region, upstream of the tail of a spot. The intermittency variation is given in the figure 5.19. The parameter F is plotted in figure 5.19 and the difference is quite visible. The burst rate in the boundary layer is given in figure 5.21. The peak of the burst rate is shifted marginally towards the downstream direction, making the distribution more symmetric. It is seen that the calming effect does not change the burst rate in a random breakdown.

5.8 Axisymmetric Boundary Layers

Transition to turbulence in boundary layers forming around axisymmetric bodies is poorly understood in spite of wide application in the motion of submarines, fishes etc. When the transverse curvature is significant, transition can proceed quite differently from a two-dimensional boundary layer (Govindarajan & Narasimha, 2000). When the typical patch of turbulence, consisting either of a single spot

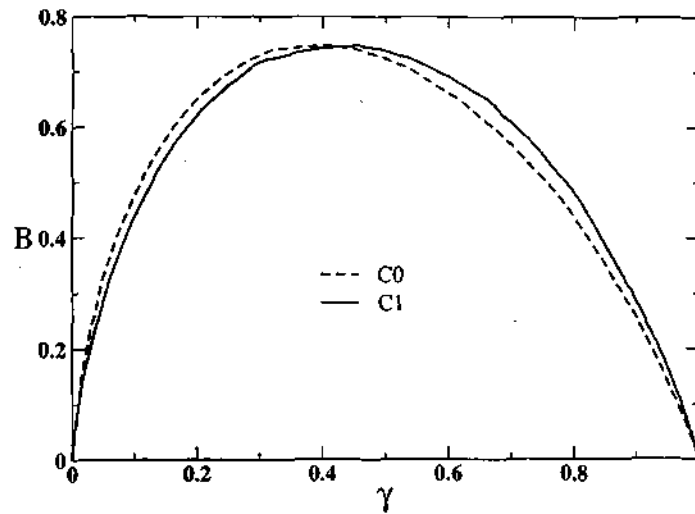


Figure 5.21: Burst rate plotted against intermittency. *C0* is without considering the effect of the calmed region. In the scenario *C1* each spot is followed by a calmed tail. The maxima are scaled arbitrarily.

or a group of spots which have merged laterally, attains a width of the order of the diameter of the cylinder, it wraps itself around the body. Downstream of the location of wrap, further lateral growth is not possible. The turbulent patch then resembles a sleeve (Narasimha, 1985; Rao, 1974) displaying only a one-dimensional growth in the streamwise direction.

We have carried out stochastic simulations of the birth, downstream propagation and growth of turbulent spots in the transition zone of an axisymmetric boundary layer. The downstream variation of the intermittency parameter F is shown in figure 5.22. The quantity c is the circumference of the body. In the initial region, transition proceeds exactly as it would in two-dimensional flow. This is because spots are too small to “see” the body. When spots wrap themselves around the cylinder, a qualitative change is observed, as is expected from the discussion above, and transition proceeds much more slowly after this. The burst rate B shown in figure 5.23 is another indication of the differences in the transition

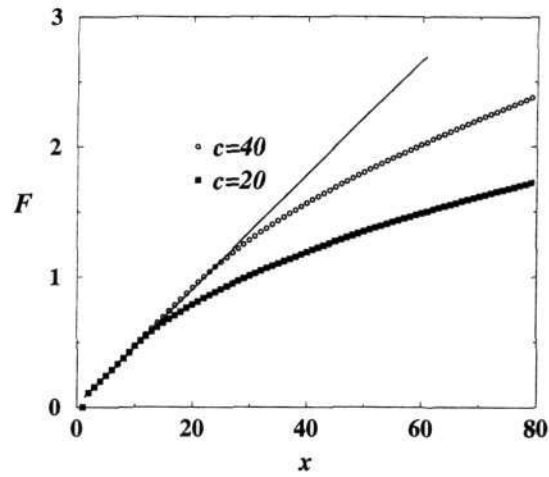


Figure 5.22: The intermittency factor F Vs. X , for different circumferences of the cylinder. The straight line is the result of two-dimensional simulations with the same spot birth rate.

process. Again there is a qualitative difference downstream of the “wrapping location”. Experiments on axisymmetric bodies are called for which can check these predictions.

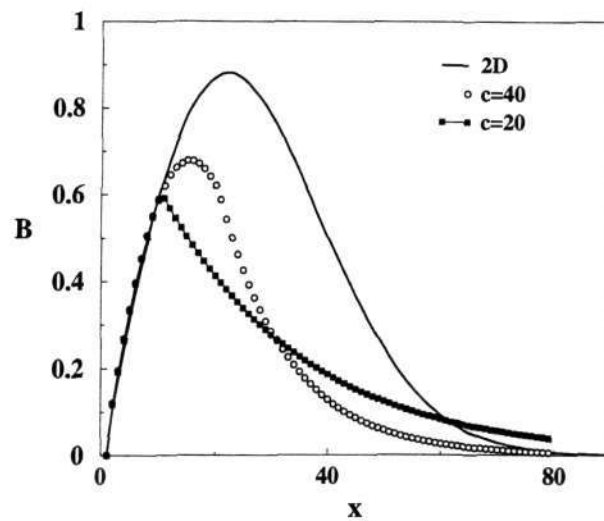


Figure 5.23: The burst rate in the transition zone of the boundary layer around a cylinder.

CHAPTER 6

CONCLUSIONS

6.1 Summary of Results

Instability and the process of transition in axisymmetric laminar boundary layers are found to be different from two-dimensional boundary layers, since transverse curvature has an effect on both. The main findings on instability are as follows. In an extension to Rayleigh's and Fjørtoft's theorem to axisymmetric boundary layers, the boundary layer past a cylinder is shown to be inviscidly stable. Above a certain level of curvature, the flow is linearly stable at all Reynolds numbers. Squire's theorem does not apply and the helical mode is unstable at the lowest Reynolds number.

At low curvatures, several nonaxisymmetric modes are simultaneously unstable, and the production layers of the disturbance kinetic energy have a significant overlap. Higher non-axisymmetric modes ($n \geq 2$) are linearly unstable only for a very small range of curvatures. The helical ($n = 1$) mode is unstable over a significant axial extent of the cylinder, but is never unstable for curvatures above 1. Curvature has an overall stabilising effect, both via the mean flow, as well as directly through the stability equations.

The secondary instability analysis of the flow containing linear modes of a certain amplitude is carried out. It is found that secondary modes are unstable at larger curvatures than linear modes. However there is again a maximum curvature,

where $\theta \approx 2r_0$, above which all disturbances decay. It is found that the most unstable secondary modes are always those whose azimuthal wavenumbers are related to that of the primary mode by $m_+ = 2n$ and $m_- = -n$. As in two-dimensional boundary layers the subharmonic (in terms of axial wavenumber) modes are least stable.

For the transition zone we have focussed mainly on two-dimensional boundary layers. This is because the connection between instability and the transition is not understood even for this case. Secondly experimental results are available only for this case. Stochastic simulations, inspired by a cellular-automaton approach, of turbulent spot generation and propagation in transitional boundary layers have been conducted, employing the hypothesis of concentrated breakdown and the observation that spot growth is self-similar.

The primary objective is to make a connection between secondary instability and the onset of transition. It is shown that experimental measurements of intermittency in high disturbance environments as well as in adverse pressure gradients are consistent with a primarily regular pattern in the birth of turbulent spots, rather than randomly distributed spot birth as hitherto assumed. The pattern is as dictated by the secondary instability. At zero pressure gradient, when the disturbance is low, the intermittency is consistent with random spot birth, reasons are discussed.

The simulations are used to validate the hypothesis of concentrated breakdown as well as to investigate the effect of the calmed region behind a turbulent spot. Further predictions are made which may be experimentally verified. Simulations on axisymmetric boundary layers show that the presence of curvature results in a longer transition zone. i.e. a slower attainment of fully turbulent flow. In conjunction with experimental measurements, the approach can serve as a useful

new tool to study transition zone behaviour.

6.2 Suggestions for future work

The balance of disturbance kinetic energy shows that the production layers of various linear modes overlap over a significant radial extent. This could imply that nonlinearities have a chance to grow much earlier in the transition process than in the case of two-dimensional boundary layers. An extension of the present study into the non-linear regime is required to tell whether nonlinear interactions among the above modes can lead to turbulence, and if so, whether the flow will relaminarise downstream due to the tendency for the boundary layer to remain stable at higher curvatures. At higher freestream disturbance environments, algebraic growth plays an important role in the transition to turbulence in two-dimensional boundary layers. It would be of interest to study the effect of curvature on transient growth and to see whether streaks play the same role here as in two-dimensional boundary layers.

The present results are limited to the flow past a cylinder, but the formulation derived here may be used to study arbitrary axisymmetric bodies. Non-parallel effects may be important in flows involving complex geometries. Understanding the receptivity of three-dimensional disturbances in curved flows is important.

Since the transition zone is not well-understood, there is a lot of scope for future work. Statistical measures such as intermittency, burst rates and persistence times of laminar flow are relatively straightforward to obtain experimentally. These can be used to infer the pattern of spot breakdown and to make connections with upstream processes as described in this thesis.

APPENDIX I

CHEBYSHEV SPECTRAL COLLOCATION METHOD

A.1 Chebyshev Expansions

Chebyshev polynomials can be defined in one of the following ways;

(1) Trigonometric Function

$$T_n(y) = \cos(ncos^{-1}y). \quad (I.1)$$

noindent (2) Rodrigues' Formula

$$T_n(y) = \frac{(-1)^n 2^n n!}{(2n)!} \sqrt{1-y^2} \frac{d^n}{dy^n} [(1-y^2)^{n-1/2}]. \quad (I.2)$$

(3) A Direct Formula

$$T_n(y) = \frac{1}{2} [(y + \sqrt{1-y^2})^n + (y - \sqrt{1-y^2})^n]. \quad (I.3)$$

(4) Solution of Sturm-Liouville

$$\frac{d}{dy} \left(\sqrt{1-y^2} \frac{d}{dy} T_n(y) \right) + \frac{n^2}{\sqrt{1-y^2}} T_n(y) = 0. \quad (I.4)$$

(5) Recurrence Relation

$$T_0(y) = 1, \quad T_1(y) = y, \quad T_{n+1}(y) = 2yT_n(y) - T_{n-1}(y). \quad (\text{I.5})$$

The Chebyshev polynomials satisfy the orthogonality condition

$$\int_{-1}^1 \frac{T_n(y)T_m(y)}{\sqrt{1-y^2}} dy = C_n \delta_{nm} \quad C_0 = \pi \quad C_n = \pi/2 \quad (n \neq 0) \quad (\text{I.6})$$

The variables can be expanded as

$$\phi(y) = \sum_{n=0}^N a_n T_n(y) \quad (\text{I.7})$$

The domain in between -1 and $+1$, y_i 's are called Gauss-Lobatto points given as,

$$y_i = \cos(i\pi/N). \quad (\text{I.8})$$

The computation domain should be transformed from physical to a Gauss-Labatto. Chebyshev spectral methods are dealt in the classic books (see Boyd, 2001; Canuto *et al.*, 1987; Gottlieb & Orszag, 1977; Peyret, 2002).

A.2 Differentiation in Chebyshev Plane

The derivative of $\phi(y)$ can be evaluated in two ways.

Method 1

Let $\phi_N^{(p)}(y_i)$ be the p^{th} derivative. Then

$$\phi_N^{(p)}(y_i) = \sum_{n=0}^N a_n T_n^{(p)}(y_i) \quad (\text{I.9})$$

The $T_n^{(p)}(y_i)$ can be evaluated from the recurrence formula I.5. There is another transformation associated with equation I.9. This method is not usually used for eigenvalue value problems. Equation I.9 can be transformed to as

$$\phi_N^{(p)}(y_i) = \sum_{n=0}^N b_n^{(p)} T_n(y_i) \quad (\text{I.10})$$

where $b_n^{(p)}$ are the coefficients of derivatives which can be transformed from Chebyshev coefficients. The first two derivative transformations are given below.

$$b_n^{(1)} = \frac{2}{c_n} \sum_{p=n+1}^N p a_p \quad \text{if } p+n \text{ odd} \quad (\text{I.11})$$

$$b_n^{(2)} = \frac{1}{c_n} \sum_{p=n+2}^N p(p^2 - n^2) a_p \quad \text{if } p+n \text{ even} \quad (\text{I.12})$$

where $\bar{c}_0 = \bar{c}_N = 2$, $\bar{c}_n = 1$ for $1 \leq j \leq N-1$.

Method 2

The dependent variable $\phi_N(y_i)$ can also be written as

$$\phi_N(y) = \sum_{j=0}^N h_j(y) \phi_N(y_j) \quad (\text{I.13})$$

where $h_j(y)$ is the polynomial of degree N defined as,

$$h_j(y) = \frac{(-1)^{j+1}(1-y^2)T_N'(y)}{\bar{c}_j N^2 (y-y_j)} \quad (\text{I.14})$$

Then the derivative can be written as

$$\phi_N^{(p)}(y_i) = \sum_{j=0}^N d_{i,j}^{(p)} \phi_N(y_j) \quad (\text{I.15})$$

where $d_{i,j}^{(p)} = h_j^{(p)}(y_i)$. The expression of coefficients for some $d_{i,j}^{(p)}$ are

$$d_{i,j}^{(1)} = \begin{cases} \frac{\bar{c}_i}{\bar{c}_j} \frac{(-1)^{i+j}}{(y_i - y_j)}, & 0 \leq i, j \leq N, \quad i \neq j \\ -\frac{y_i}{2(1-y_i^2)}, & 1 \leq i \leq N-1, \quad i = j \end{cases} \quad (\text{I.16})$$

$$d_{0,0}^{(1)} = -d_{N,N}^{(1)} = \frac{2N^2 + 1}{6} \quad (\text{I.17})$$

where $\bar{c}_0 = \bar{c}_N = 2$, $\bar{c}_j = 1$ for $1 \leq j \leq N-1$ and

$$d_{i,j}^{(2)} = \sum_{k=0}^N d_{i,k}^{(1)} d_{i,k}^{(1)}. \quad (\text{I.18})$$

So that in vector form, $\phi^{(p)} = D^{(p)}\phi$ where $D = d_{i,j}^{(1)}$, $i, j = 0, \dots, N$.

A.3 Chebyshev Discretisation of OS Equation

The Orr-Sommerfeld equation can be written as,

$$(U - \omega/\alpha)(v'' - \alpha^2 v) - U''v = \frac{1}{i\alpha R}(v^{iv} - 2\alpha^2 v'' + \alpha^4 v) \quad (\text{I.19})$$

For boundary layers $U(y)$ is the mean velocity non-dimensionalised by U_∞ , and the primes denote differentiation with respect to y . The boundary conditions are, $v = v' = 0$ at the wall, and $v, v' \rightarrow 0$ as $y \rightarrow \infty$. Equation I.19 can be discretised

as in the above two method.

Method 1

The derivative is given by equation I.9. Equation I.19 discretised as,

$$\begin{aligned}
& \left[U \sum_{n=0}^N a_n T_n^{(2)}(y) - (k^2 U - U'') \sum_{n=0}^N a_n T_n^{(0)}(y) \right] \\
& - \frac{1}{i\alpha_p Re} \left[\mu \sum_{n=0}^N a_n T_n^{(4)}(y) + 2\mu' \sum_{n=0}^N a_n T_n^{(3)}(y) + (\mu'' - 2k^2 \mu) \sum_{n=0}^N a_n T_n^{(2)}(y) \right. \\
& \left. - 2k^2 \mu' \sum_{n=0}^N a_n T_n^{(1)}(y) + (k^2 \mu'' + k^4 \mu) \sum_{n=0}^N a_n T_n^{(0)}(y) \right] \\
& = \left[\sum_{n=0}^N a_n T_n^{(2)}(y) - k^2 \sum_{n=0}^N a_n T_n^{(0)}(y) \right] c_p \tag{I.20}
\end{aligned}$$

where $k^2 = \alpha_p^2 + \beta_p^2$. The equation I.20 with boundary conditions will be an eigenvalue problem of the form $Aa = c_p Ba$.

Method 1

The derivative is given by equation I.15

$$\begin{aligned}
& \left[U D^2 \phi(y) - (k^2 U - U'') \phi(y) \right] \\
& - \frac{1}{i\alpha_p Re} \left[\mu D^4 \phi(y) + 2\mu' D^3 \phi(y) + (\mu'' - 2k^2 \mu) D^2 \phi(y) \right. \\
& \left. - 2k^2 \mu' D^1 \phi(y) + (k^2 \mu'' + k^4 \mu) \phi(y) \right] \\
& = \left[D^2 \phi(y) - k^2 \phi(y) \right] c_p \tag{I.21}
\end{aligned}$$

The equation I.20 with boundary conditions will be an eigenvalue problem of the form $A\phi = c_p B\phi$.

References

- ANDERSSON, P., BERGGREN, M. & HENNINGSON, D. S. 1999 Optimal disturbances and bypass transition in boundary layers. *Phys. Fluids* **11**, 134.
- ANDERSSON, P., BRANDT, L., BOTTARO, A. & HENNINGSON, D. S. 2001 On the breakdown of boundary layer streaks. *J. Fluid Mech.* **428**, 29–60.
- BARRY, M. D. J. & ROSS, M. A. S. 1970 The flat plate boundary layer Part 2. The effect of increasing thickness on stability. *J. Fluid Mech.* **43**, 813–818.
- BAYLY, B. J., ORSZAG, S. A. & HERBERT, T. 1988 Instability mechanisms in shear flow transition. *Annu. Rev. Fluid Mech.* **20**, 359–391.
- BECH, K. H., HENNINGSON, D. S. & HENKES, R. A. W. M. 1998 Linear and nonlinear development of localised disturbances in zero and adverse pressure gradient boundary layers. *Phys. of Fluids* **10** (6), 1405–1418.
- BERTOLOTTI, F. P., HERBERT, T. & SPALART, P. R. 1992 Linear and nonlinear stability of the Blasius boundary layer. *J. Fluid Mech.* **242**, 441–474.
- BOIKO, A. V. 2002 Receptivity of a flat plate boundary layer to freestream axial vortex. *Eur. J. Mech. B Fluids* **21**, 325.
- BOIKO, A. V. & CHUN, H. H. 2004 Development of low-frequency streaks in Blasius boundary layer. *Phys. Fluids* **16**, 3153–3160.
- BOIKO, A. V., WESTIN, K. J. A., KLINGMANN, B. G. B., KOZLOV, V. V. & ALFREDSON, P. H. 1994 Experiments in a boundary layer subjected to freestream turbulence, Part 2. The role of TS waves in the transition process. *J. Fluid Mech.* **281**, 219.
- BOYD, J. P. 2001 *Chebyshev and Fourier Spectral Methods*, 2nd edn. Dover Publishers.
- BRANDT, L., COSSU, C., CHOMAZ, J. M., HUERRE, P. & HENNINGSON, D. S. 2003 On the convectively unstable nature of optimal streaks in boundary layers. *J. Fluid Mech.* **485**, 221–242.

- BRANDT, L. & HENNINGSON, D. S. 2002 Transition of streamwise streaks in zero pressure gradient boundary layers. *J. Fluid Mech.* **472**, 229–261.
- CANUTO, C., HUSSAINI, M. Y., QUARTERONI, A. & ZANG, T. A. 1987 *Spectral Methods in Fluid Dynamics*, 1st edn. Springer-Verlag.
- CHANDRASEKHAR, S. 1961 *Hydrodynamics and hydromagnetic stability*. Oxford University Press, London.
- CORBET, P. & BOTTARO, A. 2000 Optimal perturbations for boundary layers subject to streamwise pressure gradient. *Phys. Fluids* **12**, 120–130.
- CORKE, T. C. & GRUBER, S. 1989 Resonant growth of three-dimensional modes in Falkner-Skan boundary layers with adverse pressure gradients. *J. Fluid Mech.* **320**, 211–233.
- CORKE, T. C. & MANGANO, R. A. 1989 Resonant growth of three dimensional modes in translational Blasius boundary layers. *J. Fluid Mech.* **209**, 93–150.
- CRAIK, A. D. D. 1971 Nonlinear resonant instability in boundary layers. *J. Fluid Mech.* **50**, 393.
- DAVEY, A. & DRAZIN, P. G. 1969 The stability of Poiseuille flow in a pipe. *J. Fluid Mech.* **36**, 209–218.
- DAVIES, S. J. & WHITE, C. M. 1928 An experimental study of the flow of water in pipes of rectangular section. *Proc. Roy. Soc* **119**, 92–107.
- DEY, J. & NARASIMHA, R. 1988 An integral method for the calculation of 2-d transition boundary layers. *Dept. Aerospace Engg., Indian Institute of Science, Rep. 88FM7*.
- DHAWAN, S. & NARASIMHA, R. 1958 Some properties of boundary layer flow during transition from laminar to turbulent motion. *J. Fluid Mech.* **3**, 418–437.
- DRAZIN, P. G. & REID, W. H. 1981 *Hydrodynamic Stability*. Cambridge University Press, London.
- DUCK, P. W. 1984 The effect of a surface discontinuity on an axisymmetric boundary layer. *Q. J. Mech. Appl. Maths* **37**, 57–74.
- DUCK, P. W. 1990 The inviscid axisymmetric stability of the supersonic flow along a circular cylinder. *J. Fluid Mech.* **214**, 611–637.
- DUCK, P. W. & HALL, P. 1989 On the interaction of Tollmein-Shlichting waves in axisymmetric supersonic flows. *Q. J. Mech. Appl. Maths* **42**, 191–201.

- ELLINGSEN, T. & PALM, E. 1975 Stability of linear flow. *Phys. Fluids* **18**, 487.
- EMMONS, H. 1951 The laminar-turbulent transition in a boundary layer - part 1. *J. Aero. Sci.* **18**, 490-498.
- FAISST, H. & ECKHARDT, B. 2003 Travelling waves in pipes. *Phys. Rev. Lett.* **91** (22), 224502.
- FASEL, H. & KONZELMANN, U. 1990 Non-parallel stability of flat-plate boundary layer using complete Navier-Stokes equations. *J. Fluid Mech.* **221**, 311-347.
- FJORTOFT, R. 1950 Application of integral theorems in deriving criteria of stability for laminar flow and for the baroclinic circular vortex. *Geofys. Pub. Oslo* **17** (6), 1-52.
- FRANSSON, J. H. M., BRANDT, L., TALAMELLI, A. & COSSU, C. 2004 Experimental and theoretical investigation of the nonmodal growth of steady streaks in a flat plate boundary layer. *Phys. Fluids* **16**, 3627-3638.
- GASTER, M. 1974 On the effects of boundary layer growth on flow stability. *J. Fluid Mech.* **66**, 465-480.
- GLAUERT, M. B. & LIGHTHILL, M. J. 1955 The axisymmetric boundary layer on a thin cylinder. *Proc. Roy. Soc. London Ser. A* **230**, 188-203.
- GÖRTLER, H. 1940 Über eine dreidimensionale instabilität laminarer grenzschichten an konkaven wänden. *Nachr. Ges. Wiss. Göttingen, N. F.* **2**, 1-26, Translated as 'On the three-dimensional instability of laminar boundary layers on concave walls', *Tech. memor. nat. Adv. Comm. Aero., Wash No.* 1375 (1954) pp. 116-118.
- GOSTELOW, J. P. & BLUNDEN, A. R. 1988 Investigations of boundary layer transition in adverse pressure gradient. *33rd ASME International Gas Turbine and Aeroengine Congress, Amsterdam (Netherlands)* .
- GOSTELOW, J. P., BLUNDEN, A. R. & WALKER, G. J. 1994 Effects of free-stream turbulence and adverse pressure gradients on boundary layer transition. *Trans. ASME J. Turbomachinery* **116**, 392-404.
- GOSTELOW, J. P., MELWANI, N. & WALKER, G. J. 1995 Effect of streamwise pressure gradient on turbulent spot development. *ASME paper 95-GT-303* .
- GOTTLIEB, D. & ORSZAG, S. A. 1977 *Numerical analysis of spectral methods: Theory and Applications*.. SIAM, Philadelphia.
- GOVINDARAJAN, R. & NARASIMHA, R. 2000 Transition delay by surface heating: a zonal analysis for axisymmetric bodies. *J. Fluid Mech.* **418**, 77-100.

- GREGORY, N. & WALKER, W. S. 1950 The effect on transition of isolated surface excrescences in the boundary layers. *A.R.C. Tech. Report. 2779* p. 436, published as Aeronaut. Res. Council R&M 2779 (1956) pp 1-10.
- HEISENBERG, W. 1924 Über stabilität und turbulenz von flüssigkeitsströmen. *Ann. Phys. Lpz.* **74** (4), 577-627., Translated as 'On stability and turbulence of fluid flows', *Tech. Memor. Nat. Adv. Comm. Aero. Wash.*, No. 1291 (1951).
- VON HELMHOLTZ, H. 1868 Über discontinuirliche flüssigkeitsbewegungen. *Monats. Königl. Preuss. Akad. Wiss. Berlin* **23**, 215-28, Translated to english by F. Guthrie as 'On discontinuous movements of fluids,' *Phil. Mag.*(4) **36**, 337-46 (1868).
- HERBERT, T. 1988 Secondary instability of boundary layers. *Annu. Rev. Fluid Mech.* **20**, 487-526.
- VAN HEST, B. F. A., PASSCHIER, D. M. & VAN INGEN, J. L. 1994 The development of turbulent spots in adverse pressure gradient boundary layers. *Proc. IUTAM Symp. on Laminar-Turbulent Transition , Sendai* .
- HOF, B., VAN DOORNE, C. W. H., WESTERWEEL, J., NIEUWSTADT, F. T. M., FAISST, H., ECKHARDT, B., WEDIN, H., KERSWELL, R. R. & WALLEFFE, F. 2004 Experimental observation of nonlinear traveling waves in turbulent pipe flow. *Science* **305**, 1594.
- HOGBERG, M. & HENNINGSON, D. 1998 Secondary instability of cross-flow vortices in Falkner-Skan-Cooke boundary layers. *J. Fluid Mech.* **368**, 339-357.
- HUERRE, P. & ROSSI, M. 1998 Hydrodynamic instabilities in openflows. In *Hydrodynamics and nonlinear instabilities* (ed. C. Godreche & P. Manneville), pp. 81-288. Cambridge University Press, Cambridge.
- HUNT, J. C. R., DURBIN, P. A., KEVLAHAN, K. R. & FERNANDO, H. J. S. 1996 Non-local effects of shear in turbulent flows. In *Presented at the Sixth European Turbulence Conference*. Lausanne, Switzerland.
- VAN INGEN, J. L. 1956 A suggested semi-empirical method for the calculation of boundary layer transition region. *Tech. Rep. VTH-74*. Dept. of Aeronautical Engg., Univ. of Delft.
- JACOBS, R. G. & DURBIN, P. A. 1998 Shear sheltering and the continuous spectrum of the orr-sommerfeld. *Phys. Fluids* **10** (8), 2006.
- JOHNSON, M. W. & FASIHFAR, A. 1994 Properties of turbulent bursts in transition boundary layers. *Int. J. of Heat and Fluid Flow* **15** (4), 283-290.

- KACHANOV, YU, S. & LEVCHENKO, V. Y. 1984 The resonant interaction of disturbances at laminar-turbulent transition in a boundary layer. *J. Fluid Mech.* **138**, 209–247.
- KACHANOV, Y. S. 1994 Physical mechanisms of laminar-boundary layer transition. *Annu. Rev. Fluid Mech.* **26**, 411–482.
- KACHANOV, Y. S., KOZLOV, V. & LEVCHENKO, V. Y. 1977 Nonlinear development of a wave in a boundary layer. *Izv. Akad. Nauk SSSR, Mekh. Zhidk. Gaza* **3**, 49–53, in Russian. Transl. *Fluid Dyn.* 1978, 12:383:90.
- KAO, T. W. & PARK, C. 1970 Experimental investigations of the stability of channel flows. part 1. flow of a single liquid in a rectangular channel. *J. Fluid Mech.* **43**, 145.
- KATZ, Y., SEIFERT, A. & WYGNANSKI, I. 1990 On the evolution of turbulent spots in a laminar boundary layer with a favorable pressure gradient. *J. Fluid Mech.* **221**, 1–22.
- KELVIN, L. 1871 Hydrokinetic solutions and observations. *Phil. Mag.* **42** (4), 362–77. Also *mathematical and physical papers*(1910) vol. IV, pp69-85.
- KLEBANOFF, P. S., TIDSTORM, K. D. & SARGENT, L. M. 1962 The three-dimensional nature of boundary layer instability. *J. Fluid. Mech.* **12**, 1–34.
- KLINGMANN, B. G. B., BOIKO, A. V., WESTIN, K. J. A., KOZLOV, V. V. & ALFREDSSON, P. H. 1993 Experiments on the stability of Tollmien-Schlichting waves. *Euro. J. Mech. B, Fluids* **12**, 493–514.
- KOCH, W., BERTOLOTTI, F. P., STOLTE, A. & HEIN, S. 2000 Nonlinear equilibrium solutions in a three-dimensional boundary layer and their secondary instability. *J. Fluid Mech.* **406**, 131–174.
- LANDAHL, M. T. 1975 Wave breakdown and turbulence. *SIAM J. Appl. Math.* **28**, 735–756.
- LANDAHL, M. T. 1980 A note on algebraic instability of inviscid parallel shear flows. *J. Fluid Mech.* **98**, 243–251.
- LAUCHLE, G. & GURNEY, G. 1984 Laminar boundary layer transition on a heated underwater body. *J. Fluid Mech.* **144**, 79–101.
- LESSEN, M., SADLER, S. G. & LIU, T. Y. 1968 Stability of pipe Poiseuille flow. *Phys. Fluids* **11**, 1404–1409.
- LIN, C. C. 1955 *The theory of hydrodynamic stability*. Cambridge University Press.

- LING, C. H. & REYNOLDS, W. C. 1973 Non parallel flow corrections for the stability of shear flows. *J. Fluid Mech.* **59**, 57–591.
- LIU, C. & MASLOWE, S. A. 1999 A numerical investigation of resonant interactions in adverse-pressure-gradient boundary layers. *J. Fluid Mech.* **378**, 269–289.
- LUCHINI, P. 2000 Reynolds-number-independent instability of the boundary layer over a flat surface: optimal perturbations. *J. Fluid Mech.* **404**, 289–309.
- MACK 1987 Stability of axisymmetric boundary layers on sharp cones at hypersonic Mach numbers. *AIAA paper 87-1413* .
- MACK, L. M. 1976 A numerical study of temporal eigenvalue spectrum of the Blasius boundary layer. *J. Fluid Mech.* **73**, 497–520.
- MALIK, M. R. 1987 Stability of axisymmetric boundary layers on sharp cones at hypersonic Mach numbers. *AIAA Paper 87-4113* .
- MALIK, M. R., LI, F. & CHANG, C. L. 1994 Crossflow disturbances in three-dimensional boundary layers: nonlinear development, wave interaction and secondary instability. *J. Fluid Mech.* **268**, 1–36.
- MALIK, M. R. & POLL, D. I. A. 1985 Effect of curvature on three-dimensional boundary layer stability. *AIAA J.* **23** (9), 1362.
- MALIK, M. R. & SPALL, R. E. 1991 On the stability of compressible flow past axisymmetric bodies. *J. Fluid. Mech.* **228**, 443–463.
- MANGLER, W. 1945 Boundary layers on bodies of revolution in symmetrical. *Ber. Aerodyn. Versuchsanst. Goett, Report 45/A/17* .
- MASLOWE, S. A. 1974 Instability of rigidly rotating flows to non-axisymmetric disturbances. *J. Fluid. Mech.* **64**, 307–317.
- MATSUBARA, M. & ALFREDSSON, P. H. 2001 Disturbance growth in boundary layers subjected to free-stream turbulence. *J. Fluid. Mech* **430**, 149–168.
- MICHEL, R. 1952 Etude de la transition sur les profils d'aile; établissement d'un critère de détermination de point de transition et calcul de la traînée de profil incompressible. *ONERA Tech. Rep. 1/1578/A* .
- MORKOVIN, M. V. & RESHOTKO, K. 1989 Dialogue on progress and issues in stability and transition research. *IUTAM symposium on Laminar-Turbulent transition* pp. 3–29.
- NARASIMHA, R. 1957 On the distribution of intermittency in the transition region of a boundary layer. *J. Aero. Sci.* **24**, 711–712.

- NARASIMHA, R. 1984 Subtransitions in the transition zone. *Proc. IUTAM Symp. on Laminar-Turbulent Transition*, Novosibirsk .
- NARASIMHA, R. 1985 The laminar-turbulent transition zone in the boundary layer. *Prog. Aero. Sci.* **22**, 29–80.
- NARAYANAN, M. A. B. & NARAYANAN, T. 1967 Some studies on transition from laminar to turbulent flow in a two-dimensional channel. *Z. Angew. Math. Phys.* **18**, 642, in English *J. App. Math. and Phys.*
- NISHIOKA, M., IIDA, S. & ICHIKAWA, Y. 1975 An experimental investigation of the stability of plane Poiseuille flow. *J. Fluid Mech.* **72**, 731–751.
- ORR, W. M. F. 1907 The stability or instability of the steady motions of a perfect liquid and of a viscous liquid. Part I: A perfect liquid, Part II: A viscous liquid. *Proc. Roy. Irish Acad.* **27** (3), 69–138.
- PATEL, V. C. & HEAD, M. R. 1969 Some observations on skin friction and velocity profiles in fully developed pipe and channel flows. *J. Fluid Mech.* **38**, 181.
- PEYRET, R. 2002 *Spectral Methods for Incompressible Viscous Flow*. Springer.
- PRIGENT, A., GRÉGOIRE, G., CHATÉ, H., DAUCHOT, O. & VAN SAARLOOS, W. 2002 large scale finite wavelength modulation within transition shear flows. *Phys. Rev. Lett.* **89** (1), 014501.
- RAMESH, O. N. & HODSON, H. P. 1999 A new intermittency model incorporating the calming effect. *Proceedings of 3rd European Conf on Turbomachinery Fluid Dynamics and Thermodynamics, IMechE, London* pp. 243–258.
- RAO, G. N. V. 1967 Effects of convex transverse surface curvature on transition and other properties of the incompressible boundary layer. PhD thesis, Dept. of Aerospace Engg., Indian Institute of Science.
- RAO, G. N. V. 1974 Mechanics of transition in an axisymmetric boundary layer on a circular cylinder. *Z. Angew. Math. Phys.* **25**, 63–75.
- RAYLEIGH 1880 On the stability of certain fluid motions. *Proc. Math. Soc. Lond.* **11**, 57–70.
- REED, H. L. & SARIC, W. S. 1996 Linear stability theory applied to boundary layers. *Ann. Rev. Fluid Mech.* **28**, 389–428.
- RESHOTKO, E. 2001 Transient growth: A factor in bypass transition. *Phys. Fluids*. **13**(5), 1067–1075.

- REYNOLDS, O. 1883 An experimental investigation of the circumstances which determine whether the motion of water shall be direct or sinuous and of the law of resistance in parallel channels. *Phil. Trans. Roy. Soc.* **174**, 935–982.
- ROSS, J. A., BARNES, F. H., BURNS, J. G. & ROSS, M. A. S. 1970 The flat plate boundary layer Part 3. Comparison of theory with experiment. *J. Fluid Mech.* **43**, 819–832.
- SARIC, W. S., KOZLOV, V. V. & LEVCHENKO, V. Y. 1984 Forced and unforced subharmonic resonance in boundary layer transition. *AIAA paper 84-0007*.
- SARIC, W. S. & NAYFEH, A. H. 1975 Nonparallel stability of boundary layer flows. *Phys. of Fluids* **18**, 945–950.
- SARIC, W. S., REED, H. L. & WHITE, E. B. 2003 Stability and transition of three-dimensional boundary layers. *Ann. Rev. Fluid Mech.* **35**, 413–440.
- SARIC, W. S. & THOMAS, A. S. W. 1984 Experiments on the subharmonic route to turbulence in boundary layers. *In Proc. IUTAM Symp. on Turbulence and Chaotic Phenomenon in Fluids* pp. 117–122.
- SCHLICHTING, H. 1933 Zur entstehung der turbulenz bei der plattenstromung. *Nachr. Ges. Wiss. Gottingen, Math-phys., Kl.* pp. 181–208.
- SCHMID, P. J. & HENNINGSON, D. S. 1994 Optimal energy density growth in Hagen-Poiseuille flow. *J. Fluid Mech.* **277**, 197–225.
- SCHMID, P. J. & HENNINGSON, D. S. 2001 *Stability and transition in shear flows*. Springer-Verlag, New York.
- SCHUBAUER, G. B. & SKRAMSTAD, H. 1947 Laminar boundary layer oscillations and transition on a flat plate. *J. Res. Nat. Bur. Standards* **38**, 251–292.
- SCHULTE, V. & HODSON, H. P. 1998 Prediction of the becalmed region for lp turbine profile design. *ASME J. of Turbomachinery* **20** (4), 839–845.
- SEIFERT, A. & HODSON, H. 1999 Periodic turbulent strips and calmed regions in a transitional boundary layer. *AIAA J.* **37** (9), 127–1129.
- SEIFERT, A. & WYGNANSKI, I. J. 1995 On turbulent spots in a laminar boundary layer subjected to a self similar adverse pressure gradient. *J. Fluid Mech.* **296**, 185–209.
- SHANKAR, V. & KUMURAN, V. 2000 Stability of fluid flow in a flexible tube to non-axisymmetric disturbances. *J. Fluid. Mech.* **407**, 291–314.

- SMITH, A. M. O. & GAMBERONI, N. 1956 Transition, pressure gradient and stability theory. *Tech. Rep. ES 26388, Douglas Aircraft Co.* .
- SOMMERFELD, A. 1906 Ein beitrage zur hydrodynamischen erklaerung der turbulenten fluessigkeitsbewegungen. *Proc. Fourth Internat. Cong. Math., Rome III*, 116–124.
- SPALL, R. E. & MALIK, M. R. 1991 Effect of transverse curvature on the stability of compressible boundary layers. *AIAA J.* **29**, 1596–1602.
- SQUIRE, H. 1933 On the stability of three dimensional disturbances of viscous fluid between parallel walls. *Proc. Roy. Soc. London Ser. A.* **142**, 621–628.
- SREENIVASAN, S., KLIKA, S., LUDWIG, M. H. & RAM, V. V. 1994 A beginner's guide to the use of the spectral collocation method for solving some eigenvalue problems in fluid dynamics. *NAL Report PD EA 9408* .
- STETSON, K. F., THOMPSON, E. R., DONALDSON, J. C. & SILER, L. G. 1983 Laminar boundary layer stability experiments on a cone at mach 8. part i: Sharp cone. *AIAA paper 83-1761*.
- TANI, I. 1969 Boundary layer transition. *Ann. Rev. Fluid Mech.* **1**, 169.
- TOLLMIEIN, W. 1929 Uber die entstehung der turbulenz. *Nacher. ges. Wiss. Göttingen, Math-phys., Kl.* pp. 21–24.
- TOLLMIEIN, W. 1935 Ein allgemeines Kriterium der instabilitat laminarer Geschwindigkeitsverteilungen. *Nachr Ges. Wiss. Göttingen, Math. Phys. Kalsse Fachgruppe I* **1** (5), 79–114, English translation "General instability criterion of laminar velocity distributions", NACA-TM-792 (1936).
- TREFETHEN, L. N., TREFETHEN, A. E., REDDY, S. C. & DRISCOLL, T. A. 1993 Hydrodynamic stability without eigenvalues. *Science* **261**, 578–584.
- TUTTY, O. R., PRICE, W. G. & PARSONS, A. T. 2002 Boundary layer flow on a long thin cylinder. *Physics of Fluids* **14** (2), 628–637.
- WALEFFE, F. 2001 Exact coherent structures in channel flow. *J. Fluid Mech.* pp. 93–102.
- WALKER, G. J. & GOSTELOW, J. P. 1990 Effect of adverse pressure gradients on the nature and length of the boundary layer. *Trans. of ASME* **112**, 196–205.
- WAZZAN, A. R. 1975 Spatial stability of Tollmien- Schlichting waves. *Prog. Aerosp. Sci.* **16** (2), 99–127.

WHITE, E. B. 2002 Transient growth of stationary disturbances in a flat plate boundary layer. *Phys. Fluids* **14**, 4429.

WHITE, F. M. 1991 *Viscous Fluid Flow*, 2nd edn. McGraw-Hill.

ZELMAN, M. B. & MASLENNIKOVA, I. I. 1993 Tollmien-schlichting-wave resonant mechanism of subharmonic-type transition. *J. Fluid. Mech.* **252**, 449–478.

